

Homogeneous analysis of 239 Magellanic star clusters with AStECA

G.I. Perren^{1,3*}, A.E. Piatti^{2,3}, and R.A. Vázquez^{1,3}

¹ Facultad de Ciencias Astronómicas y Geofísicas (UNLP), IALP-CONICET, La Plata, Argentina

² Observatorio Astronómico, Universidad Nacional de Córdoba, Córdoba, Argentina

³ Consejo Nacional de Investigaciones Científicas y Técnicas (CONICET), Buenos Aires, Argentina

Received September 15, 1996; accepted March 16, 1997

ABSTRACT

Aims. To present a catalog of 239 resolved star clusters located in the Small and Large Magellanic Clouds, with their fundamental parameters fully estimated. All the clusters were observed in the Washington photometric system.

Methods. Our entire cluster sample was processed with the recently introduced Automated Stellar Cluster Analysis (AStECA) package, which ensures both an automatized and fully reproducible treatment, together with a statistically based obtention of their fundamental parameters and associated uncertainties. The main parameters determined with this tool for each cluster, via a color-magnitude diagram (CMD) analysis, are: metallicity, age, extinction, true distance modulus, and total mass.

Results. We generate a truly objective and homogeneous catalog composed of structural properties for each cluster, along with a complete determination of their fundamental parameters. A detailed internal error analysis and a thorough comparison with values taken from twenty-six published articles is also performed. We present a study of the distribution of all fundamental parameters in both Clouds, along with the obtention of a new age-metallicity relation derived from our homogeneous set of star cluster's ages and metallicities.

Conclusions. The AStECA package is shown to be capable of being applied to the unsupervised determination of fundamental cluster parameters; a task of increasing importance as more data becomes available through upcoming surveys.

Key words. catalogs – galaxies: fundamental parameters – galaxies: star clusters: general – Magellanic Clouds – methods: statistical – techniques: photometric

1. Introduction

The study of a galaxy's structure, dynamics, star formation history, chemical enrichment history, etc., depends heavily on the analysis of its star clusters. These galactic building blocks are made up of a varying number of coeval stars which share a chemical composition, are located at the same distance, and affected by roughly the same amount of reddening. All these factors greatly facilitate the obtention of their fundamental parameters, and thus the properties of the host galaxy. New developments in astrophysical software allow the homogeneous processing of different types of star clusters' databases. The article series by Kharchenko et al. (see Kharchenko et al. 2005; Schmeja et al. 2014, and references therein) and the integrated photometry based derivation of age and mass for 920 clusters presented in Popescu et al. (2012)¹, are examples of semi-automated and automated packages applied on a large number of clusters.

Such tools notwithstanding, there is no guarantee that employing a homogeneous method will result in similar – much less unique – parameter values across different studies. This is particularly true when the methods require user intervention, which inevitably makes the results subjective to some degree. In Netopil et al. (2015) the parameters age, extinction, and distance are contrasted throughout seven published databases, for open clusters matched across them (metallicity is not inspected as this quantity is usually assumed rather than adjusted). The authors find

that all articles show non-negligible offsets among each other, in the reported parameter values for the studied star clusters. This result underscores an important issue. Most of the times CMD isochrone fits are done by-eye, adjusting correlated parameters independently, and often omitting any kind of proper error treatment (see von Hippel et al. 2014, for a more detailed description of this problem). When statistical methods are employed, the used code is seldom publicly shared to allow scrutiny by the community. There is then no objective way to asses the underlying reliability of each set of results. Lacking this basic audit, the decision of which database values to use becomes a matter of preference.

As demonstrated by Hills et al. (2015), assigning precise fundamental parameters for an observed cluster (OC) is not a straightforward task. Using multiple combinations of up to eight filters ($UBVRIJHK_s$) and three stellar evolution models, they process an open cluster with their Bayesian isochrone fitting technique², and arrive at statistically different results for its final parameter values. The above study was performed on NGC188, a ~4 Gyr Milky Way OC with a well defined sequence that is rather unaffected by field star contamination, and with proper motions and radial velocities data available. One can therefore expect that analyzing clusters with a complex or non-standard morphology, affected by a significant amount of field star contamination, observed with fewer filters, and without information about its dynamics (i.e.: a rather standard situation), will be significantly more complicated. A mismatch between several theo-

* e-mail: gabrielperren@gmail.com

¹ Based on their MASSive CLuster Evolution and ANalysis (MASSCLEAN) package: <http://www.massclean.org/>

² BASE-9: <http://webfac.db.erau.edu/~vonhippt/base9/>

53 retical evolutionary models among themselves, along with an in-
 54 ability to reproduce OCs in the unevolved main sequence range,
 55 had already been reported in Grocholski & Sarajedini (2003).

56 The aforementioned difficulties in the analysis of an OC will
 57 only increase if the study is done by-eye, since: a) the number of
 58 possible solutions manually fitted is several orders of magnitude
 59 smaller than what a code can handle, b) correlations between
 60 parameters are almost entirely disregarded, c) uncertainties can
 61 not be assigned through valid mathematical means – and are
 62 often not assigned at all –, and d) the final values are necessarily
 63 highly subjective. The need is clear for an automated general
 64 method with a fully open and extensible code base, that takes
 65 as much information into account as possible, and is capable of
 66 generating reproducible results.

67
 68 In Perren et al. (2015) (hereafter Paper I) we presented the
 69 Automated STELLAR Cluster Analysis (AStECA³) package, aimed
 70 towards allowing a more accurate and comprehensive study of
 71 star clusters. Through an unassisted process the code analyses an
 72 OC's positional and photometric data to derive its fundamental
 73 parameters, along with their uncertainties. AStECA was applied
 74 on a group of 20 observed Milky Way open clusters in Paper I.
 75 As shown in that article, the code is able to assign precise param-
 76 eter values for OCs with low to medium field star contamination,
 77 and gives reasonable estimations for heavily contaminated OCs.
 78 Every part of this astrophysical package is open and publicly
 79 available, and its development is ongoing.

80 In the present work we apply AStECA on 239 OCs from the
 81 Small and Large Magellanic Clouds (S/LMC), distributed up
 82 to $\sim 5^\circ$ and $\sim 8^\circ$ in angular distance from their centers, respec-
 83 tively. The Magellanic Clouds (MCs) are located close enough
 84 to us to allow the study of their resolved star clusters. The large
 85 number of catalogued OCs – ~ 4000 are listed in the Bica et al.
 86 (2008) catalog – makes them an invaluable resource for investi-
 87 gating the properties of the two most massive galaxies that orbit
 88 the Milky Way. The reddening that affects the MCs is relatively
 89 small, except for a few regions like 30 Doradus in the LMC,
 90 where E_{B-V} extinction can reach values above 0.4 mag (Piatti
 91 et al. 2015a). The overall low levels of extinction further simpli-
 92 fies the research of these two galaxies, through the obtention of
 93 their clusters' parameters. We make use of the CT_1 filters of the
 94 Washington photometric system (Canterna 1976; Geisler 1996),
 95 which are known to produce a color that is highly sensitive to
 96 metal abundance (Geisler & Sarajedini 1999). The results ob-
 97 tained here regarding the metal content of the clusters in our
 98 sample, are thus of clear relevance for the analysis of the MCs
 99 chemical enrichment history.

100 This is the first study where such a large sample of resolved
 101 star clusters is homogeneously analyzed in an automatic way,
 102 with all of their fundamental parameters statistically estimated
 103 rather than fitted by eye or fixed a priori. Having metal content
 104 assigned for 100% of our sample is particularly important, espe-
 105 cially considering the state of other catalogs. The latest version
 106 of the well known DAML02 database⁴ (Dias et al. 2002) for ex-
 107 ample, reports abundances for only 13% out of the 2167 clus-
 108 ters it contains. Estimations for the total cluster mass are almost
 109 never given, except for a few works were integrated photometry
 110 is employed.

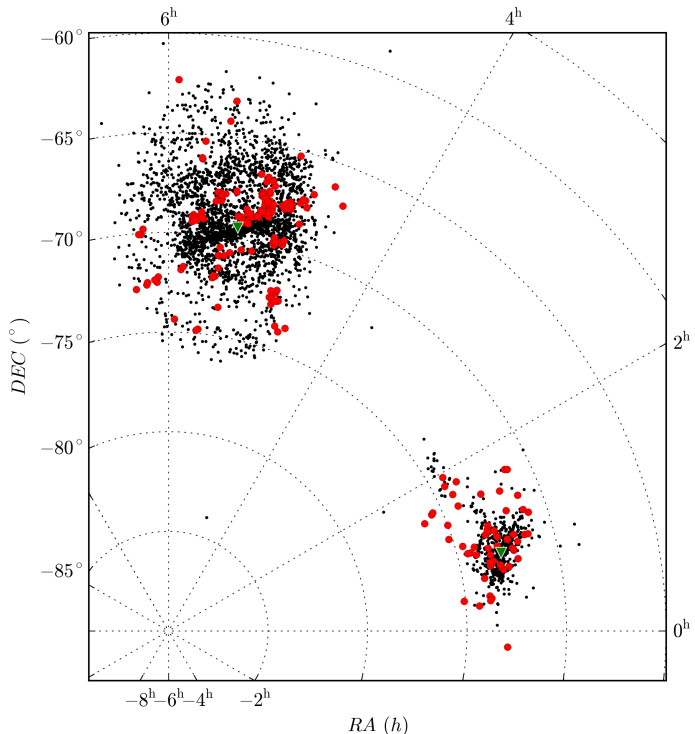


Fig. 1. Distribution of our set of analyzed OCs, shown in red, over the Bica et al. (2008) database of 3740 star clusters (black dots), for both MCs. The assumed centers for the Clouds are marked with a green triangle.

This article is structured as follows. In Sect. 2 we present the
 111 OC sample used in this work along with the twenty-six studies
 112 used to compare and validate our results. Sections 3 and 4 de-
 113 scribe the obtention of the fundamental parameters found with
 114 AStECA, and analyze their uncertainties respectively. In Sect. 5
 115 a detailed comparison of our results with published values from
 116 the aforementioned articles is performed. Sect. 6 shows how the
 117 fundamental parameters obtained with AStECA for both Clouds
 118 are distributed, along with the galaxies' age-metallicity relations.
 119 We give in Sect. 7 a summary of our results and concluding re-
 120 marks.

2. Observed clusters sample

The data used in this work consists of CT_1 Washington pho-
 123 tomographic system magnitudes and their errors, for the 239 OCs
 124 that comprise our sample. The majority of the OCs, 150 out of
 125 the 239, belong to the LMC while the remaining 89 belong to
 126 the SMC. In Fig. 1 we show the distribution of all OCs in both
 127 MCs, along with the entire set of star clusters from the Bica et al.
 128 (2008) database for reference.

All OCs in our sample have been previously analyzed and
 130 the results published in the articles shown in Table 1. These
 131 nineteen articles can be merged into a single group, whose re-
 132 sults arise from the analysis of the same CT_1 photometry used
 133 by AStECA in the current study. From here on we will refer to
 134 this group as the “literature”, and the values presented in each of
 135 the articles in Table 1 as “literature values”. Details on the data
 136 handling and reduction process can be found in the literature,
 137 and will not be repeated here. Metallicity, age, reddening, and
 138 true distance modulus (μ_0) values are assigned for all OCs by
 139 the literature articles, except for the 36 clusters presented in Pi-
 140 atti (2011b) which had only their ages estimated via the δT_1 in-

³ AStECA is released under a general public license (GPL v3; <https://www.gnu.org/copyleft/gpl.html>) and can be downloaded from its official site: <http://asteca.github.io>

⁴ Latest version: v3.5, 2016 Jan 28; <http://www.wilton.unifei.edu.br/ocdb/>

Table 1. Set of articles where the same CT_1 Washington photometric data was used, as that employed by AStECA in this work. N is the number of clusters present in this “literature” database, which are also present in our sample. The CTIO 0.9m, 1.5m, and Blanco 4m telescopes are located at Cerro Tololo (Chile); the Danish 1.54m telescope is located at La Silla Observatory (Chile).

Article	N	Galaxy	Telescope
Geisler et al. (2003)	8	LMC	CTIO 0.9m
Piatti et al. (2003b)	5	LMC	CTIO 0.9m
Piatti et al. (2003a)	6	LMC	CTIO 0.9m
Piatti et al. (2005)	8	SMC	CTIO 0.9m
Piatti et al. (2007a)	4	SMC	CTIO 0.9m
Piatti et al. (2007c)	2	SMC	Danish 1.54m
Piatti et al. (2007b)	2	SMC	Danish 1.54m
Piatti et al. (2008)	6	SMC	Danish 1.54m
Piatti et al. (2009)	5	LMC	CTIO 0.9m / Danish 1.54m
Piatti et al. (2011b)	3	LMC	CTIO 0.9m
Piatti et al. (2011a)	14	SMC	CTIO 1.5m
Piatti (2011a)	9	SMC	Blanco 4m
Piatti (2011b)	36	LMC	Blanco 4m
Piatti (2011c)	11	SMC	Blanco 4m
Piatti (2012)	26	LMC	Blanco 4m
Piatti & Bica (2012)	4	SMC	Blanco 4m
Palma et al. (2013)	23	LMC	Blanco 4m
Maia et al. (2013)	29	SMC	Blanco 4m
Choudhury et al. (2015)	38	LMC	Blanco 4m

Table 2. Set of articles where different photometric data was used to analyze the OCs sample. N is the number of clusters in each database that could be cross-matched with our set of 239 clusters. The photometry used in each article is shown in the “Phot” column.

Article	N	Galaxy	Phot
Pietrzynski & Udalski (1999), P99	7	SMC	BVI
Pietrzynski & Udalski (2000), P00	25	LMC	BVI
Hunter et al. (2003), H03	62	S/LMC	UBVR
Rafelski & Zaritsky (2005), R05	24	SMC	UBVI
Chiosi et al. (2006), C06	16	SMC	VI
Glatt et al. (2010), G10	61	S/LMC	UBVI
Popescu et al. (2012), P12	48	LMC	UBVR

142 dex (Phelps et al. 1994; Geisler et al. 1997). In most works the
143 metallicity is fixed to $z=0.004$ and $z=0.008$ ($[Fe/H]=-0.7$ dex,
144 $[Fe/H]=-0.4$ dex), while the distance modulus values are al-
145 ways fixed to $\mu_o=18.5$ mag and $\mu_o=18.9$ mag, for the S/LMC re-
146 spectively. Ages and extinctions reported in the literature were in
147 all cases obtained by eye, either through the standard isochrone
148 technique or applying the δT_1 index method (for the age parame-
149 ter). Maia et al. (2013) is the only article that presents total mass
150 estimations for their 29 OCs sample.

151 Our sample of 239 OCs was also cross-matched with a large
152 set of clusters taken from seven published articles, shown in Ta-
153 ble 2. These seven databases can be combined into a single group
154 of works, where different photometry was used to obtain the
155 fundamental parameter values for each OC. This group will be re-
156 ferred from here on as the “databases” (DBs), as a way to dis-
157 tinguish them from the “literature” articles mentioned above. In
158 Sect. 5 we show how the parameter values obtained by AStECA
159 for our sample of OCs, compares to those given in both the liter-
160 ature and the databases.

3. Obtention of observed clusters parameters

161

All the fundamental – metallicity, age, true distance modulus, ex-
162 tinction, mass – and structural parameters – center coordinates,
163 radius, contamination index, approximate number of members,
164 membership probabilities, true cluster probability – associated
165 with the OCs in our database, were obtained either automati-
166 cally or semi-automatically by the AStECA package. A detailed
167 description of the functions built within this tool can be found in
168 Paper I, and in the code’s online documentation⁵.

The final catalog, composed of the fundamental and struc-
170 tural parameters for the 239 resolved Magellanic star clusters
171 in our sample, can be accessed via VizieR⁶. We’ve made avail-
172 able online the entire Python codebase developed to analyze the
173 data obtained with AStECA and generate the figures in this arti-
174 cle.⁷ In addition, the full output image generated by AStECA for
175 each processed cluster together with its corresponding mem-
176 bership probability file, can be accessed separately through a public
177 code repository.⁸

3.1. Ranges for fitted fundamental parameters

179

Before AStECA is able to process an OC, the user is required
180 to provide a suitable range for each free (fitted) fundamental
181 parameter. This is accomplished by setting a minimum, a
182 maximum, and a step value in the appropriate input data file. As
183 explained in Sect. 3.4, each single value combination for each
184 of the five fundamental parameters fitted represents a unique
185 synthetic cluster, or model. Hence an interval too broad between
186 the minimum and maximum values for a given parameter, or a
187 very small step – or a combination of both – will result in a large
188 number of possible values. The larger the number of values a
189 parameter can access, the larger the number of models the code
190 will have to process to find the one with the best match to the
191 OC. For this reason, the allowed ranges and steps were selected
192 to provide a balance between a reasonably large interval, and a
193 computationally manageable number of total models. Especial
194 care must be taken, to avoid defining a range that could bias the
195 results towards a particular region of any fitted parameter. All
196 ranges can be seen in Table 3, with the rationale behind each
197 one explained below.

Unlike most previous works where the metallicity is a pre-
200 defined fixed value (usually $z = 0.008$ for the LMC and $z=0.004$
201 for the SMC), we do not make any assumptions on the clus-
202 ter’s metal content. The minimum and maximum $[Fe/H]$ values
203 selected are $[-2.2, 0]$ dex; with a step of ~ 0.1 dex. This inter-
204 val covers completely the usual metallicities reported for OCs in
205 the MCs. The age range is set to 1 Myr–12.6 Gyr with a step of
206 $\log(\text{age}/\text{yr}) = 0.05$ dex, encompassing almost the entire allowed
207 range of the CMD service⁹ where the theoretical isochrones were
208 obtained from (see Sect. 3.4).

The maximum allowed value for the extinction of each
210 cluster was determined through the MCEV¹⁰ reddening maps
211 (Haschke et al. 2011), while the minimum value is always zero.
212 These maps contain a large number of observed areas with as-

⁵ AStECA documentation: <http://asteca.rtfd.org>

⁶ <http://vizier.XXXX>

⁷ <https://github.com/Gabriel-p/mc-catalog>

⁸ <https://github.com/Gabriel-p/mc-catalog-figs>

⁹ CMD: <http://stev.oapd.inaf.it/cgi-bin/cmd>

¹⁰ Magellanic Clouds Extinction Values (MCEV): <http://dc.zah.uni-heidelberg.de/mceextinct/q/cone/form>

Table 3. Fundamental parameters' ranges used by AStECA on our set of 239 OCs. The approximate number of values used for each parameter is N. This gives a combined total of $\sim 2.3 \times 10^7$ possible models, that could be theoretically matched to each studied OC in our sample.

Parameter	Min	Max	Step	N
[Fe/H]	~-2.2	0	~0.1	23
log (age/yr)	6.	10.1	0.05	82
E_{B-V}	0.0	MCEV _{max}	~0.01	~12
μ_{SMC}	18.86	19.06	0.02	10
μ_{LMC}	18.4	18.6	0.02	10
Mass (M_\odot)	10	[1, 3]×10 ⁴	200	[50, 150]

214 signed E_{V-I} extinction values. The TOPCAT¹¹ tool was used to
 215 query a region as small as possible around the positions of each
 216 our OCs, for MCEV reddening values. For approximately 85%
 217 of our sample we found several regions with an associated red-
 218 dening value, within a box of 0.5 deg centered on the OC's po-
 219 sition. For the remaining OCs, larger boxes had to be used to
 220 find regions with assigned E_{V-I} values. The two most extreme
 221 cases are NGC1997 ($\alpha=5^h30^m34^s$, $\delta= -63^\circ12'12''$ [J2000.0])
 222 and OHSC28 ($\alpha=5^h55^m35^s$, $\delta= -62^\circ20'43''$ [J2000.0]) in the
 223 outers of the LMC, where boxes of 4 deg and 6 deg respectively
 224 where needed to find a region with an assigned reddening value.
 225 Once all close-by MCEV regions for an OC are found, the maxi-
 226 mum value MCEV_{max} among all regions is selected as the extinc-
 227 tion range's upper limit. Three steps are used to ensure that the
 228 reddening range is partitioned similarly for all MCEV_{max} val-
 229 ues: 0.01 for MCEV_{max}>0.1, 0.02 if $0.05 \leq \text{MCEV}_{\text{max}} \leq 0.1$, and
 230 0.005 for MCEV_{max}<0.05. The E_{V-I} extinction is converted to
 231 E_{B-V} following Tammann et al. (2003): $E_{V-I}=1.38 E_{B-V}$, with
 232 an extinction law of $R_v=3.1$ applied throughout the analysis.

233 The true distance modulus ranges for the S/LMC Clouds
 234 were assumed to be 18.96 ± 0.1 mag and 18.46 ± 0.1 mag re-
 235 spectively; where the mean values are taken from de Grijs &
 236 Bono (2015) and de Grijs et al. (2014). The 0.1 mag deviations
 237 allowed give depths of ~ 5.7 kpc and ~ 4.6 kpc for the S/LMC.
 238 This covers entirely the line of sight depths found in Subra-
 239 manian & Subramaniam (2009) for both MCs.¹²

240 For the total cluster mass, the range was set to a minimum of
 241 $10 M_\odot$ and a maximum of $10000 M_\odot$. This is true for almost all
 242 the OCs in our sample, except for 15 visibly massive clusters for
 243 which the maximum mass limit was increased to $30000 M_\odot$. The
 244 step used to divide the mass range was $200 M_\odot$, which also sets
 245 the minimum possible uncertainty for a cluster's mass estimate.

246 Finally, the binary fraction was fixed to a value of 0.5 – con-
 247 sidered a reasonable estimate for OCs (von Hippel 2005; Sollima
 248 et al. 2010) – to avoid introducing an extra degree of complexity
 249 into the fitting process. Secondary masses are randomly drawn
 250 from a uniform mass ratio distribution of the form $0.7 \leq q \leq 1$,
 251 where $q=M_2/M_1$, and M_1 , M_2 are the primary and secondary
 252 masses. This range for the secondary masses was found for ex-
 253 ample for the LMC cluster NGC1818 in Elson et al. (1998),
 254 and represents a value commonly used in analysis regarding the
 255 MCs (see Rubele et al. 2011, and references therein).

256 3.2. Center and radius assignment

257 In fully automatic mode, AStECA uses a Gaussian kernel den-
 258 sity estimator (KDE) function to determine the center of the OC

as the point of maximum star density. A radial density profile
 259 (RDP) is used in this same mode to estimate the OC's radius,
 260 as the point where the RDP reaches the star density of the sur-
 261 rounding field.
 262

The first function requires that the density of cluster mem-
 263 bers make the OC stand out over the combination of foreground
 264 and background field stars, and that no other over-density is
 265 present in the observed frame.¹³ The second function will give
 266 good results when the RDP generated is reasonably smooth, and
 267 only if the OC does not occupy the entire observed frame; i.e.:
 268 some portion of the surrounding field must be visible. When
 269 these conditions are not met for either function, the user needs
 270 to run the code on semi-automatic mode. In this mode the center
 271 coordinates can be either manually fixed, or found by the code
 272 based on an initial set of approximate values. Similarly, in semi-
 273 automatic mode the radius must be fixed by the user.
 274

For over ~66% of our OCs sample the center coordinates
 275 were obtained via a KDE analysis, based on initial approxi-
 276 mate values passed to the code. Radii values were calculated by
 277 AStECA for ~60% of the OCs, through an RDP analysis of the
 278 observed surrounding field. The remaining OCs are those that
 279 are highly contaminated, contain very few members, and/or oc-
 280 cupy most of the observed frame. This means that an automatic
 281 obtention of their centers and/or radii is not possible, and the
 282 semi-automatic mode must be used.
 283

The contamination index (CI) calculated by the code, is a
 284 parameter related to the number of foreground/background stars
 285 present in the defined cluster region. A value of $CI=0$ means
 286 that the OC is not contaminated by field stars, $CI=0.5$ means
 287 the overdensity is indistinguishable from the surrounding field
 288 (i.e.: the average number of field stars expected within the clus-
 289 ter region equals the total number of stars in it), and $CI>0.5$
 290 means more field stars are expected within the cluster region than
 291 true cluster members.¹⁴ For reference, the average CI of the set
 292 of OCs with manual radii assignment is $CI \approx 0.9 \pm 0.2$, while the
 293 same average is $CI \approx 0.6 \pm 0.2$ for those OCs where the radius
 294 was automatically estimated. Naturally, more contaminated OCs
 295 are the ones that require more often that the radius be set man-
 296 nually, to prevent the code from employing a wrong value in its
 297 analysis.
 298

299 3.3. Field-star decontamination

A decontamination algorithm (DA) was employed on the CT_1
 300 color-magnitude diagram (CMD) of each processed OC. The DA
 301 allows cleaning the CMD of field-star contamination, before the
 302 isochrone fitting function is used (see Sect. 3.4). The DA must
 303 therefore process all stars within the defined cluster region, i.e.:
 304 the circular region of center and radius either automatically de-
 305 termined by the code or manually fixed by the user.
 306

The Bayesian DA presented in Paper I was improved for
 307 this article; the new DA works in two steps. First, the original
 308 Bayesian membership probability (MP) assignation is applied
 309 to the CMD of all stars within the cluster region (see Paper I
 310 for more details). After that, a cleaning algorithm is used to re-
 311 move stars of low MPs from the CMD, as shown in Fig. 2. To
 312 do this, the full CMD is divided into smaller cells, according to
 313 a given binning method. By default AStECA uses the Bayesian
 314

¹³ The single over-density limitation is planned to be lifted in upcoming versions of AStECA.

¹⁴ See Paper I, Sect. 2.3.2 for a complete mathematical definition of the index.

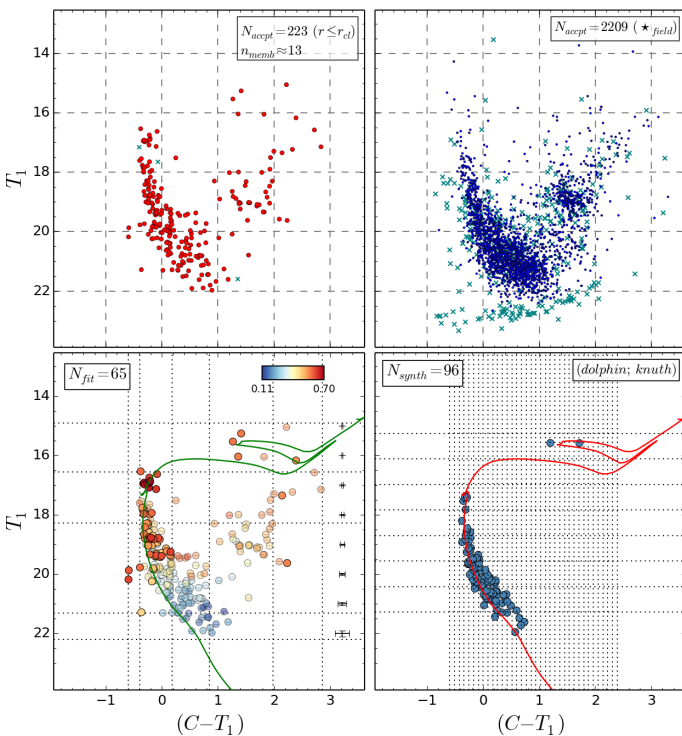


Fig. 2. CMDs for the SMC-L62 cluster. *Top:* CMD of cluster region to the left, where n_{memb} is the approximate number of true members based on the star density of the OC compared to the star density of the field. The CMD of the surrounding field region is shown to the right. In both cases N_{accept} is the number of stars that were not rejected due to their large photometric errors. Rejected stars with large errors are shown as green crosses. *Bottom:* cluster region after the DA is applied is shown to the left; MPs vary according to the colorbar at the top right. Dotted horizontal and vertical lines show the binning used to reject low MP stars cell-by-cell, as obtained via the Bayesian blocks method. Stars that are drawn semi-transparent in each cell are those that were rejected, i.e.: not used in the isochrone fitting process that follows. N_{fit} is the number of stars left after the cell-by-cell rejection. The best fit isochrone is shown in green and red in this CMD, and in the CMD of the best match synthetic cluster to the right (generated from that isochrone), respectively. N_{synth} is the number of stars in the synthetic cluster, and the dotted lines represent the binning obtained using Knuth's rule, applied to the synthetic cluster match process.

blocks method¹⁵ introduced in Scargle et al. (2013), via the implementation of the astroML package (Vanderplas et al. 2012).¹⁶ This second step is similar to the field-star density based cell-by-cell removal algorithm applied in Bonatto & Bica (2007, B07), which uses a simpler rectangular grid. The main difference, aside from the binning method employed, is that AStECA can remove stars cell-by-cell based on their previously assigned MPs, not randomly as done in B07.

For over ~70% of our sample the default settings in AStECA were used in the decontamination process, this is: a Bayesian DA followed by the removal of low MP stars, based on a Bayesian block binning method of the cluster region's CMD. The remaining OCs were processed with modified settings to allow a proper field-star decontamination. This ~30% of OCs are mainly those with a low number of members or a heavily contaminated evolu-

¹⁵ http://www.astroml.org/examples/algorithms/plot_bayesian_blocks.html

¹⁶ While Bayesian blocks binning is the default setting in AStECA, several others techniques for CMD star removal are available, as well as five more binning methods.

tional sequence. Changes in the settings can go from selecting a different binning method (often a rectangular grid using Scott's rule, Scott 1979), to skipping the Bayesian MP assignation and only performing a density based cell-by-cell statistical field star removal. In this latter case, the DA works very similarly to the B07 algorithm.

A correct field-star decontamination is of the utmost importance, as the resulting – hopefully – clean cluster sequence will determine the OCs' fundamental parameters via the isochrone fitting process that follows. Care was thus exercised in this regard, to ensure that non-member stars were properly removed – to the extent possible – from the cluster region of each OC.

3.4. Isochrone fitting

The last part of the automatic analysis performed by AStECA is the isochrone fitting of the OC, to estimate its fundamental parameters. In rigor, the process does not employ isochrones but rather synthetic clusters (SC) generated from theoretical isochrones.¹⁷ In this work we use a PARSEC v1.1 set of isochrones (Bressan et al. 2012, B12). An isochrone of given metallicity and age is combined with a total mass value and the log-normal form of the initial mass function (IMF) defined by Chabrier (2001), to generate a SC with a correct mass distribution. The IMF is stochastically sampled until the desired total cluster mass is reached. The position of this SC in the CMD is then affected by reddening and moved a certain distance modulus value, to obtain the final SC – or model – that will be compared to the OC.

The Poisson likelihood rate (PLR) developed in Dolphin (2002) is employed to assess the goodness of match between the OC and a SC. As the PLR is a binned statistic, it requires binning the CMDs of the OC and all the SCs that can be generated according to the fundamental parameter ranges defined in Sect. 3.1. This part of the analysis uses Knuth's rule (Knuth 2006, also implemented via the astroML package) as the default binning method, see bottom right plot in Fig. 2. The aforementioned Bayesian blocks method results in noticeably larger cells, which means that if applied here some defining features of the evolutionary sequence could be lost. The inverted logarithmic form of the PLR can be written as

$$LPLR = -\ln PLR = \sum_i m_i - n_i + n_i \ln \frac{n_i}{m_i}, \quad (1)$$

where m_i and n_i are the number of stars in the i th CMD cell of the SC and the OC, respectively.¹⁸ In Paper I the total cluster mass parameter could not be estimated, due to the likelihood statistic used (see Paper I, Eq. 11). The LPR defined in Eq. 1 allows us to also consider the mass as a free parameter in the search for the best SC match. Following the validation performed in Paper I for the metallicity, age, extinction and distance parameters, we present in Appendix C a validation study for the total mass. We demonstrate that the masses recovered by AStECA for almost 800 MASSCLEAN synthetic clusters, are in excellent agreement with the true masses used to generate them.

¹⁷ For a detailed description on the AStECA technique for the generation of synthetic clusters from theoretical isochrones, see: Paper I, Sect. 2.9.1

¹⁸ If for any given cell we have $n_i \neq 0$ and $m_i = 0$, a very small number is used instead ($m_i = 1 \times 10^{-10}$) to avoid a mathematical inconsistency with the factor $\ln m_i$.

The best match for an OC is given by the SC that minimizes the LPLR. Since we have five free fundamental parameters, a 5-dimensional surface of solutions is determined by all the possible SCs that can be matched to each OC. ASteca applies a genetic algorithm (GA) on this surface to find the SC that best matches the OC. This SC thus determines the fundamental parameter values that will be assigned to the OC under analysis.

The GA uses a set of reasonable default options which indicate how it performs the search for the best OC-SC match. As with the DA, these options had to be modified – mainly extending the depth of the GA search for the best match – for $\sim 30\%$ of the OCs in the sample. This sub-sample is composed of clusters with particularly complicated morphologies, i.e.: very low number of members, high field star contamination, little to no MS present above the maximum magnitude value observed, etc.

Once the GA returns the optimal fundamental parameter values found for an OC, uncertainties are estimated via a standard bootstrap technique. This process takes a significant amount of time to complete, since it involves running the GA several more times on a randomly generated OC with replacement.¹⁹ Ideally, the bootstrap process would be run hundreds and even thousands of times. This is not possible in practice, as it would be prohibitively costly timewise, so we must settle with running it ten times for each OC in our set.

4. Errors in fitted parameters

It is well known that a parameter given with no error estimation is meaningless from a physical standpoint (Dolphin 2002; Andrae 2010). This fact notwithstanding, a detailed error treatment is usually ignored in articles that deal with star clusters analysis (Paunzen & Netopil 2006). As explained in Sect. 3.4, ASteca employs a bootstrap method to assign standard deviations for each fitted parameter in our OCs sample.

Since the code must simultaneously fit a large number of free parameters – five in this case – within a wide range of allowed values, and using only a 2-dimensional space of observed data (i.e.: the CT_1 magnitudes)²⁰, the uncertainties involved will expectedly be somewhat large. It is worth noting that unlike manually set errors, these are statistically valid uncertainty estimates obtained via a bootstrap process. This is an important point to make given that the usual by-eye isochrone fitting method not only disregards known correlations among all OCs parameters, it is also fundamentally incapable of producing a valid error analysis (Naylor & Jeffries 2006). Any uncertainty estimate produced by-eye serves only as a mere approximation, which will often be biased towards smaller figures. The average logarithmic age error given in the literature, for example, is 0.16 dex, in contrast with the almost twice as large average value estimated by ASteca (see below). In Fig. 3 we show the distribution of the standard deviations versus the five fundamental parameters fitted by the code, for the entire sample (SMC and LMC OCs).

Colors follow the CI obtained for each cluster.

The apparent dependence of the metallicity error with decreasing $[Fe/H]$ values arises from the fact that ASteca uses z values – the linear metallicity measure – to find the best OC-SC

¹⁹ Generating a new OC “with replacement”, means randomly picking stars one by one from the original OC, where any star can be selected more than once. The process stops when the same number of stars as those present in the original OC have been picked.

²⁰ We plan to upgrade the code to eventually allow more than just two observed magnitudes, therefore extending the 2-dimensional CMD analysis to an N-dimensional one.

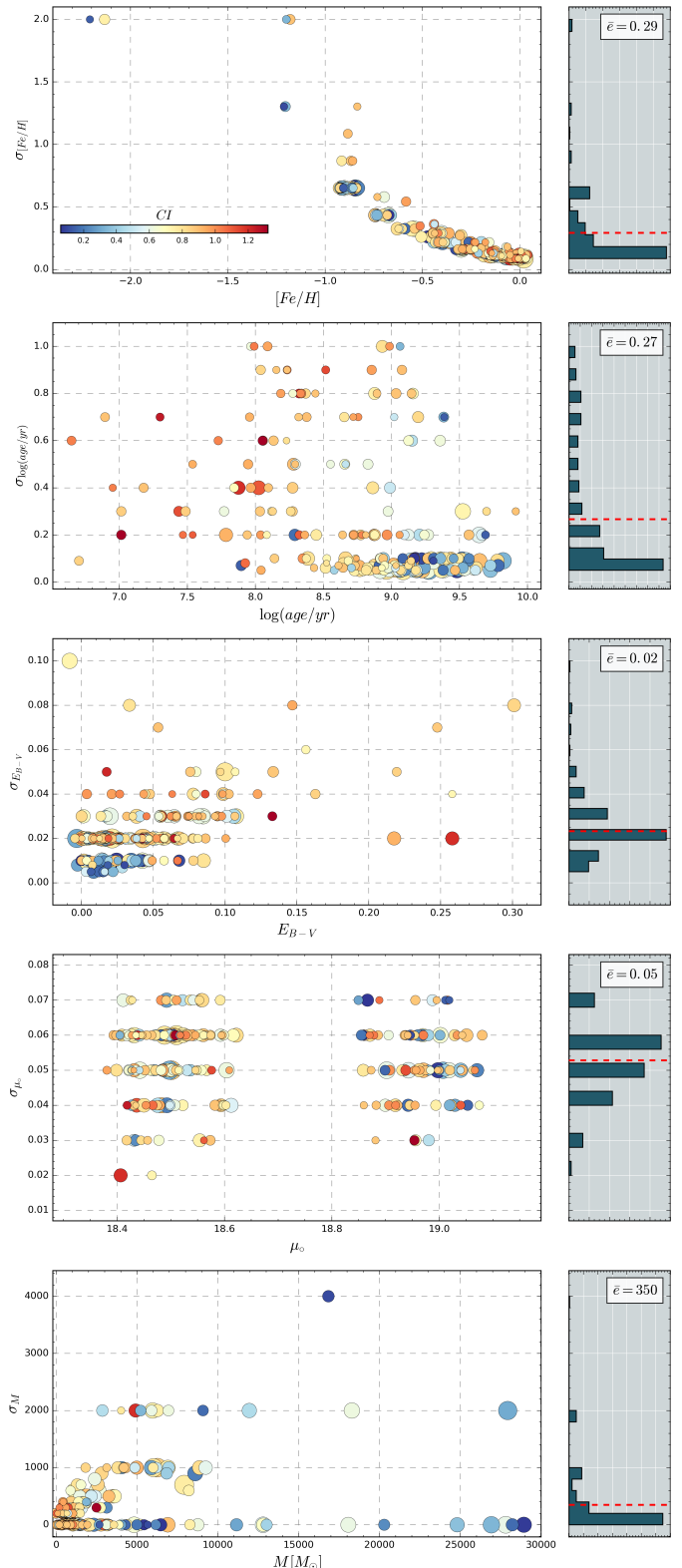


Fig. 3. *Left:* Distribution of errors versus the five parameters fitted by ASteca. Colors are associated to the CI (see bar in top plot), sizes are proportional to the actual cluster sizes. A small random scatter in the x axis is added for clarity. *Right:* Error histogram. The mean error value for each parameter is shown in the top right corner, and drawn in the plot with a dashed red line.

match. The error in z is found to be on average $e_z \approx 0.003$ for all

435 analyzed clusters²¹. This means that, when converting to $e_{[Fe/H]}$
 436 using the relation

$$\sigma_{[Fe/H]} = \sigma_z / [z \times \ln(10)], \quad (2)$$

437 the z in the denominator makes $\sigma_{[Fe/H]}$ grow as it decreases,
 438 while σ_z remains more or less constant. For very small z values
 439 (e.g.: $z=0.0001$), the logarithmic errors can easily surpass
 440 $\sigma_{[Fe/H]}=2$ dex. In those cases, as seen in Fig. 3, the error is
 441 trimmed to 2 dex which is enough to cover the entire metallicity
 442 range.

443 Other than the mathematical dependence of the logarithmic
 444 metallicity explained above, there are no visible trends in the
 445 arrangement of errors for any of the fitted parameters. This is a
 446 desirable feature for any statistical method. If the uncertainties of
 447 a parameter varied (increase/decrease) with it, it would indicate
 448 that AStECA was introducing biases in the solutions.

449 Histograms plotted to the right in Fig. 3 show the distribution
 450 of errors, and their arithmetic means as a dashed red line. The
 451 average metallicity and age errors for the full sample are 0.3
 452 dex and 0.27 dex respectively. For the SMC $\sigma_{[Fe/H]} < 0.2$ dex
 453 for ~34% of the calculated uncertainties. The same relation
 454 is true for ~69% of the LMC OCs, which means that OCs in
 455 the SMC have a larger dispersion in their assigned metallicity
 456 errors. This is due to the lower overall metal content of the SMC
 457 OCs, combined with the effect described above by which the
 458 logarithmic metallicity error increases for smaller [Fe/H] values.
 459 Approximately 53% of the combined S/LMC sample show
 460 $\sigma_{\log(\text{age}/\text{yr})} < 0.1$ dex, a very reasonable uncertainty estimate.
 461 Error estimates for the remaining parameters are all within
 462 acceptable ranges.

463 Numerically, errors could be lowered applying several differ-
 464 ent techniques: increase the number of bootstrap runs, increase
 465 the number of models evaluated in the GA (“generations”), or
 466 reduce the value of the steps in the parameters grid. All of
 467 these methods will necessarily extend the time needed to pro-
 468 cess each cluster, in particular increasing the number of boot-
 469 strap runs. Limited computational time available requires a bal-
 470 ance between the maximum processing power allocated to the
 471 calculations, and the precision one is aiming at. The error values
 472 presented here should then be considered a conservative upper
 473 limit of the accuracy with which the fundamental parameters of
 474 our sample can be obtained by AStECA.

476 5. Comparison with published data

477 We compare in Sect. 5.1 the resulting parameter values obtained
 478 after running AStECA on our set of Magellanic OCs, with those
 479 taken from the original reference articles (those that used the
 480 same Washington photometry used in this work, see Table 1)
 481 referred as the “literature”. The parameters age, extinction, and
 482 mass are also analyzed in Sect 5.2 for a subset of 142 OCs that
 483 could be cross-matched with seven articles (where *UBVRI* pho-
 484 tometry was used, see Table 2), referred as the “databases”.

485 5.1. Literature values

486 The comparison of AStECA versus literature values for the
 487 parameters metallicity, age, extinction and true distance mod-
 488 ulus, is presented in Fig. 4, one parameter per row. The first

489 two plots show the 1:1 identity line for the LMC and the SMC
 490 respectively. The rightmost diagram shows a Bland-Altman
 491 (BA) plot for our combined set of OCs in the MCs, with the
 492 variation in the x axis proposed by Krouwer (Bland & Altman
 493 1986; Krouwer 2008).²² The BA plot shows differences in
 494 the y axis in the sense $\Delta = (\text{AStECA} - \text{litterature})$, versus
 495 values found by the code in the x axis. Errors in Δ values are
 496 calculated combining the errors for both estimates. The mean
 497 of the differences, $\bar{\Delta}$, is shown as a dashed line and its standard
 498 deviation as a gray band.

499 An offset is noticeable for the abundance estimates (first row
 500 of Fig. 4), where AStECA tends to assign values ~0.22 dex larger
 501 than those found in the literature. On average, the offset is of
 502 ~0.27 dex for the SMC and ~0.18 dex for the LMC. This ef-
 503 fect can be explained by three different processes, in light of
 504 our knowledge that the AStECA’s OC-SC best fit matching in-
 505 troduces no biases into the solutions. First, the MC’s star clus-
 506 ters are generally considered to have low metallicities. For ex-
 507 ample, the [Fe/H] values assumed in the 19 literature articles,
 508 are exactly -0.7 dex and -0.4 dex for ~60% and ~75% of the
 509 S/LMC clusters. The by-eye fit is thus very likely biased towards
 510 the assignment of lower abundances. This type of “confirmation
 511 bias” in published values has been studied recently by de Grijs
 512 et al. (2014), in relation to distance measurements reported for
 513 the LMC. Researchers also tend to fit isochrones adjusting it
 514 to the lower envelope of an OC’s sequence; which also con-
 515 tributes to the selection of isochrones of smaller metallicity.²³
 516 Second, the code writes an obtained parameter value to file, us-
 517 ing as many significant figures as those given by the rounded
 518 standard deviation. The standard deviation in turn, is rounded
 519 following the convention of keeping only its first significant fig-
 520 ure. This means for example that a value of $z=0.0005 \pm 0.00312$
 521 will be rounded to $z=0.001 \pm 0.003$. Although this effect is an is-
 522 sue only for cases where the uncertainty is larger – or close to –
 523 the parameter value, it will nonetheless affect smaller metallici-
 524 ties shifting them towards larger estimates.²⁴ Third, AStECA’s z
 525 values are converted to the logarithmic form [Fe/H] using a so-
 526 lar metallicity of $z_\odot=0.0152$ (Bressan et al. 2012). Values found
 527 in the literature, on the other hand, are converted using a solar
 528 metal content of $z_\odot=0.019$ (Marigo et al. 2008). This means that
 529 AStECA will always give [Fe/H] values larger by ~0.1 dex, for
 530 any fitted isochrone of equivalent z being compared, following

$$\begin{aligned}\Delta[\text{Fe/H}] &= [\text{Fe/H}]_{\text{AStECA}} - [\text{Fe/H}]_{\text{litterature}} \\ &= \log(z/0.0152) - \log(z/0.019) = \log(0.019/0.0152) \\ &\approx 0.0969 \text{dex}\end{aligned}\quad (3)$$

These three effects combined can therefore explain the offset
 532 found for the abundances assigned to OCs in the literature versus
 533

²² The BA is also called a “difference” plot or more commonly a “Tukey Mean-Difference” plot. In the original BA plot the default x axis displays the mean values between the two methods being compared. The Krouwer variation changes the means for the values of one of those methods, called the “reference”. In our case, the reference method is AStECA so we use its reported values in the x axis.

²³ The reason is that increasing an isochrone’s metal content moves it towards redder (greater color) values in a CMD, see for example Bressan et al. (2012), Fig 15.

²⁴ This behavior will be changed in the next release of AStECA. The parameter estimates will be written to file keeping more significant figures, to avoid this issue.

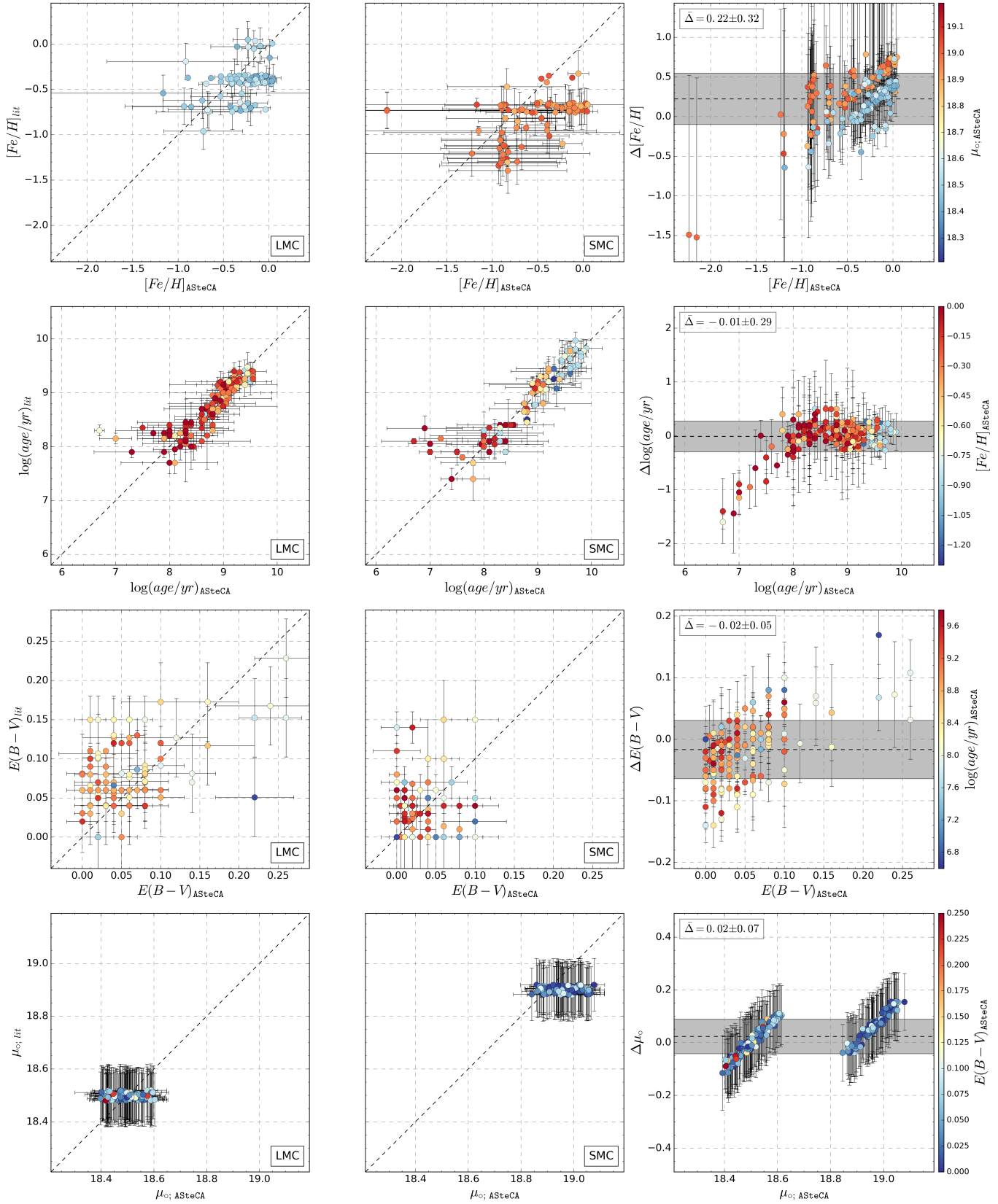


Fig. 4. *Left column:* parameters comparison for the LMC. *Center column:* idem for the SMC. *Right column:* BA plot with differences in the sense ASteCA minus literature, for the combined S/LMC sample. For clarity, a small random scatter is added to both axes for the metallicity and distance modulus plots. Mean and standard deviation are shown as a dashed line and a gray band, respectively; its values are displayed in the top left of the plot. Colors following the coding shown in the bar at the right of the figure, for each row. Piatti (2011b) OCs which contain only age information are plotted with $E_{B-V}=0$ color coding.

those estimated by AStECA. It is important to notice that neither effect is intrinsic to the best likelihood matching method used by the code.

There are two SMC OCs which present an extremely low metallicity: NGC294 ($\alpha=0^h53^m06^s$, $\delta=-73^\circ22'49''$ [J2000.0]) and HW85 ($\alpha=1^h42^m28^s$, $\delta=-71^\circ16'45''$ [J2000.0]). These OCs are positioned close to the SMC's center and towards its periphery, respectively. Both are found to have metallicities of $[Fe/H] \approx -2.2$ dex – with large errors given by AStECA – versus their smaller literature values of -0.7 dex. The code assigns $\log(age/yr)$ values of 8.8 ± 0.06 dex for NGC294, and 9.3 ± 0.7 dex for HW85; while the respective values in the literature are 8.51 ± 0.47 dex and 9.26 ± 0.28 dex. NGC294 has been assigned abundances as low as -1.2 dex (see the integrated spectroscopy study by Dias et al. 2010), although the value obtained by AStECA is substantially lower. HW85 is a little studied cluster with very few members – approximately 20 in our photometric data set – and thus prone to present variations in its estimated parameters. No other published estimation of this cluster's metallicity could be found. The sequence of an OC is broadened towards redder colors by the presence of unresolved binaries. We thus investigate the possibility that our selected fraction of unresolved binaries ($b_f = 0.5$, see Sect. 3.1) could be influencing the selection of these low metallicities. Both OCs are processed five more times setting the b_f factor to [0., 0.25, 0.5, 0.75, 1.], leaving the metallicity to vary as a free variable, and fixing the remaining parameters to the values found by AStECA's original run. If we average these results we find mean metallicities of -1.36 ± 0.08 dex and -1.5 ± 0.2 dex for NGC294 and HW85, respectively. Although these are larger than the original $[Fe/H]$ values, they are still very low metallicity estimates. We can thus rule out the binary fraction used as the responsible factor of these low abundances, and conclude that these are indeed OCs with low metallicities.

The general dispersion between literature and AStECA values can be quantized by the standard deviation of the Δ differences in the BA plot. This value is ~ 0.32 dex (top left of BA plot), in close agreement with the mean internal uncertainty found in Sect. 4 for this parameter. Mean metallicity estimates for the MCs using AStECA values are $[Fe/H]_{SMC} \approx -0.52 \pm 0.44$ dex, and $[Fe/H]_{LMC} \approx -0.26 \pm 0.24$ dex. These averages are more metal rich and disperse, than the ones obtained using literature values: $[Fe/H]_{SMC} \approx -0.78 \pm 0.23$ dex, and $[Fe/H]_{LMC} \approx -0.42 \pm 0.16$ dex

The second row in Fig. 4 shows the age distribution for both Clouds. The overall agreement is very good, with larger deviations from the identity line appearing only for younger ages. There are ten OCs for which AStECA assigned $\log(age/yr)$ values that differ more than 0.5 dex from their literature values. These are referred to as "outliers", and are treated separately in Sect. 5.1.1.

In Palma et al. (2015) an offset is found between star clusters in the LMC fitted with the Girardi et al. (2002, G02) and Bresan et al. (2012, B12) set of isochrones, where OCs fitted with the latter presented consistently larger values. Here we confirm this trend, for ages assigned to our set of OCs for both the SMC and the LMC. While AStECA uses the B12 set of theoretical isochrones, eleven out of the nineteen articles the literature set (see Table 1) used G02 isochrones. The Lejeune & Schaerer (2001, L01) and Marigo et al. (2008) isochrone sets were used by four and two literature articles, respectively; with the remaining two articles applying the δT_1 index to derive ages. In Piatti et al. (2003a,b, 2007a) no significant differences were found between the L01 and the G02 sets, so we assume the same age

offset should be present in the former set. Excluding the outlier OCs described above, the $\Delta \log(age/yr)$ offset for S/LMC clusters between AStECA and literature values are ~ 0.02 dex and ~ 0.05 dex, respectively. The B12 isochrones

The mean value for the $\Delta \log(age/yr)$ parameter in the BA plot, including all S/LMC OCs, is ~ -0.01 dex. This points to an excellent agreement among literature and AStECA values for the $\log(age/yr)$. If we exclude the outliers, the mean of the differences increases by a small amount to ~ 0.04 dex. Similarly to what was found for the metallicity, the dispersion between literature and AStECA values is almost exactly the internal uncertainty found for errors assigned by the code, i.e.: ~ 0.3 dex.

The reddening distribution is relatively small for OCs in both MCs. Maximum E_{B-V} values are ~ 0.15 mag and ~ 0.3 mag for the S/LMC respectively, as shown in the AStECA versus literature identity plots. The Δ differences are well balanced with a mean of -0.02 and a standard deviation of 0.05 mag, slightly larger than the 0.02 mag average uncertainty found for the errors assigned by the code. We obtain average E_{B-V} extinctions for the S/LMC of 0.03 ± 0.03 and 0.05 ± 0.05 , noticeably lower estimates – approximately a third – than those used for example in the Hunter et al. (2003) study of the MCs.

The true distance moduli (μ_o) found by AStECA in both MCs show a clear displacement from literature values. This is expected, as the distance to OCs in the latter is always assumed to be a fixed constant equivalent to the distance to the center of the corresponding galaxy. The distribution of μ_o values found by the code covers the entire range allowed in Sect. 3.1. Distances obtained by AStECA thus vary up to ± 0.1 mag from the default fixed μ_o values used in the literature. It is worth noting that this variation appears to have no substantial effect on any of the remaining parameters, something that could in principle be expected due to the known correlations between all fundamental parameters (see Paper I, Sect. 3.1.4). This reinforces the idea that using a fixed value for the distance modulus, as done in the literature, is a valid way of reducing the number of free variables at no apparent extra cost.

Since masses are only assigned in Maia et al. (2013, M13) for its sample of 29 SMC OCs, the comparison with AStECA is presented separately in Fig. 5. The identity plot (top) shows a trend for AStECA masses to be smaller than those from M13. This is particularly true for two of the OCs with the largest mass estimates – and the largest assigned errors – in M13: H86-97 ($3300 \pm 1300 M_\odot$), and H86-87 ($3100 \pm 1700 M_\odot$). The BA plot (bottom) shows that, on average, M13 masses are $\sim 500 \pm 700 M_\odot$ larger. To explain these differences, we need to compare the way total cluster masses are obtained by M13 and by AStECA in this work.

In M13 masses were determined using two methods, both based on estimating a mass function via the T_1 luminosity function (LF) of an OC. In both cases a field star cleaning process was applied. The first one employs a CMD decontamination procedure (described in Maia et al. 2010), and the second one cleans the cluster region's LF by subtracting it a field star LF. The results obtained with these two methods are averaged to generate the final mass values. Although any reasonable field star cleaning algorithm should remove many or most – depending on the complexity of the OC's CMD – of the foreground/background stars in a cluster region, some field stars are bound to remain. For heavily contaminated OCs this effect will be determinant in shaping the "cleaned" CMD sequence, as true cluster mem-

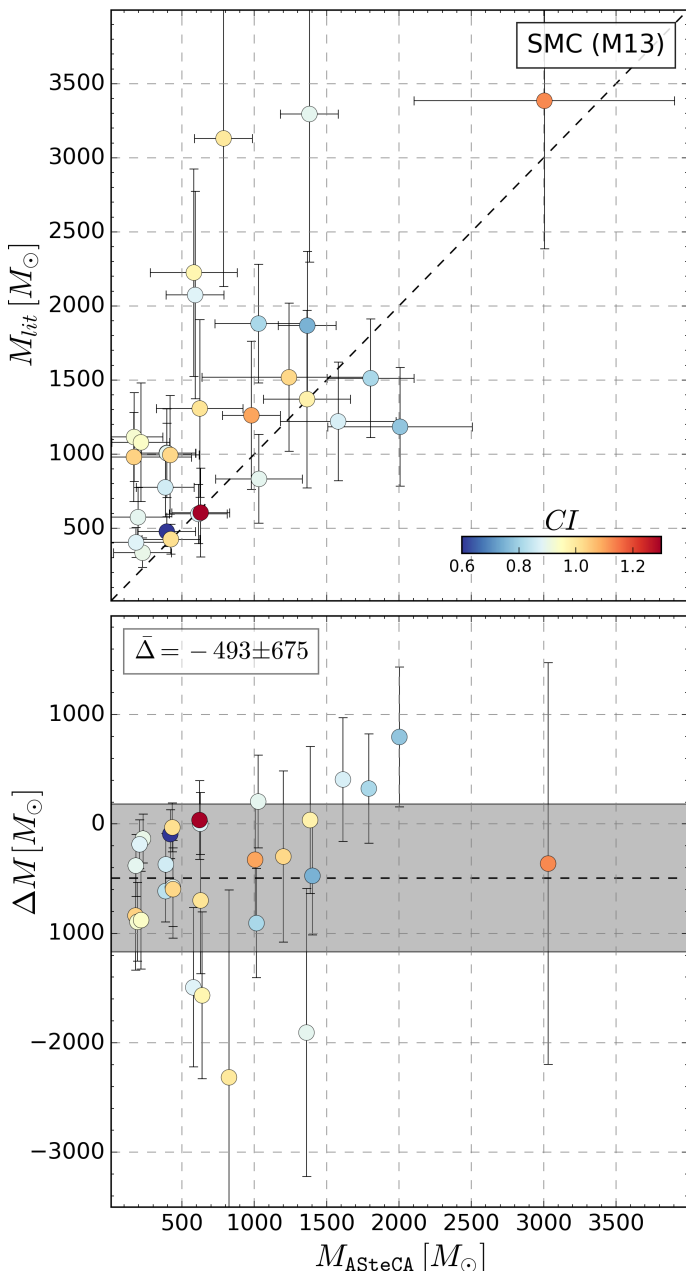


Fig. 5. *Top:* Mass comparison for ASteCA versus literature values. *Bottom:* BA plot with mean and standard deviation of the differences shown as a dashed horizontal line, and a gray band respectively. The mean and standard deviation values are displayed in the top left corner.

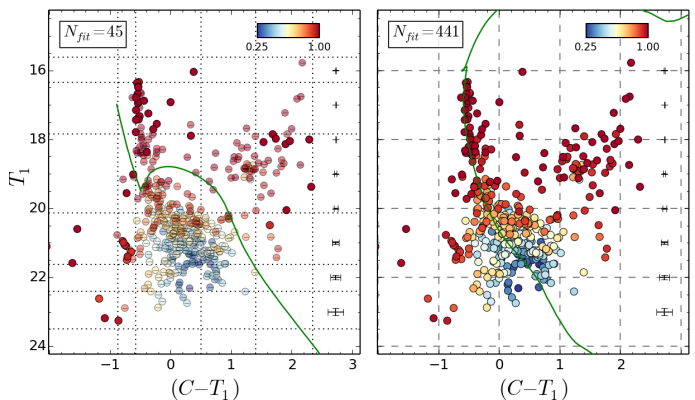


Fig. 6. *Left:* Best fit isochrone for B48 found by ASteCA when a cell-by-cell removal is applied on its sequence, following the Bayesian MP assignation (removed stars are drawn semi-transparent). The estimated age and total mass are $\log(\text{age}/\text{yr})=6.2 \pm 0.6$, and $M=400 \pm 200 M_{\odot}$. *Right:* Best fit isochrone found when no removal of stars is performed, and the full cluster region is used in the search for the best synthetic cluster match. The estimated age and total mass are now $\log(\text{age}/\text{yr})=7.5 \pm 0.3$, and $M=3000 \pm 900 M_{\odot}$.

The case of B48 is worth mentioning, as it is the OC with the largest total mass given in M13 ($3400 \pm 1600 M_{\odot}$). After being cleaned of possible field stars by the DA – see Sect. 3.3 – low mass stars are entirely removed and B48 is left only with its upper sequence ($T_1 < 18.4$ mag). This happens both in the literature and in the analysis done by ASteCA, see left CMD in Fig. 6, and Fig. C8 in M13. The likelihood defined in Eq. 1 sees then no statistical benefit in matching the OC with a SC of a similar age and mass, which will contain a large number of low mass stars. This leads the GA to select as good matches SCs of considerably younger ages ($\log(\text{age}/\text{yr}) < 7.0$ dex) than that assigned in M13 ($\log(\text{age}/\text{yr})=7.9 \pm 0.05$ dex), and with much lower mass estimates (see caption of Fig. 6). A good match both in age and in mass could be found by the code, only if the DA was applied with no cell-by-cell removal of low MP stars as shown in the right CMD of Fig. 6. This means that all stars within the cluster region – including field stars – are used in the SC matching process, which inevitably questions the reliability of the total mass estimate. Dealing with this statistical effect is not straightforward and will probably require an extra layer of modelling added to the SC generation algorithm. As discussed in Sect. 5.1.1 this effect also plays an important role in the significant age differences found between ASteCA and the literature, for a handful of OCs.

5.1.1. Outliers

Ten of the analyzed OCs in this work – approximately 4% of the total 239 clusters present in the set – show a difference in age with literature values of $\Delta \log(\text{age}/\text{yr}) > 0.5$. Such a large age difference translates into two very dissimilar isochrones fitted to the same observed coeval star sequence, which makes this sub-sample of OCs stand out from the rest. For these “outliers” no configuration of the DA plus the employed binning methods could be found, that resulted in SC matches with age values more similar to those found in the literature. In Appendix A, literature and ASteCA isochrone matches are shown for these ten outliers.

Five of these OCs belong to the LMC and the remaining five to the SMC, as shown in Table 4. All the OCs in the outliers sample had smaller ages assigned by the code, compared to their literature values. These differences go from 0.55 dex up to 1.6 dex in the most extreme case of the LMC cluster KMHK975.

bers will be very difficult to disentangle from contaminating field stars. The set of 29 OCs in the M13 sample are indeed heavily affected by field star contamination. This can be seen in Fig. 5, where the color assigned to each OC corresponds to its CI. The minimum value is $CI \approx 0.55$, which means all OCs in the set are expected to contain on average more field stars within the analyzed cluster region, than true members. The presence of a large number of contaminating field stars not only makes the job much harder for the DA, it also necessarily implies that the overall LF will be overestimated, therefore leading – in the case of M13 – to an overestimation of the total mass. In contrast, ASteCA assigns OC masses taking their values directly from the best match synthetic clusters (SCs). Field star contamination will thus have a much lower influence on the code’s mass estimate, limited just to how effective the DA is in cleaning the cluster region.

Table 4. OCs with large differences in their assigned literature ages versus the values found by the code (“outliers”). Equatorial coordinates are expressed in degrees for the $J2000.0$ epoch. Ages are given as $\log(\text{age}/\text{yr})$ for literature (L) and ASteca (A). The difference between both estimates (L-A) is given in the last column as Δ .

Cluster	$\alpha(^{\circ})$	$\delta(^{\circ})$	L	A	Δ
L-KMHK975	82.49583	-67.87889	8.30	6.70	1.60
L-SL579	83.55417	-67.85639	8.15	7.00	1.15
L-BSDL631	76.64167	-68.42722	8.35	7.50	0.85
L-KMHK979	82.41250	-70.98389	7.90	7.30	0.60
L-H88-316	85.41250	-69.22944	8.25	7.70	0.55
S-L35	12.00417	-73.48611	8.34	6.90	1.44
S-H86-188	15.05833	-72.45833	8.10	6.70	1.40
S-L39	12.32500	-73.37167	8.05	7.00	1.05
S-B134	17.25417	-73.20667	8.15	7.20	0.95
S-K47	15.79583	-72.27361	7.90	7.00	0.90

Fig. A.1 (see CMD diagrams *a*) shows the best matches for this OC, where the reason for the different isochrones selected can be clearly seen. While the by-eye isochrone fit done in the literature aligned the brighter part of the OC’s sequence with the turn off point of a ~ 200 Myr isochrone, ASteca decided instead that this was the top portion of a much younger cluster (~ 5 Myr) with no discernible turn off. For almost all of the outliers, the same process can be identified as the main cause responsible for the observed age differences. The statistical mismatch due to the removal of low mass stars by the DA – discussed in Sect. 5.1 – can also be seen to affect some of the fits here. In particular the SMC OCs SL579 and H86-188 show signs of this effect in the best match SCs selected by ASteca (see isochrone fits in Fig. A.1, CMD diagrams *b* and *h*).

These age estimates could be improved – in the sense that they could be brought closer to literature values – if a more restrictive age range was used (e.g.: a minimum value of $\log(\text{age}/\text{yr})=7.5$ dex instead of 6 dex as used in this work, see Table 3). Lacking external evidence to substantiate this a priori restriction, we choose to keep the values obtained by ASteca, with this section acting as a cautionary note.

5.2. Databases values

In addition to the analysis performed in Sect. 5.1, we compare our results with those taken from seven articles – the “databases” or DBs – where a different photometric system was used; see Table 2. We can further separate these seven DBs into two groups: those where the standard by-eye isochrone fitting method was applied – P99, P00, C06, and G10 – and those where integrated photometry was employed to derive the OCs fundamental parameters – H03, R05, and P12. A total of 142 individual OCs from our sample could be cross-matched. Where names were not available to perform the cross-match – databases P00, P99, and R05 – we employed a 20 arcsec radius to find matches, based on the equatorial coordinates of the OCs in each DB.

The comparison of ASteca ages with those from the four isochrone fit DBs is shown in Fig. 7, left and center plot. P99 and P00 analyze SMC and LMC clusters respectively, using Bertelli et al. (1994) isochrones and fixed metallicities for the S/LMC of $z=0.004, 0.008$. While P99 derives individual reddening estimates based on red clump stars, P00 use extinction values determined for 84 lines-of-sight in the Udalski et al. (1999) LMC Cepheids study. The mean S/LMC extinction in P99 and P00 are $E_{B-V}\approx 0.08\pm 0.02$ mag and $E_{B-V}\approx 0.14\pm 0.02$ mag, both larger es-

timates than those found in this work ($E_{B-V}\approx 0.03\pm 0.03$ mag and $E_{B-V}\approx 0.05\pm 0.05$ mag for the S/LMC, see Sect. 5.1). Both studies attempt to eliminate field star contamination following the statistical procedure presented in Mateo & Hodge (1986). The distance moduli for the S/LMC of 18.65 mag and 18.24 mag employed in these DBs, are approximately ~ 0.25 mag smaller than the canonical distances assumed for each Cloud. This has a direct impact on their obtained ages. In de Grijs & Anders (2006) the authors estimate that had P00 used a value of $\mu_0=18.5$ mag instead for the LMC, their ages would be $\sim 0.2\text{--}0.4$ dex younger; a similar conclusion is reached by Baumgardt et al. (2013).²⁵ The same reasoning can be applied to the P99 age estimates. P99 and P00 ages are displaced on average from ASteca values (in the sense ASteca minus DB) by -0.13 ± 0.6 dex and 0.37 ± 0.5 dex respectively, as seen in Fig. 7 left plot. In the case of P99, the distance modulus correction mentioned above would bring the age values to an overall agreement with those obtained by ASteca, although with a large scatter around the identity line. P00 age values on the other hand, would end up ~ 0.7 dex below the code’s age estimates after such a correction. Such a large deviation is most likely due to the overestimated extinction values used by P00, as will be shown below.

C06 studied 311 SMC clusters via isochrone fitting applying two methods: visual inspection and a Monte Carlo based χ^2 minimization. The authors also employ a decontamination algorithm to remove contaminating field stars, making this the article that more closely resembles this present work. Distance modulus is assumed to be $\mu_0=18.9$ mag. Reddening and metallicity values of $E_{B-V}=0.08$ mag and $z=0.008$ are used, adjusted when necessary to improve the fit. It is worth noting that the $[\text{Fe}/\text{H}] = -0.4$ dex abundance employed in C06 is closer to the average $[\text{Fe}/\text{H}] = -0.52\pm 0.44$ dex value found for the SMC by ASteca, than the canonical value of $[\text{Fe}/\text{H}] = -0.7$ dex used by default in most works. This is the DB – out of the four isochrone-fit and the three integrated photometry DBs – that best matches ASteca’s $\log(\text{age}/\text{yr})$ values, with a mean deviation from the identity line of 0.02 ± 0.58 dex.

G10 analyzed over 1500 OCs with ages <1 Gyr in both Clouds via by-eye isochrone fitting. They assumed distance moduli of (18.9, 18.5) mag, and metallicities of (0.004, 0.008), for the S/LMC respectively. Extinction was adjusted also by-eye on a case-by-case basis. The G10 database presents a systematic bias where smaller logarithmic ages are assigned compared to our values, with an approximate deviation of $\Delta \log(\text{age}/\text{yr})\approx 0.23 \pm 0.46$ (ASteca minus G10). This is consistent with the results found in Choudhury et al. (2015) (see Fig. 5), and later confirmed in Piatti et al. (2015b,a). G10 does not apply any decontamination method, by which probable field stars are removed from the cluster’s CMD prior to its analysis. Instead, they plot over the cluster region a sample of surrounding field stars 0.1 arcmin away from the cluster’s radius, taken from a 0.5 arcmin concentric annulus. The lack of a proper statistical removal of contaminating foreground/background stars can cause the isochrone fit to be skewed by their presence.

As seen in the center plot of Fig. 7, these four DBs taken as a single group present a clear age-extinction bias, when compared to ASteca values. This known degeneracy was found in Paper I to be the one with the largest correlation value (see Paper I, Table 3), meaning it is the process most likely to affect

²⁵ Notice that in Baumgardt et al. (2013) the authors correct the age bias that arises in P00 due to the small distance modulus used, increasing P00 age estimates by 0.2 dex. This is incorrect, ages should have been decreased by that amount.

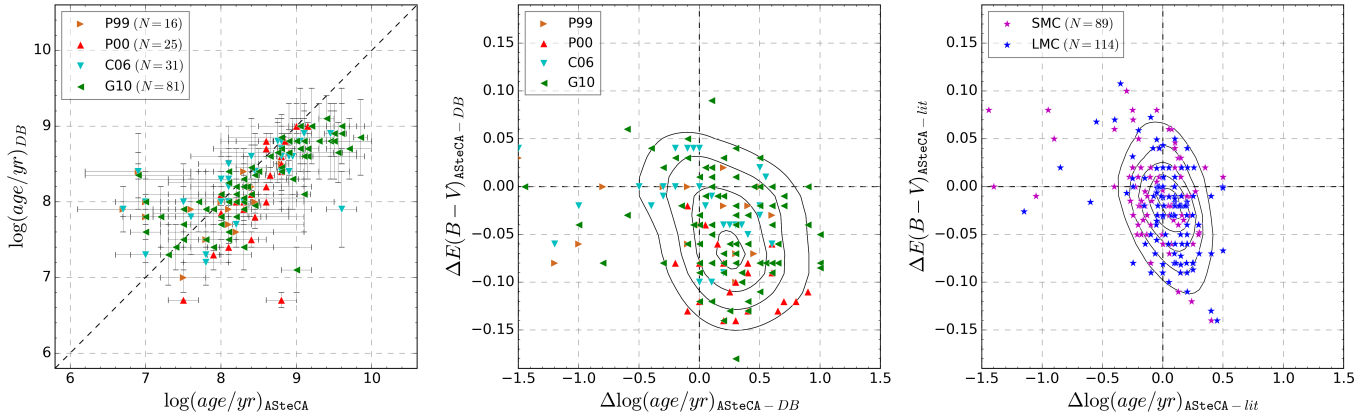


Fig. 7. *Left:* age comparison for DBs that used the isochrone fit method, versus AStECA, where N is the number of OCs cross-matched in each DB. *Center:* “delta” plot, showing the differences between extinction and age, in the sense AStECA minus DB. Curves represent regions of iso-densities after fitting a 2-dimensional Gaussian Kernel. *Right:* same as previous plot, now showing AStECA minus literature values for both Clouds.

isochrone fit studies. The maximum density in this “delta” plot is located around $\Delta E_{B-V} \approx -0.07$ mag and $\Delta \log(\text{age}/\text{yr}) \approx 0.3$ dex. This trend is most obvious for P00 where a rather large average extinction value was employed, compared to the mean value found by AStECA as stated above. For comparison purposes we show in the right plot of Fig. 7 the same delta plot, this time generated subtracting literature values from AStECA age estimations. It can be clearly seen that afore mentioned bias is basically non-existent here, pointing to a consistent overall assignation of extinction and ages by the code.

In Appendix B we show the CMDs of each cross-matched OC for this four DBs (153 in total). The isochrone plotted is the best fit proposed by the corresponding DB, and is compared to the best match found by AStECA. Those OCs that present the largest age discrepancies between AStECA and DBs values, are those where the same effect mentioned in Sect. 5.1.1 takes place. A good example of this is SMC-L39, as seen in Figs. B.9 and B.18 for C06 and G10 respectively.

Our age and mass estimates are also compared with three DBs – H03, R05, and P12 – which used integrated photometry to obtain these parameters (see Table 2). Only H03 and P12 obtained total mass values for the OCs in their sample, these are analyzed in Sect. 5.2.1.

H03 studied approximately 1000 OCs in both MCs – 748 in the LMC and 196 in the SMC²⁶ – via *UBVR* integrated photometry. Ages were assigned based on the Starburst99 model (Leitherer et al. 1999), assuming metallicities, distance moduli, and average E_{B-V} extinction values of (0.004, 0.008), (18.94, 18.48) mag, and (0.09, 0.13) mag, for the S/LMC, respectively. The masses for each OC were derived through their absolute magnitudes M_V and the mass-luminosity relation, assuming -14.55 mag to be the M_V of a 10 Myr old $10^6 M_\odot$ cluster with $z = 0.008$. This article represents, as far as we are aware, the largest published database of MCs cluster masses to date.

R05 used two models – GALEV (Anders & Fritze-v. Alvensleben 2003) and Starburst99 – combined with three metallicities values – (0.004, 0.008) and (0.001, 0.004, 0.008), used in each model respectively – to obtain ages for 195 SMC clusters. This results in five age estimates for each cluster. Individual reddening values are obtained in the same manner as done in the Harris & Zaritsky (2004) study, assigning extinctions accord-

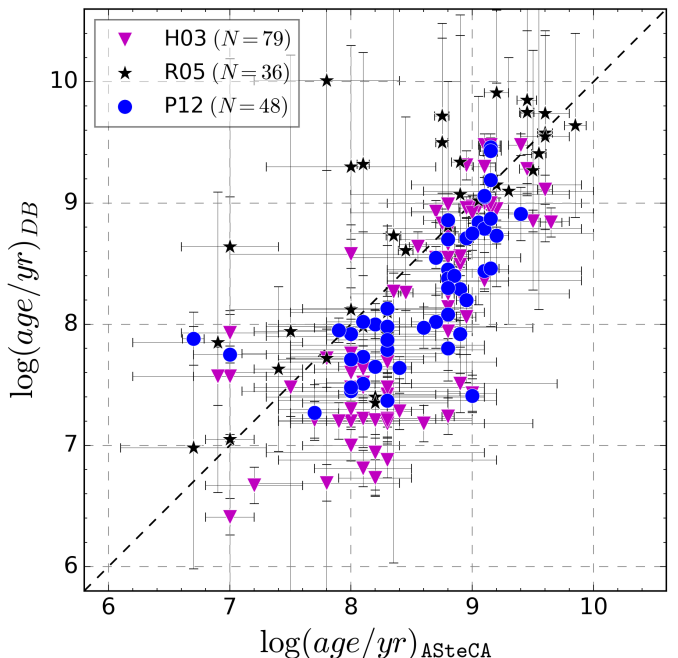


Fig. 8. Age comparison for DBs that used the integrated photometry method, versus AStECA, where N is the number of OCs cross-matched in each DB.

ing to fixed age ranges. We averaged all extinction-corrected age values for each matched cluster, and assigned an error equal to the midpoint between the lowest and highest error bound among all reported ages in the article.

P12 uses the same dataset from H03 to analyze 920 LMC clusters through their MASSCLEAN_{colors} and MASSCLEAN_{age} packages (Popescu & Hanson 2010b,a). Ages and masses from duplicated entries in the P12 sample are averaged in our analysis.

As seen in the identity plot of Fig. 8, H03 visibly underestimates ages for younger clusters. In de Grijs & Anders (2006, see Fig. 1) this effect was also registered, which the authors assigned to the photometry conversion done in H03. The average dispersion between H03 and AStECA logarithmic age values is 0.44 ± 0.56 dex. The same happens for P12 ages, albeit with a smaller mean dispersion in $\log(\text{age}/\text{yr})$ of approximately 0.35 ± 0.44 dex. In P12, their own age estimates are compared with those taken from H03. They find a clear systematic dif-

²⁶ To these numbers, 140 and 76 “questionable” (according to H03) S/LMC clusters respectively, can be added to their sample.

ference with H03 (see P12, Fig. 8), where MASSCLEAN ages are larger than H03 estimates, for OCs with $\log(\text{age}/\text{yr}) < 8$ dex. In our case, most of the OCs cross-matched with P12 are older than 8 dex. Nevertheless the same trend is confirmed, with P12 age values located below the identity line in Fig 8 – i.e.: younger ages compared to ASteca – but still closer than those from H03. This bias towards smaller age estimates by P12 is consistent with what was found in Choudhury et al. (2015). Contrary to the results found for H03 and P12, the R05 study slightly underestimates ages compared to our values, with a mean $\log(\text{age}/\text{yr})$ dispersion of -0.25 ± 0.63 dex around the identity line. The standard deviation is the largest for the three integrated photometry DBs. In R05 the authors mention the lack of precision in their age measurements, due to the use of integrated colors, and the lack of constraints for the metallicity.

Expectedly, the four isochrone fit studies analyzed previously show a more balanced distribution of ages around the 1:1 relation, in contrast with the DBs that employ integrated photometry. Ages taken from integrated photometry studies are known to be less accurate, and should be taken as a rather coarse approximation to the true values. As can be seen in P12, integrated colors present large scatters for all age values, leading inevitably to degeneracies in the final solutions. The added noise by contaminating field stars is also a key issue, as it is very difficult to remove properly from integrated photometry data. A single overly bright field star can also substantially modify the observed cluster's luminosity, leading to incorrect estimates of its parameters (Baumgardt et al. 2013; Piatti 2014). A detailed analysis of some of the issues encountered by integrated photometry studies, and the accuracy of their results, is presented in Anders et al. (2013).

5.2.1. Integrated photometry masses

Masses are obtained in H03 and P12 via integrated photometry analysis. Baumgardt et al. (2013) also derives masses, but as stated in that article, their results are in good agreement with those from P12, so we do not add this database to our work.

There are 127 OCs in the combined H03 and P12 cross-matched samples. In Fig. 9 we show DBs masses for all cross-matched OCs, versus their relative differences²⁷ defined as:

$$\overline{\Delta M_r} = (M_{\text{ASteca}} - M_{\text{DB}})/(M_{\text{ASteca}} + M_{\text{DB}}) \\ = \Delta M/(M_{\text{ASteca}} + M_{\text{DB}}), \quad (4)$$

where DB represents either H03 or P12. Crossed-matched OCs are divided into three regions, according to the masses given in either database. Sizes are scaled with each OC's radius in parsecs, and colors follow the difference in assigned ages $\Delta \log(\text{age}/\text{yr})$, in the sense ASteca minus DB values, as given in the colorbar (see rightmost plot). The minimum CI value for OCs in this set is ~ 0.6 , meaning that they comprise a highly contaminated sample of clusters. The horizontal dashed line in each plot is the combined mean of the relative differences for the assigned masses, $\overline{\Delta M_r}$, for both DBs. The gray band shows the one standard deviation region around the mean.

The average relative differences in the $M_{\text{DBs}} \leq 5000 M_\odot$ low-mass region – left plot in Fig. 9 – is very close to zero, with a

standard deviation of almost ~ 0.5 , equivalent to a multiplicative factor of 3 between ASteca and DBs masses. The mean value of ΔM ($= M_{\text{ASteca}} - M_{\text{DBs}}$), is $\sim 40 M_\odot$ which points to a very reasonable scatter around the identity line. The standard deviation of ΔM is $\sim 1700 M_\odot$, a somewhat large number considering the maximum $5000 M_\odot$ limit for the OCs analyzed. This is nevertheless expected for a set composed of clusters with such small masses. As stated for example in P12 and Baumgardt et al. (2013), low mass OCs – i.e., those with $M \lesssim 5000$ or $10000 M_\odot$ – will tend to have their estimated integrated photometry masses largely dominated by stochastic processes.

A surprising systematic trend arises when we take a closer look at the mass values assigned by the DBs. It can be evidently noticed that the larger the mass estimated by either DB, the larger the relative difference with ASteca's derived value. The left plot in Fig. 9 already shows this trend, albeit disguised by some OCs with positive $\overline{\Delta M_r}$ differences – i.e., with larger masses given by the code – beyond $2000 M_\odot$. If we look at the center and right plots in Fig. 9, where DBs mass estimates $> 5000 M_\odot$ are shown, the trend becomes unmistakable. In these plots we see OCs with DB mass estimates up to $1 \times 10^5 M_\odot$ with ΔM differences of almost $9 \times 10^4 M_\odot$. The most discrepant case of SMC cluster NGC419 had to be left out of the right plot in Fig. 9 for clarity, as it is given a mass of $3.9 \times 10^5 M_\odot$ by H03 and only $2.8 \times 10^4 M_\odot$ by the code. This OC is one of the nine clusters – five in the LMC and four in the SMC – identified by H03 as “extreme” clusters due to their very low absolute magnitude values (see end of Sect. 4 in H03).

The mean and standard deviation for $\overline{\Delta M_r}$ in the medium and large-mass regions shown in the center and right plots of Fig. 9, are $\sim -0.5 \pm 0.3$, and $\sim -0.8 \pm 0.1$ respectively. A mass value estimated by the DBs is thus on average between 3 and 9 times larger than the one calculated by ASteca. The smaller standard deviations for $\overline{\Delta M_r}$ in both these regions, would seem to imply that this is not just a stochastic effect but rather a systematic one.

Considering that integrated photometry studies assign more credibility to higher mass estimates – as they will tend to be less influenced by stochastic fluctuations – this constitutes indeed an unexpected result. It is also in direct contrast with what we show in Appendix C, where the total mass estimation by ASteca is validated using MASSCLEAN synthetic clusters. In that study we found that the relative differences in mass – ASteca minus MASSCLEAN – do not tend to either increase or decrease with the true mass of the cluster. The mass estimations done by ASteca remain close to the actual cluster masses even for low values. The standard deviation of the average relative differences for the three mass regions explored (as shown in Fig. 9), actually decrease for larger masses, as expected, pointing to a more accurate recovery of the mass as the clusters analyzed grow in size.

In Table 5 we show the five OCs with the largest ASteca-DBs mass discrepancies, $\Delta M > 2 \times 10^4 M_\odot$, ordered locating the ones with the larger DB masses on top. CMD plots for each one of these OCs are presented in Appendix D, along with the best match synthetic clusters generated by the code. For the most extreme cases, both DBs assign total masses that are over an order of magnitude greater than the value found by ASteca. Ages are largely in good agreement across the two DBs and this work, for these five OCs. As mentioned previously for the SMC cluster NGC419, H03 assigns a mass that is $3.6 \times 10^5 M_\odot$ – or equivalently 14 times – larger than the mass obtained by the code. Similarly, P12 gives LMC cluster NGC1917 a mass 25 times larger – $\Delta M = 9.6 \times 10^4 M_\odot$ – than the one derived by ASteca.

²⁷ For clarity we employ relative differences here instead of differences as in previous BA plots, since the masses span a large range of values. A $5000 M_\odot$ discrepancy will not carry the same weight if it happens for an OC with estimated masses below $10000 M_\odot$, than if it happens for an OC with estimated masses above $1 \times 10^5 M_\odot$.

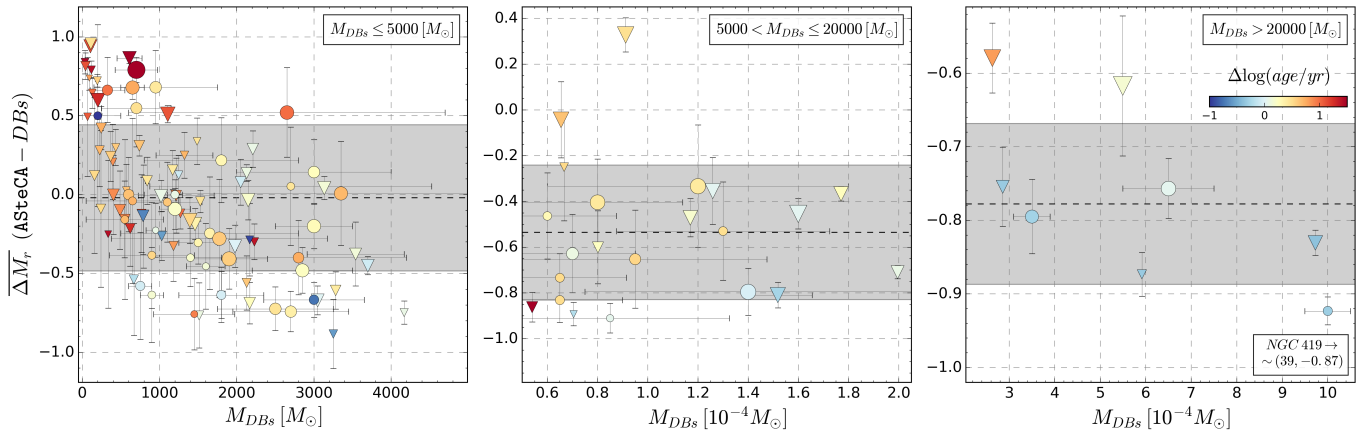


Fig. 9. Left: BA mass plot, showing the differences between estimated masses in the H03 and P12 DBs and the code, in the sense ASteca minus DB; symbols as in Fig. 8. Only DB masses $\leq 5000 M_{\odot}$ are shown here. Colors are assigned according to the difference in $\log(\text{age}/\text{yr})$ estimation of each OC (colorbar is shown in the right plot), while sizes are proportional to the actual sizes in parsecs. The gray band is the mean $\pm 1\sigma$ for the ΔM values (notice that the axis is scaled by $10^{-4} M_{\odot}$). Center: same as previous plot, now showing DB mass values in the range $5000 - 20000 M_{\odot}$. Right: same as previous plot, for DB mass values $> 20000 M_{\odot}$.

Table 5. OCs with large differences ($\Delta M > 20000 M_{\odot}$) in their assigned ASteca masses, versus the values found in the DBs. Equatorial coordinates are expressed in degrees for the J2000.0 epoch. Ages are given as $\log(\text{age}/\text{yr})$.

Cluster	$\alpha(^{\circ})$	$\delta(^{\circ})$	$H03_{\text{age}}$	$P12_{\text{age}}$	$ASteca_{\text{age}}$	$H03_M [M_{\odot}]$	$P12_M [M_{\odot}]$	$ASteca_M [M_{\odot}]$
S-NGC419	17.07917	-72.88417	9.31 ± 0.12	—	8.95 ± 0.05	$\sim 3.9 \times 10^5$	—	$2.8 \pm 0.3 \times 10^4$
L-NGC1917	79.7583	-69.001	9.48 ± 0.09	9.46 ± 0.08	9.15 ± 0.08	$\sim 5.9 \times 10^4$	$1 \pm 0.05 \times 10^5$	$4 \pm 1 \times 10^3$
L-NGC1751	73.550	-69.80694	9.48 ± 0.09	9.06 ± 0.01	9.1 ± 0.05	$\sim 9.7 \times 10^4$	$6.5 \pm 1 \times 10^4$	$9 \pm 1 \times 10^3$
S-L27	10.35	-72.89083	9.28 ± 0.12	—	9.45 ± 0.06	$\sim 5.5 \times 10^4$	—	$1.3 \pm 0.4 \times 10^4$
L-SL244	76.90417	-68.54194	9.48 ± 0.09	9.43 ± 0.01	9.15 ± 0.09	$\sim 2.9 \times 10^4$	$3.5 \pm 0.4 \times 10^4$	$4 \pm 1 \times 10^3$

992 A possible explanation for this large divergence in the calcu-
993 lated masses, is the presence of contaminating field stars. To test
994 this hypothesis we re-processed with ASteca all OCs in Table 5,
995 this time with no previous decontamination process applied. This
996 means that all stars within the cluster region, including field stars
997 in the same line of sight, will be employed in the obtention of the
998 best synthetic cluster match. The upper limit for the total mass
999 is set to $5 \times 10^5 M_{\odot}$, to avoid biasing the results by setting a low
1000 total mass value. For LMC cluster SL244 the total mass value
1001 obtained this way is $3 \times 10^4 M_{\odot}$, meaning its average DB mass
1002 is recovered when no field stars cleaning is performed. The best
1003 synthetic cluster match for SMC cluster L27 results in an even
1004 higher total mass of $1 \times 10^5 M_{\odot}$. These two cases clearly highlight
1005 the importance of a proper field star decontamination, before the
1006 method to derive an OC's mass is applied.

1007 For the remaining three OCs – S-NGC419, L-NGC1917, and
1008 L-NGC1751; the most massive according to H03 and P12 – the
1009 masses derived by ASteca using the contaminated cluster region
1010 fall short from the values assigned by the DBs. The closest match
1011 is found for LMC clusters NGC1751 and NGC1917, for which
1012 a mass of $2 \times 10^4 M_{\odot}$ is estimated by the code while their average
1013 DB mass is $\sim 8 \times 10^4 M_{\odot}$. In the case of SMC cluster NGC419, the
1014 recovered ASteca mass using the entirety of stars in its observed
1015 field is $5.5 \times 10^4 M_{\odot}$, still seven times smaller than the value given
1016 by H03. The radius used for NGC419 in our case is larger than
1017 the one employed in H03 by more than 20% ($\sim 85''$ versus $\sim 70''$),
1018 so we can be sure that this effect is not related to a lack of stars
1019 included within the cluster region.

1020 These three OCs share a common extra attribute beyond being
1021 the ones with the largest assigned masses in both DBs, and
1022 showing the largest discrepancies with ASteca mass values: they
1023 are all identified as clusters presenting the controversial “dual

1024 red clump” (dRC) structure (Girardi et al. 2009). This feature 1025 was predicted in Girardi et al. (1998) as a grouping of stars with 1026 enough mass to ignite helium, while avoiding e^- -degeneracy. 1027 The quantitative effect of the dRC structure, on the integrated 1028 magnitude of a cluster, was tested on synthetic MASSCLEAN 1029 clusters of varying masses. We found that adding a secondary 1030 RC composed of about $\sim 15\%$ of the stars present in the main 1031 RC (the approximate value found for NGC419 in Girardi et al. 1032 2009), has a very small effect on the synthetic cluster’s integrated 1033 V magnitude, as well as its (B-V) color.²⁸ For a 1 Gyr synthetic 1034 cluster of $10000 M_{\odot}$, adding stars to form the dRC – located ~ 0.3 1035 mag below the RC, and ~ 0.04 mag towards the bluer region of 1036 the (B-V) vs. V CMD – results in the integrated V band (and 1037 the integrated (B-V) color) increasing only a few hundredths of 1038 a magnitude. At the same time, just doubling the mass of the 1039 synthetic cluster, i.e. $20000 M_{\odot}$, increases the integrated V band 1040 value almost a full magnitude. This difference is large enough 1041 to assume that the H03 and P12 models will not mistakenly as- 1042 sign large masses, based on such a small variance in integrated 1043 photometry as that produced by a dRC. The excess brightness 1044 generated by stars in the dRC region of these three OCs, would 1045 thus appear to not be enough to explain the overestimated total 1046 mass values given by H03 and P12 (in particular to NGC419 by 1047 H03).

1048 In addition to the presence of a dRC, both NGC419 1048 and NGC1751 show extended or multiple main-sequence 1049 turnoffs (MSTO; see: Glatt et al. 2008; Milone et al. 2009; 1050 Rubele et al. 2010, 2011; Girardi et al. 2011) while NGC1917 1051 is known to posses a broadened MSTO (Milone et al. 2009). 1052

²⁸ Where both V and B filters correspond to the Johnson photometric system.

The origin of this structure is still under debate, as seen in Piatti & Bastian (2016), Milone et al. (2016), and Li et al. (2016). Its influence on the derived masses from integrated photometry studies is not straightforward to assess, nor can its impact be easily discarded.

If we examine the H03 and P12 databases, we find that the aforementioned bias – by which integrated photometric studies increasingly overestimate masses for larger mass OCs – exists even when comparing these studies among themselves. After removing duplicated entries in both DBs, and cross-matching them with a maximum search radius of 20 arcsec, we are left with 670 unique LMC OCs across H03 and P12. Fig. 10 shows BA diagrams for these cross-matched OCs. We plot here the average P12-H03 mass \bar{M}_{DBs} versus their relative difference $\Delta\bar{M}_r$, as defined in Eq. 4, in the sense P12 minus H03. As done previously, masses are separated into three regimes for clarity. There are only five OCs that show average masses larger than $100000 M_{\odot}$, and they are all massive globular clusters which are incorrectly assigned a low age and mass by P12.²⁹ For example, the LMC globular cluster NGC1835 is correctly identified by H03 as an old ~ 5 Gyr system, with a total mass of $\sim 1.4 \times 10^6 M_{\odot}$ (a reasonable value, although a bit overestimated, according to Du-bath et al. 1990). P12 on the other hand classifies this as an extremely young ~ 6.3 Myr OC with a very low total mass estimate of $1700 M_{\odot}$.

In Fig. 10 we see that, as the average OC mass given by these DBs increases, so do their relative differences. The mean values of $\Delta\bar{M}_r$ decreases from $\sim 0.5 \pm 0.4$ in the low mass region, to $\sim -0.1 \pm 0.4$ in the medium OC mass region, to $\sim -0.4 \pm 0.6$ in the large mass region. Masses go from being overestimated a factor of 3 by P12 – in relation to H03 – in the low mass region, to being underestimated by a factor of more than 2 in the large mass region. These differences in total mass grow with larger average masses, in a way that is closely related to the difference in the $\log(\text{age}/\text{yr})$ values estimated by each DB. Where P12 estimates larger masses than H03 – i.e., the low mass region – it also assigns larger ages by more than 1.5 dex. Conversely, in the large average mass region, P12 ages can reach differences of up to 3 dex lower than H03. This age-mass positive correlation, by which an older large cluster can be incorrectly identified as a much younger and less massive one or vice-versa, is also noticeable in Fig. 9 albeit to a lesser extent. In Fig. 11 we show how the age-mass correlation affects DBs estimates compared to those taken from AStECA (left plot), and how this effect is much stronger in P12 and H03 estimates (right plot).

About $\sim 17\%$ of the OCs in H03 and P12, are assigned masses above $5000 M_{\odot}$ in their respective DBs. A smaller percentage, less than $\sim 8\%$ and $\sim 5\%$, are assigned by those works mass values above $10000 M_{\odot}$ and $20000 M_{\odot}$ respectively. Similar proportions are found when inspecting AStECA's obtained masses. Clusters with relatively large masses represent – as demonstrated by the aforementioned percentages – a small portion of OCs in the DBs. Nonetheless, care should be taken when applying their integrated photometry estimated masses to the study of properties such as the initial cluster mass function (ICMF). Large discrepancies in the mass value assigned for the most massive OCs, could have a non-negligible impact on the slope of the IMCF.

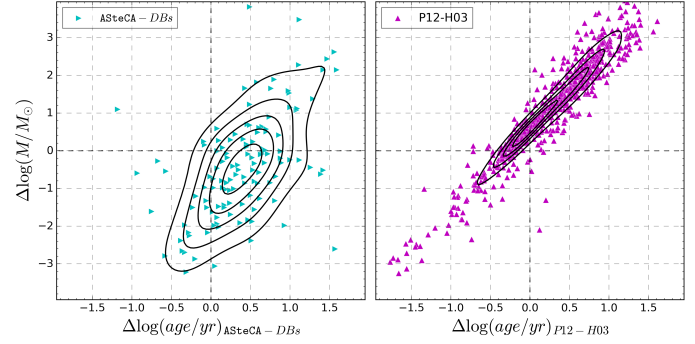


Fig. 11. Top: Differences plot for AStECA minus the combined P12 and H03 DBs. Horizontal and vertical axis show differences in $\log(\text{age}/\text{yr})$, and $\log(M/M_{\odot})$, respectively. A 2-dimensional Gaussian kernel density estimate is shown as iso-density black curves. Bottom: idem, for ages and masses of P12 and H03 cross-matched OCs, in the sense P12 minus H03.

6. Parameters distribution

1112

We present here a summary of the distribution of fundamental parameter values obtained with AStECA, for our set of 239 Magellanic Clouds clusters.

1113

In astrophysics analysis, histograms are widely used to derive a large number of properties when a substantial amount of data is available. A galaxy's star formation history (SFH) is a good example of such a property, almost always quantified via a one-dimensional histogram. Their widespread use notwithstanding, the generation of a histogram is affected by well known statistical issues; see Silverman (1986), Simonoff & Udina (1997). Different selected bin widths and anchor positions (point of origin) can make histograms built from the exact same data look utterly dissimilar. In the worst cases, completely spurious structures may appear, leading the analysis towards erroneous conclusions. We bypass these issues by constructing an adaptive (or variable) Gaussian kernel density estimate (KDE) in one and two dimensions, using the standard deviations associated to a given parameter as the bandwidth estimates. The formulas for both KDEs are:

$$KDE_{1D}(x) = \frac{1}{N \sqrt{2\pi}} \sum_{i=1}^N \frac{1}{\sigma_i} e^{-\frac{(x-x_i)^2}{2\sigma_i^2}}, \quad (5)$$

$$KDE_{2D}(x, y) = \frac{1}{2\pi N} \sum_{i=1}^N \frac{1}{\sigma_{xi}\sigma_{yi}} e^{-\frac{1}{2}\left(\frac{(x-x_i)^2}{\sigma_{xi}^2} + \frac{(y-y_i)^2}{\sigma_{yi}^2}\right)}, \quad (6)$$

where N is the number of observed values, x_i is the i th observed value of parameter x , and σ_{xi} its assigned standard deviation (same for y_i and σ_{yi}). The 1D version of these KDEs is similar to the “smoothed histogram” used in the Rafelski & Zaritsky (2005) study of SMC clusters. The use of standard deviations as bandwidth estimates means that the contribution to the density map (in 1D or 2D) of parameters derived with large errors, will be smoothed (or “spread out”) over a large portion of the parameter's domain. Precise parameter values on the other hand – i.e. those with small assigned errors – will contribute to a much more narrow region, as one would expect.

1142

Replacing one and two-dimensional histogram analysis with these KDEs has two immediate benefits: a) it frees us from having to select an arbitrary value for the bandwidth (the most important component of a KDE, equivalent to the bin width of a

²⁹ These five LMC globular clusters are: NGC1916, NGC1835, NGC1786, NGC1754, and NGC1898. P12 assigns masses below $2000 M_{\odot}$ in all cases.

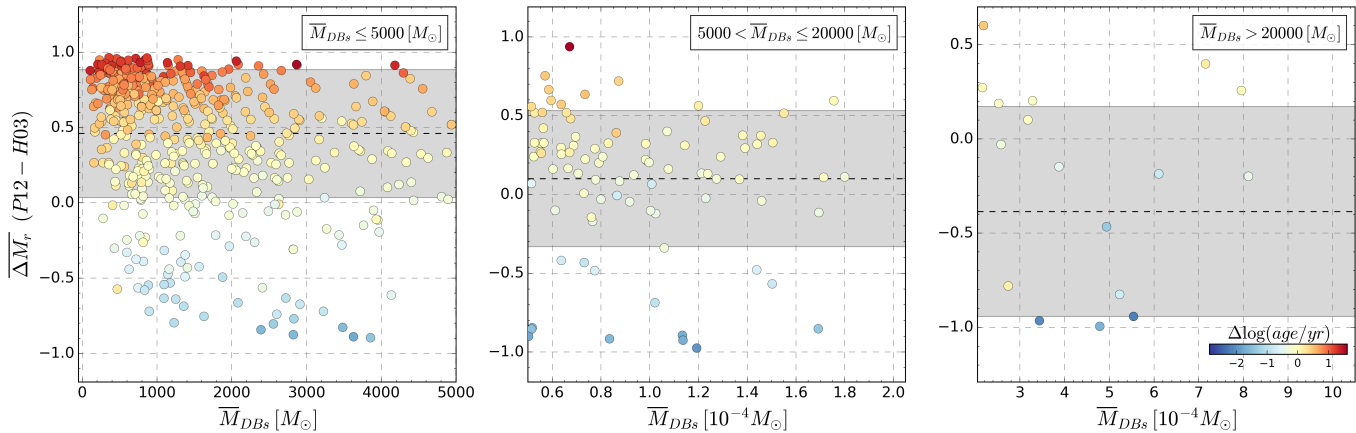


Fig. 10. *Left:* BA plot for the relative difference between P12 minus H03 masses, for average mass values below $5000 M_{\odot}$. OCs are colored according to the difference in their assigned logarithmic ages by each DB – i.e.: $\Delta \log(\text{age}/\text{yr})$ – in the sense P12 minus H03; see colorbar in the rightmost plot. The mean and standard deviation for ΔM_r is shown as a dashed black line and a gray region, respectively. *Center:* idem, for average DB masses $5000 < \overline{M}_{DB} < 20000 (M_{\odot})$. *Right:* idem, for average DB masses $\overline{M}_{DB} > 20000 (M_{\odot})$.

regular histogram), and b) it naturally incorporates the errors obtained for each studied parameter into its derived probability density function. Figs. 12 and 13 show 1D and 2D density maps constructed via Eqs. 5 and 6, for two paired parameters, for each of the MCs. Being probability density functions means that the area under the curve integrates to unity. This makes the distributions for a given parameter comparable for both galaxies, even if the number of observed points – clusters in our case – is not the same (equivalent to a normalized histogram).

Based on the analysis of a database of over 1500 OCs, G10 reports two periods of enhanced cluster formation in the MCs: around 160 Myr and 630 Myr for the SMC, and around 125 Myr and 800 Myr for the LMC. A third period is reported at approximately 8 Myr for both MCs. To obtain these results, the authors construct histograms of their data, combined with data from P00 and C06 (see Figs. 5 and 6 in G10). They analyze the peaks found in both histograms and conclude that the formation episodes are correlated, as they happened around the same period of time. This is a good example of the issues mentioned at the beginning of this section, regarding histogram construction. If we look at the 1D $\log(\text{age}/\text{yr})$ KDEs in Fig. 12 (top), we see that most of the enhanced formation periods reported in G10 are not present. A distinct period of cluster formation is visible in the LMC starting around the ~ 5 Gyr mark, which lasted up to ~ 1.3 Gyr ago. A similar, but much less pronounced peak is seen for the SMC, with a clear drop in cluster formation around ~ 2 Gyr. The height difference between the SMC and LMC KDEs is related to the decline in cluster formation. While the LMC sharply drops to almost zero from ~ 1 Gyr to present times, the SMC shows a much softer descent with smaller peaks around ~ 250 Myr and ~ 130 Myr. The well known “age gap” in the LMC between 3–10 Gyrs (Babbinet et al. 2010) is present, visible as a marked drop in the $KDE_{\log(\text{age}/\text{yr})}$ curve at approximately ~ 9.5 dex. No clusters older than this age are found in our work.

The 2D KDE age-metallicity map shows how spread out these values are for OCs in the SMC, compared to those in the LMC which are much more heavily clustered together. Although in this map the abundance of the SMC can be seen to reach substantially lower values than the LMC, the 1D KDE to the right reveals that the $[\text{Fe}/\text{H}]$ parameter peaks between 0 dex and -0.2 dex, for OCs in both clouds.

The age-mass 2D map shows a clustering around younger ages and smaller masses for the LMC, relative to the SMC. The

OC seen in the bottom right corner of the age-mass SMC map is HW42 ($\alpha=1^{\text{h}}01^{\text{m}}08^{\text{s}}$, $\delta=-74^{\circ}04'25''$ [J2000.0]), a small cluster (radius <20 pc) located close to the SMC’s center. Though its position in the map is somewhat anomalous, the 1σ error in its age and mass estimates could move it to $\log(\text{age}/\text{yr}) \approx 9.4$ and $\log(M/M_{\odot}) \approx 2.6$. This OC is classified as a possible emissionless association by Bica & Schmitt (1995).

In both clouds there is a tendency for the mass and the size of the OC, to grow with the estimated age, as expected. In the 1D mass KDE, we see that the LMC accumulates most OCs in the low mass regime ($\sim 3000 M_{\odot}$). This is also true for the SMC which has a larger proportion of large mass OCs, with a distinctive peak around $\sim 30000 M_{\odot}$.

As seen in Fig. 13 (top), the 1D KDEs of the true distance moduli are well behaved and clearly normal in their distribution. A Gaussian fit to these curves results in best fit values of 18.96 ± 0.08 mag for the SMC, and 18.49 ± 0.08 mag for the LMC. The initial ranges given in Table 3, as well as the literature mean distances, are thus properly recovered. Extinction values are much more concentrated in the SMC around $E_{B-V} \approx 0.015$ mag. The OCs in the LMC on the other hand, show that most values are dispersed below $E_{B-V} \approx 0.1$ mag, with a shallower peak located at ~ 0.03 mag.

6.1. Age-metallicity relation

A stellar system’s age-metallicity relation (AMR) is an essential tool to learn about its chemical enrichment evolution. This relation is usually presented either as scattered single points in the age-metallicity space, or as a function created by grouping and averaging metallicity estimates in arbitrary age bins. In Piatti (2010) a method was devised to generate an AMR able to take into account the errors in age values, to produce bins of different sizes. This method has been applied to the obtention of AMRs in Piatti & Geisler (2013), and also adapted to derive star cluster frequency distributions (e.g., Piatti 2013).

We can take advantage of the KDE technique described in Sect. 6 – used to produce two-parameters density maps – to generate an AMR that is truly representative of the observed data, with some important improvements over previous methods. First, a Gaussian density map has no dependence on the number, size (fixed or variable) or location of bins, as a regular histogram

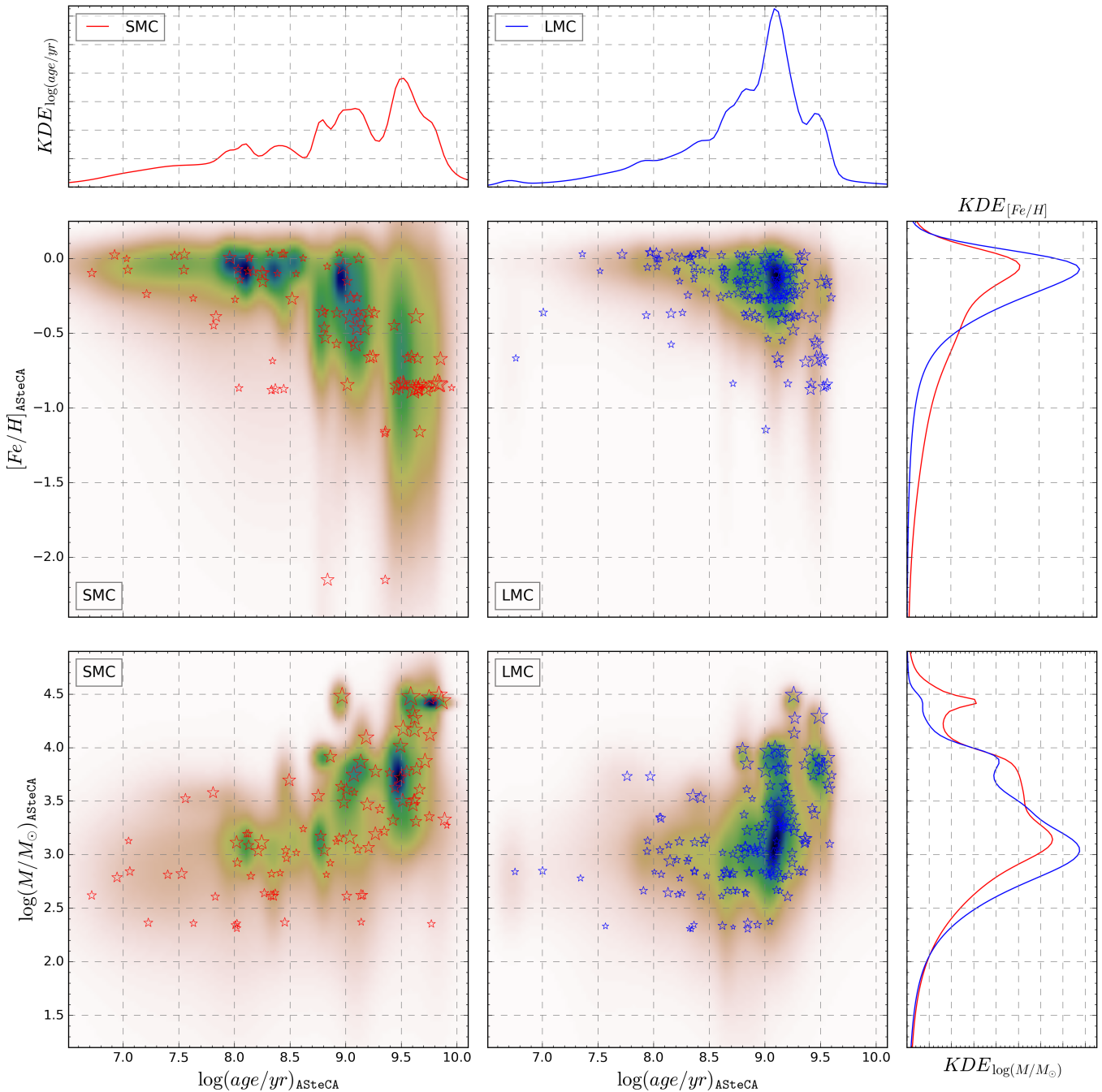


Fig. 12. One and two-dimensional Gaussian adaptive KDEs for the age, metallicity and mass parameters. Top and right plots are 1D KDEs while the center plots are 2D KDEs. Observed clusters are plotted as red and blue stars for the S/LMC, respectively in the 2D KDEs. Sizes are scaled according to each OC's radius in parsecs. A small scatter is introduced for clarity.

1230 or the aforementioned method would. Second, the errors in the
 1231 two parameters used to obtain the density map (age and metal-
 1232 licity), are organically included in the function that generates it
 1233 (as explained in Sect. 6). This means that no ad-hoc procedure
 1234 is required to incorporate the important information carried by
 1235 these values, into the final AMR.

1236 The process of creating an AMR function³⁰ requires that we
 1237 associate a unique $[Fe/H]$ to a single age value, for the available
 1238 age range. After generating the age-metallicity 2D density map,
 1239 a dense 2D grid is created dividing it into N steps of 0.01 dex

1240 width, covering the ranges of both parameters. Every point in
 1241 this grid is evaluated in the KDE map and its value (w_i) is stored,
 1242 along with its age-metallicity coordinates (age_i , $[Fe/H]_i$). Each
 1243 of the N ages defined in the grid is then associated to a single
 1244 representative $[Fe/H]$ value. This representative metallicity for a
 1245 given age is obtained as the mean metallicity value, weighted by
 1246 the KDE function at that particular age. The formal equation for
 1247 obtaining it, can be written as

$$[Fe/H]_{age_i} = \frac{\sum w_i [Fe/H]_i}{\sum w_i} \quad (7)$$

³⁰ By “AMR function” we mean a curve that spans the entire observed age range, mapping each age value to a single metallicity value.

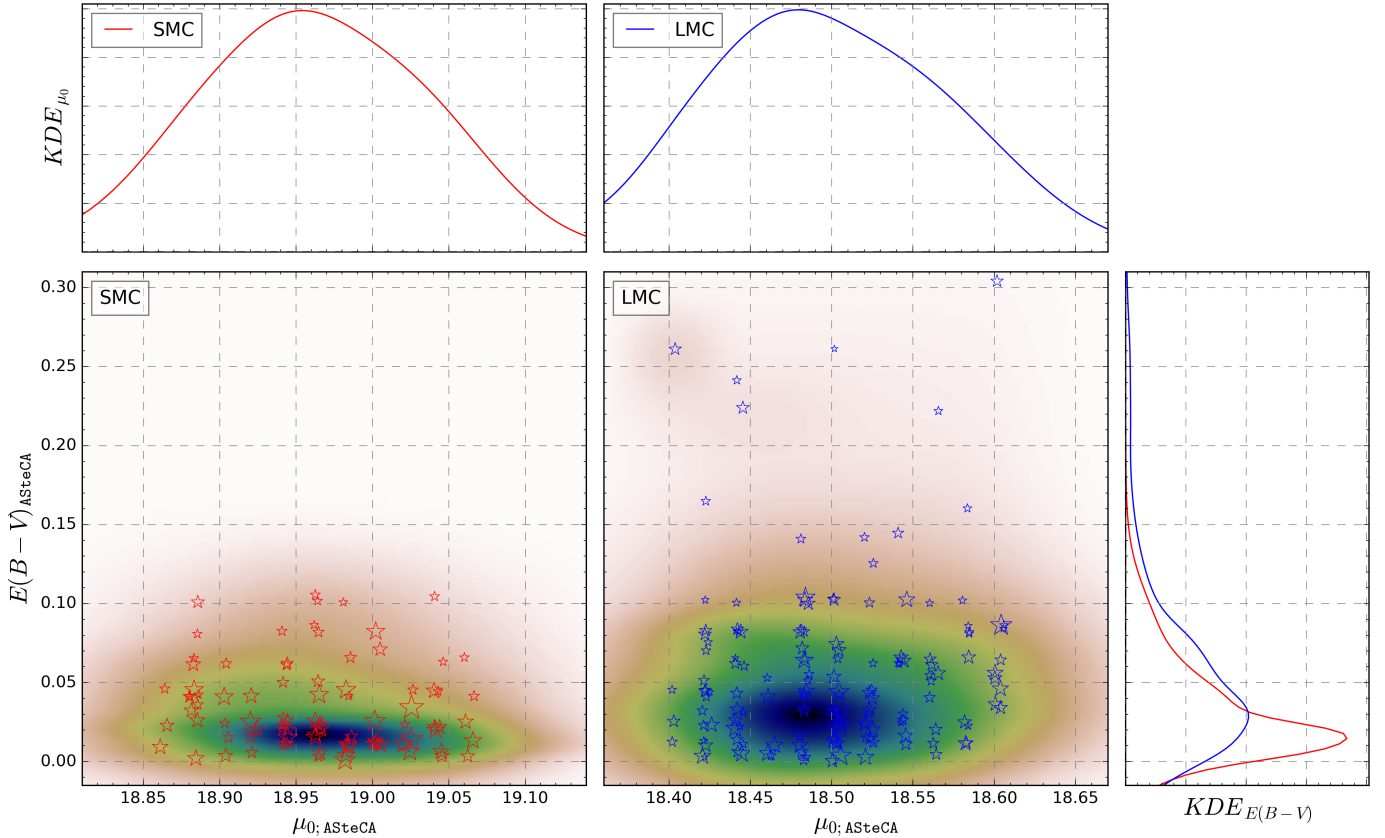


Fig. 13. Same as Fig. 12 for the extinction and distance modulus parameters.

where the summations are performed over each i step for the N defined steps in the metallicity range, $[Fe/H]_i$ is the metallicity value at step i , and w_i is the value of the 2D KDE map for that fixed age and metallicity coordinates. The age_i subindex in Eq. 7 indicates that this mean metallicity was calculated for a fixed age value, and thus represents a unique point in the AMR. A similar version of this weighted metallicity was employed in Noël et al. (2009, see Eq. 3) to derive AMR estimates for three observed fields. We apply the above formula to all the N ages in the grid defined at the beginning of the process. The standard deviation for each $\overline{[Fe/H]}_{age_i}$ value is calculated through the equation

$$\sigma_{age_i}^2 = \frac{\sum w_i \sum [w_i ([Fe/H]_i - \overline{[Fe/H]}_{age_i})^2]}{(\sum w_i)^2 - \sum w_i^2} \quad (8)$$

where again all summations are applied over N, and the descriptions given for the parameters in Eq. 7 apply. At this point, this method already gives us an AMR function estimate, since every age step is mapped to a unique metallicity. The downsides are that the AMR is noisy due to the very small step of 0.01 dex used, and that the associated errors are quite large. This latter effect arises because the weighted standard deviation, Eq. 8, will be affected not only by the errors in both measured parameters – through the constructed 2D KDE map – but also by the intrinsic dispersion in the metallicity values found for any given age. To solve this, we calculate the average $[Fe/H]$ for a given age interval, rather than assigning a metallicity value to each age step in the grid. Dividing the age range into intervals requires a decision about the step width, much like when constructing a histogram, bringing back the issue of binning. We have two advantages here: a) we use Knuth's algorithm (see Sect. 3.4) to obtain the optimal

binning for our data, and b) the final AMR function is very robust to changes in the binning method selected, so even the previous choice is not crucial in determining the shape of our AMR. Finally, the $\overline{[Fe/H]}_{age_i}$ values obtained for every age_i within a defined age interval, are averaged. Errors are propagated through the standard formula, disregarding covariant terms (Bevington & Robinson 2003, Eq. 3.14).

The final AStECA AMRs for the S/LMC can be seen in Fig. 14 as red and blue continuous lines, respectively. Stars show the position of all OCs in our sample for each galaxy, with sizes scaled according to their radii. The shaded regions represent the 1σ standard deviations of the AMR functions. These regions span a $[Fe/H]$ width of approximately 0.2 dex for both Clouds, for the entire age range. The blue (top) and red (bottom) vertical segments in the top plot are the bin edges determined for each age interval by Knuth's algorithm, for the LMC and the SMC respectively. As stated previously, the final AMR functions are mostly unaffected by the chosen binning method. Using Knuth's algorithm results in approximately 12 age intervals of widths between 0.35 and 1 Gyr, as seen in Fig. 14. If instead we use 100 intervals of ~ 0.1 dex width, the only substantial change is that the SMC curve is raised by ~ 0.1 dex, for ages below 500 Myr. The two SMC clusters with extremely low metallicities $[Fe/H] < -2$ dex – are NGC294 and HW85; their abundances were already analyzed in Sect. 5.1. Having such small metallicity values means that their associated uncertainty will be quite large, as discussed in Sect. 4. This has the effect of spreading their positions in the density map, preventing these low values from affecting the AMR substantially. If these two OCs are excluded from our data, the resulting AMR for the SMC moves upwards in the $[Fe/H]$ axis by less than 0.02 dex.

Several chemical evolution models and empirically estimated AMRs can be found in the literature for both Magellanic Clouds. Many of the studies performed on the age-metallicity relation of the S/LMC present their results as scattered points in the age vs metallicity plot, rather than fitting a unique AMR function to describe the distribution of those observed values. To allow a straightforward comparison with our AMR functions, we show in Fig. 14 – center and bottom plots – the functions presented in twelve other works. These studies constitute a representative sample of the different methods and data used in the literature over the past twenty years, for these two galaxies: Pagel & Tautvaisiene (1998, PT98; bursting models), Geha et al. (1998, G98; closed-box model with Holtzman SFH), Harris & Zaritsky (2004, HZ04), Carrera et al. (2008b, C08a; average of four disk frames), Carrera et al. (2008a, C08b; average of thirteen frames), Harris & Zaritsky (2009, HZ09), Noël et al. (2009, N09; 5th degree polynomial fit to the AMRs of their three observed regions), Tsujimoto & Bekki (2009, TB09; 1: no merger model, 2: equal mass merger, 3: one to four merger), Rubele et al. (2012, R12; four tiles average), Cignoni et al. (2013, C13; B: Bologna, C: Cole), Piatti & Geisler (2013, PG13), and Meschin et al. (2014, M14; 0: field LMC0, 1: field LMC1, 2: field LMC2). Details on how these AMRs were constructed will not be given here, as they can be consulted in each reference. All of the above mentioned articles used field stars for the obtention of their AMRs. This is, as far as we are aware, the first work where the AMR function for both galaxies is derived entirely from observed star clusters.

The overall trend of both AMRs coincides with what has already been found in the literature, namely that the metallicity increases rather steadily with younger ages. On average, our AMR estimates are displaced slightly towards more metal rich values, particularly in the case of the SMC. This tendency was already mentioned in Sect. 5.1, where possible causes for at least some part of the effect were also given.

For the LMC galaxy, Fig. 14 center plot, we see a marked drop in metallicity from ~ -0.3 dex beginning around 3.8 Gyr, and ending 3 Gyrs ago at ~ -0.55 dex. The former high $[Fe/H]$ value is not found in any of the remaining functions for the LMC. The M14-0 curve seems to reproduce this behavior, but shifted ~ 0.8 Gyr towards younger ages, and with a less pronounced peak that reaches its maximum of ~ -0.45 dex at ~ 3.2 Gyr. The high metallicity value in the LMC AMR at 3.8 Gyr, is caused by the four OCs located around ~ 3.3 Gyr with $[Fe/H] \approx -0.25$ dex; when they are excluded, the peak disappears. These four OCs are: SL33, H3, SL5, and KMHK586, their CMDs are shown in Appendix E, Fig E.2. The last three of these OCs are analyzed in Piatti (2011b) and have no metallicities or extinction values assigned, as only ages were estimated in this article via the δT_1 index. Ages obtained by AStECA for this group of OCs are between 0.1-0.3 dex larger than the ones given in Piatti (2011b). According to this article, the oldest OCs in the group have ages of ~ 2.5 Gyr. This means that if literature's ages were used instead of the ones produced by the code, the peak would not show. In fact, the entire AMRs functions derived using literature values – i.e., those taken from the articles in Table 1 – are markedly different from the ones shown in Fig. 14. This is expected as most OCs in these works are assigned fixed metallicities of -0.7 dex and -0.4 dex for the S/LMC, respectively; particularly for estimated ages below 1 Gyr. Literature AMRs for both MCs, obtained following the same method explained in this section, can be seen in Appendix E, Fig E.1.

After the aforementioned drop in the LMC's AMR, there is a steep climb from 3 Gyr to 2 Gyr reaching almost $[Fe/H] \sim -0.25$ dex, and then a sustained but much more shallow increase up to

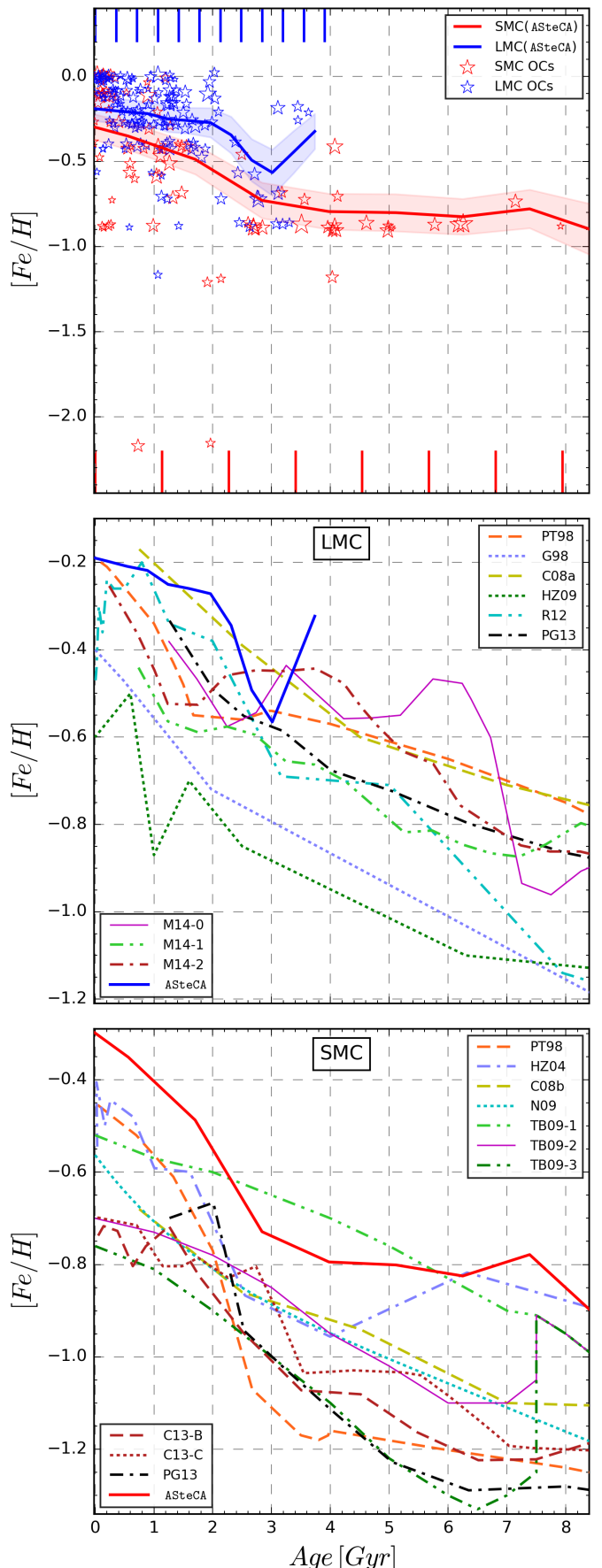


Fig. 14. AStECA's age-metallicity relation for the S/LMC (red/blue solid lines). Shaded areas are the 1σ regions for each AMR. Blue and red stars are the LMC and SMC clusters in our set. See text in Sect. 6.1 for more details.

1370 the present day's metal content of ~ -0.2 dex. The AMR functions
 1371 for the LMC that differ the most from the one obtained
 1372 with AStECA values, are those taken from HZ09 and G98. These
 1373 two curves are visibly separated, not only from our AMR, but
 1374 also from the rest of the group. Our average metallicity value
 1375 for present day OCs, coincides reasonably well with those from
 1376 PT98, C08a, and M14-2. The PT98 bursting model and field 2
 1377 from M14, show nonetheless a very different rate of increase
 1378 from 2 Gyr to present times, compared to AStECA's AMR. The
 1379 average AMR from C08a, while lacking finer details, provides a
 1380 better match for this age range.

1381 The AMR function for the SMC obtained using AStECA's
 1382 age and metallicity values, is shown along ten AMRs taken from
 1383 the published literature in Fig. 14, bottom. Our AMR shows an
 1384 increased rate of [Fe/H] that reaches a peak around ~ 7.5 Gyr ago,
 1385 followed by a marked dip between 6–7 Gyr. This feature
 1386 was reported by TB09 in its two merger models. The TB09-2
 1387 model (equal mass merger) appears to best mimic our AMR for
 1388 the SMC, although ours is shifted upwards towards higher abund-
 1389 ances. The TB09-3 model (1:4 mass merger) shows the same
 1390 peak, but followed by a much more pronounced dip that goes
 1391 well below most AMRs, including our own. The TB09-2 model
 1392 and our AMR follow a very similar path up to 3 Gyr, where they
 1393 start to deviate. For present day ages, where the AMRs differ
 1394 the most, our curve is more metal rich by about 0.4 dex com-
 1395 pared to the TB09-2 model. Following the dip beyond ~ 6 Gyr,
 1396 abundances in our AMR plateau around a value of $[Fe/H] \approx -0.8$
 1397 dex until approximately 3 Gyr ago, where the rate of growth for
 1398 the metallicity increases considerably. From that point up to the
 1399 present day, the average metallicity for OCs in the SMC grows
 1400 by about 0.4 dex, according to the AStECA AMR. The increased
 1401 rate of growth behavior for ages younger than 3 Gyr, is only
 1402 reproduced by the PT8 model, and the HZ04 function. In both
 1403 cases, the maximum [Fe/H] value attained by these AMRs for
 1404 the youngest ages is lower by ~ 0.12 dex, compared to our own
 1405 estimate for this galaxy.

1406 The canonical metallicity values usually accepted –
 1407 $[Fe/H] = -0.7$ dex, $[Fe/H] = -0.4$ dex, for the S/LMC – are
 1408 shown to be off by ~ 0.3 dex on average, for clusters younger
 1409 than 2.5 Gyr in both galaxies. We must keep in mind though,
 1410 that most of the [Fe/H] values in the previous literature are ob-
 1411 tained using a solar metallicity of $z_{\odot} = 0.019$. Instead in this work
 1412 we used the more recent value of $z_{\odot} = 0.0152$. As was shown in
 1413 Sect. 5.1, this difference alone means our [Fe/H] estimates will
 1414 be ~ 0.1 dex above the others.

1415 Overall our AMRs can not be explained by any single model
 1416 or empirical AMR function, and are best reproduced by a com-
 1417 bination of several of these. A similar result was found in Piatti
 1418 & Geisler (2013), although their AMRs – derived from field star
 1419 population – are significantly different from ours, mainly for the
 1420 SMC case. It is important to remember that the AMRs estimated
 1421 using the ages and metallicities derived via AStECA, are aver-
 1422 aged over the structure of both Magellanic Clouds. In Fig. 1 we
 1423 showed that our set of OCs covers a large portion of the surface
 1424 of these galaxies. If more OCs were available so that the AMRs
 1425 could be instead estimated by sectors in the S/LMC, it is entirely
 1426 possible that different results would arise. When clusters in our
 1427 set are divided by sectors, statistically low numbers are assigned
 1428 to each – particularly for the SMC – which makes this more de-
 1429 tailed study not feasible.

7. Summary and conclusions

1430

We presented an homogeneous catalog for a set of 239 star 1431 clusters in the Large and Small Magellanic Clouds, observed 1432 with the Washington photometric system. The OCs span a wide 1433 range in metallicity, age, and mass, and are spatially distributed 1434 throughout both galaxies. The fundamental parameters metallic- 1435 ity, age, reddening, distance modulus, and total mass were de- 1436 termined using the AStECA package. This tool allows the auto- 1437 mated processing of an OC's positional and photometric data, 1438 resulting in estimates of both its structural and intrinsic/extrinsic 1439 properties. As already shown in Paper I, the advantages of using 1440 this package include reproducible and objective results, along 1441 with a proper handling of the uncertainties involved in the syn- 1442 thetic cluster matching process. This permits the generation of a 1443 truly homogeneous catalog of observed clusters, with their most 1444 important parameters fully recovered. Our resulting catalog is 1445 complete for all the analyzed parameters, including metallicity 1446 and mass, two properties often assumed or not obtained at all. 1447

The analysis of our results, demonstrate that the assigned val- 1448 ues for the OCs are in good agreement with published literature 1449 which used the same Washington photometry. The metallicity 1450 parameter showed to be the most discrepant one, with AStECA's 1451 [Fe/H] values – for both galaxies combined – being on aver- 1452 age ~ 0.22 dex larger than those present in the literature. Half 1453 of this difference is due to the solar abundance assumed in this 1454 work ($z_{\odot} = 0.0152$; Bressan et al. 2012). The explanation for the 1455 remaining ~ 0.1 dex is largely the confirmation bias effect, by 1456 which most OC studies will assume the canonical [Fe/H] values 1457 rather than derive them through statistically valid means. We also 1458 compared our results with those taken from articles that used 1459 different photometric systems. While the age differences in this 1460 case are somewhat larger, they can be mostly explained by ef- 1461 fects outside the code. Internal errors show no biases present in 1462 our determination of fundamental parameters. 1463

We performed a detailed comparative study of masses ob- 1464 tained through integrated photometry studies, with our own esti- 1465 mates from CMD analysis. The total mass values from the latter 1466 studies are shown to be systematically overestimated. This re- 1467 sult is opposite to the expectation that larger clusters can have 1468 their masses recovered with moderate accuracy, via integrated 1469 photometry. 1470

A method for deriving the distribution of any fundamental 1471 parameter – or a combination of two of them – is presented. 1472 This method takes into account the information contained by the 1473 uncertainties, often excluded from the analysis. By relying on 1474 Gaussian kernels, it is robust and independent of ad-hoc bin- 1475 ning choices. An age-metallicity relation is derived using the 1476 above mentioned method and the parameter values obtained by 1477 AStECA, for both galaxies. The AMRs generated can not be fully 1478 matched by any model or empirical determination found in the 1479 recent literature. 1480

We demonstrated that the AStECA package is able to pro- 1481 duce proper estimations of observed star clusters, with their fun- 1482 damental parameters covering a wide range of values. A neces- 1483 sary statistically valid error analysis can be performed, thanks to 1484 its built-in bootstrap error assignment method. The tool is also 1485 proven to be capable of operating almost entirely unassisted, on 1486 large databases of clusters. This is an increasingly essential fea- 1487 ture of any astrophysical analysis tool, given the growing impor- 1488 tance of big data and the necessity to conduct research on large 1489 astronomical data sets. 1490

Acknowledgements. GIP would like to thank the help and assistance provided 1491 throughout the redaction of several portions of this work by: D. Hunter, A. E. 1492

Dolphin, M. Rafelski, D. Zaritsky, T. Palma, F. F. S. Maia, B. Popescu, and H. Baumgardt. This research has made use of the VizieR³¹ catalogue access tool, operated at CDS, Strasbourg, France (Ochsenbein et al. 2000). This research has made use of “Aladin sky atlas”³² developed at CDS, Strasbourg Observatory, France (Bonnarel et al. 2000; Boch & Fernique 2014). This research has made use of NASA’s Astrophysics Data System³³. This research made use of the Python language v2.7³⁴ (van Rossum 1995), and the following packages: NumPy³⁵ (Van Der Walt et al. 2011); SciPy³⁶ (Jones et al. 2001); Astropy³⁷, a community-developed core Python package for Astronomy (Astropy Collaboration et al. 2013); scikit-learn³⁸ (Pedregosa et al. 2011); matplotlib³⁹ (Hunter et al. 2007). This research made use of the Tool for OPerations on Catalogues And Tables (TOPCAT)⁴⁰ (Taylor 2005).

References

- Anders, P. & Fritze-v. Alvensleben, U. 2003, A&A, 401, 1063
 Anders, P., Kotulla, R., De Grij, R., & Wicker, J. 2013, The Astrophysical Journal, 778, 138
 Andrae, R. 2010, ArXiv e-prints [arXiv:1009.2755]
 Astropy Collaboration, Robitaille, T. P., Tollerud, E. J., et al. 2013, A&A, 558, A33
 Balbinot, E., Santiago, B. X., Kerber, L. O., Barbuy, B., & Dias, B. M. S. 2010, MNRAS, 404, 1625
 Baumgardt, H., Parmentier, G., Anders, P., & Grebel, E. K. 2013, MNRAS, 430, 676
 Bertelli, G., Bressan, A., Chiosi, C., Fagotto, F., & Nasi, E. 1994, A&AS, 106
 Bevington, P. R. & Robinson, D. K. 2003, McGraw-Hill
 Bica, E., Bonatto, C., Dutra, C. M., & Santos, J. F. C. 2008, Monthly Notices of the Royal Astronomical Society, 389, 678
 Bica, E. L. D. & Schmitt, H. R. 1995, ApJS, 101, 41
 Bland, J. M. & Altman, D. G. 1986, Lancet, 1, 307
 Boch, T. & Fernique, P. 2014, in Astronomical Society of the Pacific Conference Series, Vol. 485, Astronomical Data Analysis Software and Systems XXIII, ed. N. Manset & P. Forshay, 277
 Bonatto, C. & Bica, E. 2007, MNRAS, 377, 1301
 Bonnarel, F., Fernique, P., Bienaymé, O., et al. 2000, AAPPS, 143, 33
 Bressan, A., Marigo, P., Girardi, L., et al. 2012, MNRAS, 427, 127
 Canterna, R. 1976, The Astronomical Journal, 81, 228
 Carrera, R., Gallart, C., Aparicio, A., et al. 2008a, The Astronomical Journal, 136, 1039
 Carrera, R., Gallart, C., Hardy, E., Aparicio, A., & Zinn, R. 2008b, The Astronomical Journal, 135, 836
 Chabrier, G. 2001, ApJ, 554, 1274
 Chiosi, E., Vallenari, A., Held, E. V., Rizzi, L., & Moretti, A. 2006, Astronomy and Astrophysics, 452, 179
 Choudhury, S., Subramaniam, A., & Piatti, A. E. 2015, The Astronomical Journal, 149, 52
 Cignoni, M., Cole, A. A., Tosi, M., et al. 2013, ApJ, 775, 83
 de Grij, R. & Anders, P. 2006, MNRAS, 366, 295
 de Grij, R. & Bono, G. 2015, The Astronomical Journal, 149, 179
 de Grij, R., Wicker, J. E., & Bono, G. 2014, The Astronomical Journal, 147, 122
 Dias, B., Coelho, P., Barbuy, B., Kerber, L., & Idiart, T. 2010, A&A, 520, A85
 Dias, W. S., Alessi, B. S., Moitinho, A., & Lépine, J. R. D. 2002, A&A, 389, 871
 Dolphin, A. E. 2002, Monthly Notices of the Royal Astronomical Society, 332, 91
 Dubath, P., Meylan, G., Mayor, M., & Magain, P. 1990, A&A, 239, 142
 Elson, R. A. W., Sigurdsson, S., Davies, M., Hurley, J., & Gilmore, G. 1998, MNRAS, 300, 857
 Geha, M. C., Holtzman, J. A., Mould, J. R., et al. 1998, The Astronomical Journal, 115, 1045
 Geisler, D. 1996, AJ, 111, 480
 Geisler, D., Bica, E., Dottori, H., et al. 1997, AJ, 114, 1920
 Geisler, D., Piatti, A. E., Bica, E., & Claria, J. J. 2003, Monthly Notices of the Royal Astronomical Society, 341, 771
- 31 <http://vizier.u-strasbg.fr/viz-bin/VizieR>
 32 <http://aladin.u-strasbg.fr/>
 33 <http://www.adsabs.harvard.edu/>
 34 <http://www.python.org/>
 35 <http://www.numpy.org/>
 36 <http://www.scipy.org/>
 37 <http://www.astropy.org/>
 38 <http://scikit-learn.org/>
 39 <http://matplotlib.org/>
 40 <http://www.starlink.ac.uk/topcat/>
- Geisler, D. & Sarajedini, A. 1999, The Astronomical Journal, 117, 308
 Girardi, L., Bertelli, G., Bressan, A., et al. 2002, A&A, 391, 195
 Girardi, L., Eggenberger, P., & Miglio, A. 2011, MNRAS, 412, L103
 Girardi, L., Groenewegen, M. A. T., Weiss, A., & Salaris, M. 1998, MNRAS, 301, 149
 Girardi, L., Rubele, S., & Kerber, L. 2009, MNRAS, 394, L74
 Glatt, K., Grebel, E. K., & Koch, A. 2010, Astronomy and Astrophysics, 517, A50
 Glatt, K., Grebel, E. K., Sabbi, E., et al. 2008, The Astronomical Journal, 136, 1703
 Grocholski, A. J. & Sarajedini, A. 2003, MNRAS, 345, 1015
 Harris, J. & Zaritsky, D. 2004, AJ, 127, 1531
 Harris, J. & Zaritsky, D. 2009, The Astronomical Journal, 138, 1243
 Haschke, R., Grebel, E. K., & Duffau, S. 2011, The Astronomical Journal, 141, 158
 Hills, S., von Hippel, T., Courteau, S., & Geller, A. M. 2015, The Astronomical Journal, 149, 94
 Hunter, D. A., Elmegreen, B. G., Dupuy, T. J., & Mortonson, M. 2003, Astron J, 126, 1836
 Hunter, J. D. et al. 2007, Computing in science and engineering, 9, 90
 Jones, E., Oliphant, T., Peterson, P., et al. 2001, SciPy: Open source scientific tools for Python, [Online; accessed 2016-06-21]
 Kharchenko, N. V., Piskunov, A. E., Röser, S., Schilbach, E., & Scholz, R.-D. 2005, A&A, 440, 403
 Knuth, K. H. 2006, ArXiv Physics e-prints [physics/0605197]
 Krouwer, J. S. 2008, Stat Med, 27, 778
 Leitherer, C., Schaerer, D., Goldader, J. D., et al. 1999, ApJS, 123, 3
 Lejeune, T. & Schaerer, D. 2001, A&A, 366, 538
 Li, C., Grijs Richard, d., Bastian, N., et al. 2016, ArXiv e-prints [arXiv:1606.05394]
 Maia, F. F. S., Corradi, W. J. B., & Santos, Jr., J. F. C. 2010, MNRAS, 407, 1875
 Maia, F. F. S., Piatti, A. E., & Santos, J. F. C. 2013, Monthly Notices of the Royal Astronomical Society, 437, 2005
 Marigo, P., Girardi, L., Bressan, A., et al. 2008, A&A, 482, 883
 Mateo, M. & Hodge, P. 1986, ApJS, 60, 893
 Meschin, I., Gallart, C., Aparicio, A., et al. 2014, MNRAS, 438, 1067
 Milone, A. P., Bedin, L. R., Piotto, G., & Anderson, J. 2009, A&A, 497, 755
 Milone, A. P., Marino, A. F., D’Antona, F., et al. 2016, MNRAS, 458, 4368
 Naylor, T. & Jeffries, R. D. 2006, MNRAS, 373, 1251
 Netopil, M., Paunzen, E., & Carraro, G. 2015, Astronomy & Astrophysics
 Noël, N. E. D., Aparicio, A., Gallart, C., et al. 2009, ApJ, 705, 1260
 Ochsenbein, F., Bauer, P., & Marcout, J. 2000, A&AS, 143, 23
 Pagel, B. E. J. & Tautvaisiene, G. 1998, MNRAS, 299, 535
 Palma, T., Clariá, J. J., Geisler, D., Piatti, A. E., & Ahumada, A. V. 2013, Astronomy & Astrophysics, 555, A131
 Palma, T., Gramajo, L. V., Clariá, J. J., et al. 2015, ArXiv e-prints [arXiv:1511.05451]
 Paunzen, E. & Netopil, M. 2006, MNRAS, 371, 1641
 Pedregosa, F., Varoquaux, G., Gramfort, A., et al. 2011, Journal of Machine Learning Research, 12, 2825
 Perren, G. I., Vázquez, R. A., & Piatti, A. E. 2015, Astronomy & Astrophysics, 576, A6
 Phelps, R. L., Janes, K. A., & Montgomery, K. A. 1994, AJ, 107, 1079
 Piatti, A. E. 2010, Astronomy and Astrophysics, 513, L13
 Piatti, A. E. 2011a, Monthly Notices of the Royal Astronomical Society: Letters, 416, L89
 Piatti, A. E. 2011b, Monthly Notices of the Royal Astronomical Society: Letters, 418, L40
 Piatti, A. E. 2011c, Monthly Notices of the Royal Astronomical Society: Letters, 418, L69
 Piatti, A. E. 2012, Astronomy & Astrophysics, 540, A58
 Piatti, A. E. 2013, Monthly Notices of the Royal Astronomical Society, 437, 1646
 Piatti, A. E. 2014, MNRAS, 445, 2302
 Piatti, A. E. & Bastian, N. 2016, ArXiv e-prints [arXiv:1603.06891]
 Piatti, A. E. & Bica, E. 2012, Monthly Notices of the Royal Astronomical Society, 425, 3085
 Piatti, A. E., Bica, E., Geisler, D., & Claria, J. J. 2003a, Monthly Notices RAS, 344, 965
 Piatti, A. E., Clariá, J. J., Bica, E., et al. 2011a, Monthly Notices of the Royal Astronomical Society, 417, 1559
 Piatti, A. E., Clariá, J. J., Parisi, M. C., & Ahumada, A. V. 2011b, Publications of the Astronomical Society of the Pacific, 123, 519
 Piatti, A. E., de Grij, R., Ripepi, V., et al. 2015a, MNRAS, 454, 839
 Piatti, A. E., de Grij, R., Rubele, S., et al. 2015b, MNRAS, 450, 552
 Piatti, A. E. & Geisler, D. 2013, The Astronomical Journal, 145, 17
 Piatti, A. E., Geisler, D., Bica, E., & Claria, J. J. 2003b, Monthly Notices of the Royal Astronomical Society, 343, 851
 Piatti, A. E., Geisler, D., Sarajedini, A., & Gallart, C. 2009, Astronomy and Astrophysics, 501, 585

- 1636 Piatti, A. E., Geisler, D., Sarajedini, A., Gallart, C., & Wischnjewsky, M. 2008,
 1637 Monthly Notices of the Royal Astronomical Society, 389, 429
 1638 Piatti, A. E., Sarajedini, A., Geisler, D., Clark, D., & Seguel, J. 2007a, Monthly
 1639 Notices of the Royal Astronomical Society, 377, 300
 1640 Piatti, A. E., Sarajedini, A., Geisler, D., Gallart, C., & Wischnjewsky, M. 2007b,
 1641 Monthly Notices of the Royal Astronomical Society, 382, 1203
 1642 Piatti, A. E., Sarajedini, A., Geisler, D., Gallart, C., & Wischnjewsky, M. 2007c,
 1643 Monthly Notices of the Royal Astronomical Society: Letters, 381, L84
 1644 Piatti, A. E., Sarajedini, A., Geisler, D., Seguel, J., & Clark, D. 2005, Monthly
 1645 Notices of the Royal Astronomical Society, 358, 1215
 1646 Pietrzynski, G. & Udalski, A. 1999, AcA, 49, 157
 1647 Pietrzynski, G. & Udalski, A. 2000, AcA, 50, 337
 1648 Popescu, B. & Hanson, M. M. 2010a, ApJ, 724, 296
 1649 Popescu, B. & Hanson, M. M. 2010b, ApJ, 713, L21
 1650 Popescu, B., Hanson, M. M., & Elmegreen, B. G. 2012, ApJ, 751, 122
 1651 Rafelski, M. & Zaritsky, D. 2005, Astron J, 129, 2701
 1652 Rubele, S., Girardi, L., Kozhurina-Platais, V., Goudfrooij, P., & Kerber, L. 2011,
 1653 MNRAS, 414, 2204
 1654 Rubele, S., Kerber, L., & Girardi, L. 2010, MNRAS, 403, 1156
 1655 Rubele, S., Kerber, L., Girardi, L., et al. 2012, A&A, 537, A106
 1656 Scargle, J. D., Norris, J. P., Jackson, B., & Chiang, J. 2013, ApJ, 764, 167
 1657 Schmeja, S., Kharchenko, N. V., Piskunov, A. E., et al. 2014, A&A, 568, A51
 1658 Scott, D. W. 1979, Biometrika, 66, 605
 1659 Silverman, B. 1986, Density Estimation for Statistics and Data Analysis, Chap-
 1660 man & Hall/CRC Monographs on Statistics & Applied Probability (Taylor &
 1661 Francis)
 1662 Simonoff, J. S. & Udina, F. 1997, Computational Statistics & Data Analysis, 23,
 1663 335
 1664 Sollima, A., Carballo-Bello, J. A., Beccari, G., et al. 2010, MNRAS, 401, 577
 1665 Subramanian, S. & Subramaniam, A. 2009, A&A, 496, 399
 1666 Tammann, G. A., Sandage, A., & Reindl, B. 2003, A&A, 404, 423
 1667 Taylor, M. B. 2005, in Astronomical Society of the Pacific Conference Se-
 1668 ries, Vol. 347, Astronomical Data Analysis Software and Systems XIV, ed.
 1669 P. Shopbell, M. Britton, & R. Ebert, 29
 1670 Tsujimoto, T. & Bekki, K. 2009, The Astrophysical Journal Letters, 700, L69
 1671 Udalski, A., Soszynski, I., Szymanski, M., et al. 1999, Acta Astron., 49, 223
 1672 Van Der Walt, S., Colbert, S. C., & Varoquaux, G. 2011, Computing in Science
 1673 & Engineering, 13, 22
 1674 van Rossum, G. 1995, Python tutorial, Report CS-R9526, pub-CWI, pub-
 1675 CWI:adr
 1676 Vanderplas, J., Connolly, A., Ivezić, Ž., & Gray, A. 2012, in Conference on In-
 1677 telligent Data Understanding (CIDU), 47–54
 1678 von Hippel, T. 2005, ApJ, 622, 565
 1679 von Hippel, T., van Dyk, D. A., Stenning, D. C., et al. 2014, in EAS Publications
 1680 Series, Vol. 65, EAS Publications Series, 267–287

1681 Appendix A: Color-magnitude diagrams for outliers

1682 We present CMDs for the ten OCs referred to as “outliers”, given
 1683 their $\log(\text{age}/\text{yr}) > 0.5$ differences between ASt_eCA and literature
 1684 values. In Fig. A.1 the CMDs for these OCs are plotted in pairs,
 1685 two OCs per row.

1686 The left CMD in each pair shows the cluster region with the
 1687 literature isochrone fit shown in red. For nine of the OCs we
 1688 fit Marigo et al. (2008) isochrones, since this set of theoretical
 1689 isochrones were used in all but one of the articles where these
 1690 OCs were analyzed. The exception is SMC-L35 which was fit
 1691 using Girardi et al. (2002) isochrones, so the same set is used for
 1692 this OC. The right CMD shows the same cluster region with the
 1693 isochrone that generated the best match SC found by ASt_eCA,
 1694 shown in green. The colors of the stars in this CMD correspond
 1695 to the MPs assigned by the DA, when applied. Semi-transparent
 1696 stars are those removed by the cell-by-cell density based clean-
 1697 ing algorithm (see Sect.3.3), also when applied. Values for the
 1698 fundamental parameters in both fits are shown to the bottom left
 1699 of each CMD.

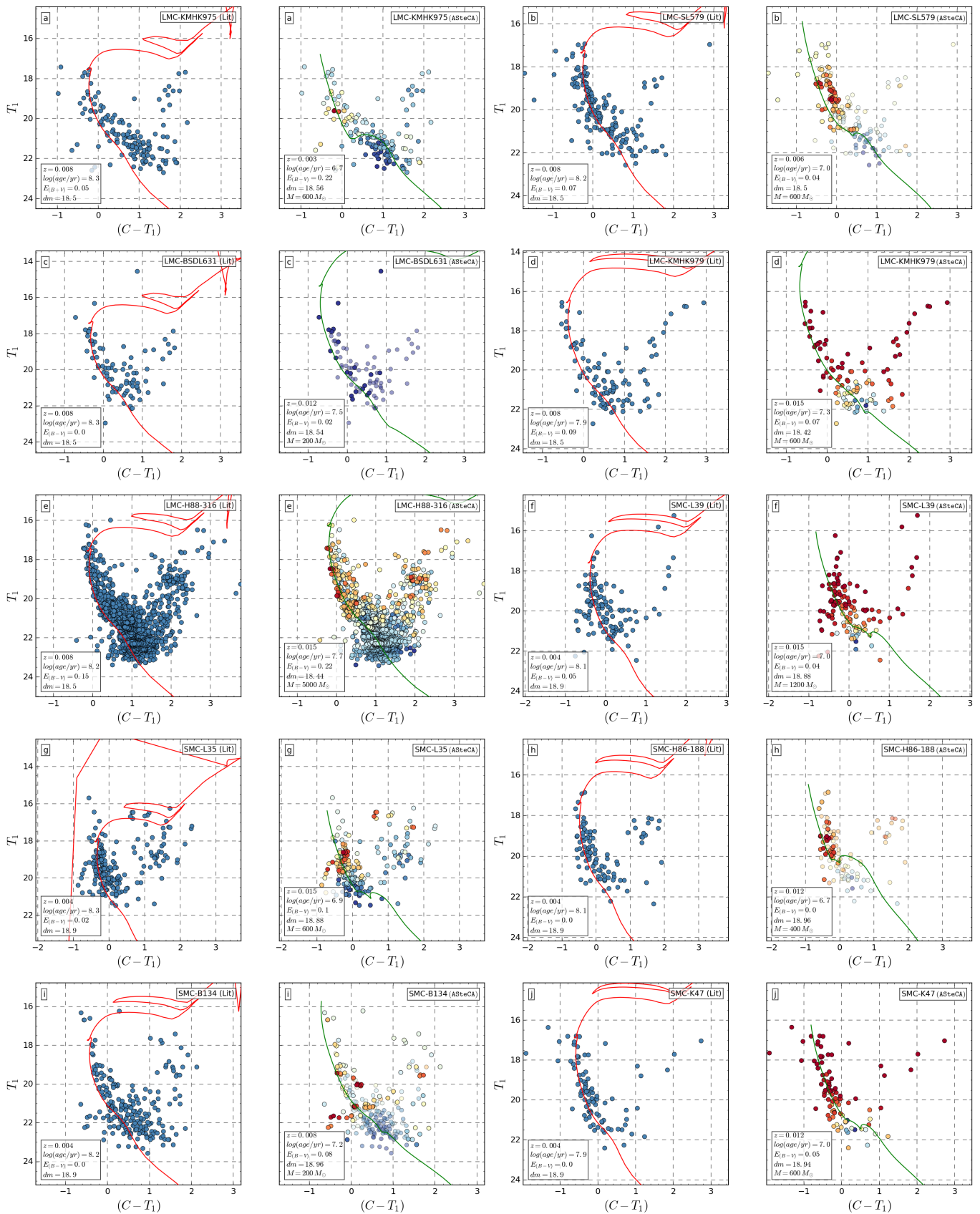
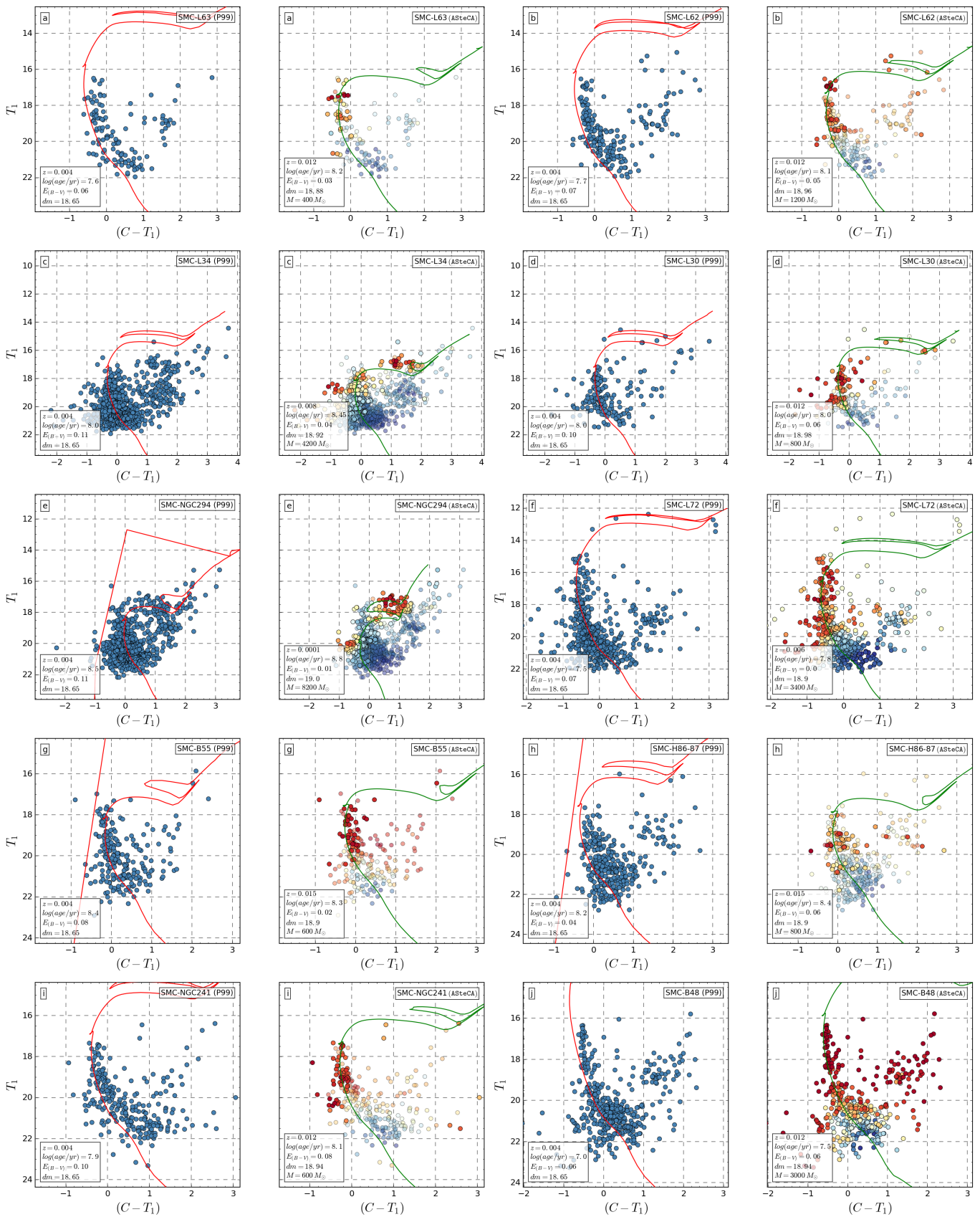


Fig. A.1. CMDs for the outliers set. See description of the plots in Appendix A.

1700 **Appendix B: Color-magnitude diagrams for the P99,**
1701 **P00, C06, and G10 databases**

1702 This appendix presents the CMDs of all OCs cross-matched with
1703 our own sample, in the databases P99, P00, C06, and G10, i.e.:
1704 those that used the isochrone fit method in their analysis.

1705 Each CMD pair in the figures below shows a given OC with
1706 the fit proposed by the corresponding database to the left (red
1707 isochrone), and the one estimated by AStECA to the right (green
1708 isochrone). The coloring of the stars in the CMD to the right,
1709 correspond to the weights assigned by the decontamination algo-
1710 rithm. Stars drawn semi-transparent were discarded by the cell-
1711 by-cell cleaning method, and thus not used in the synthetic match
1712 process.

**Fig. B.1.** CMDs for the P99 database.

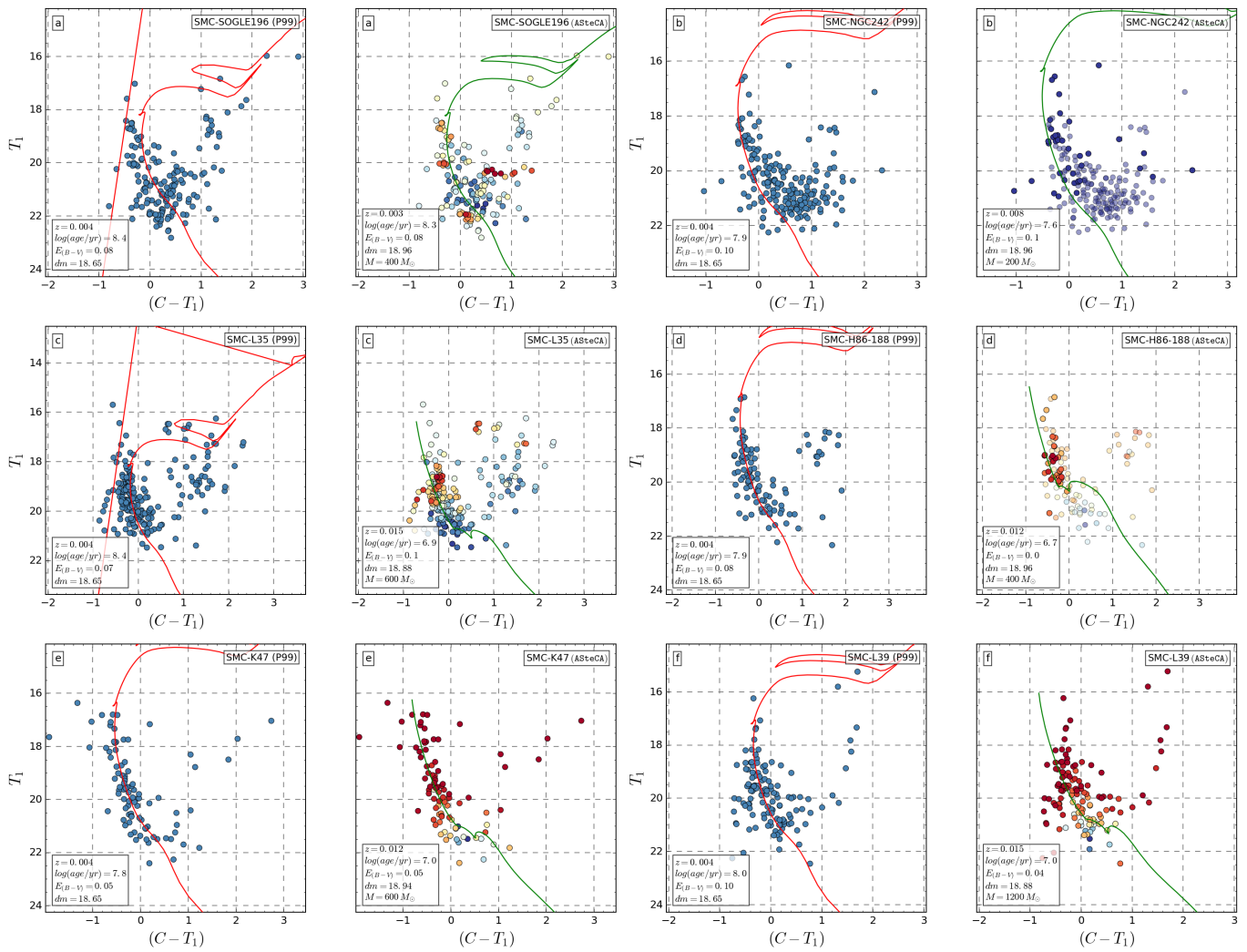
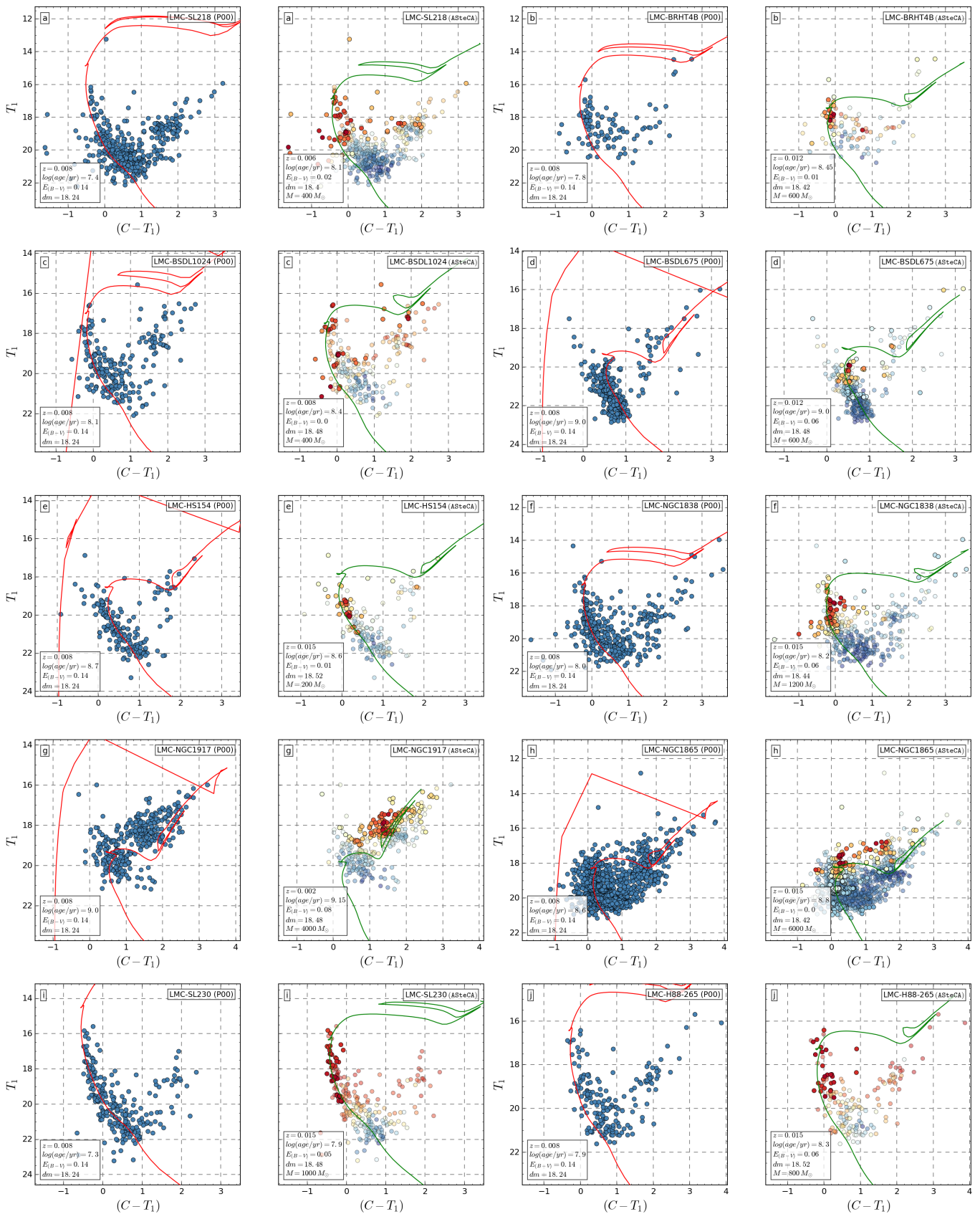
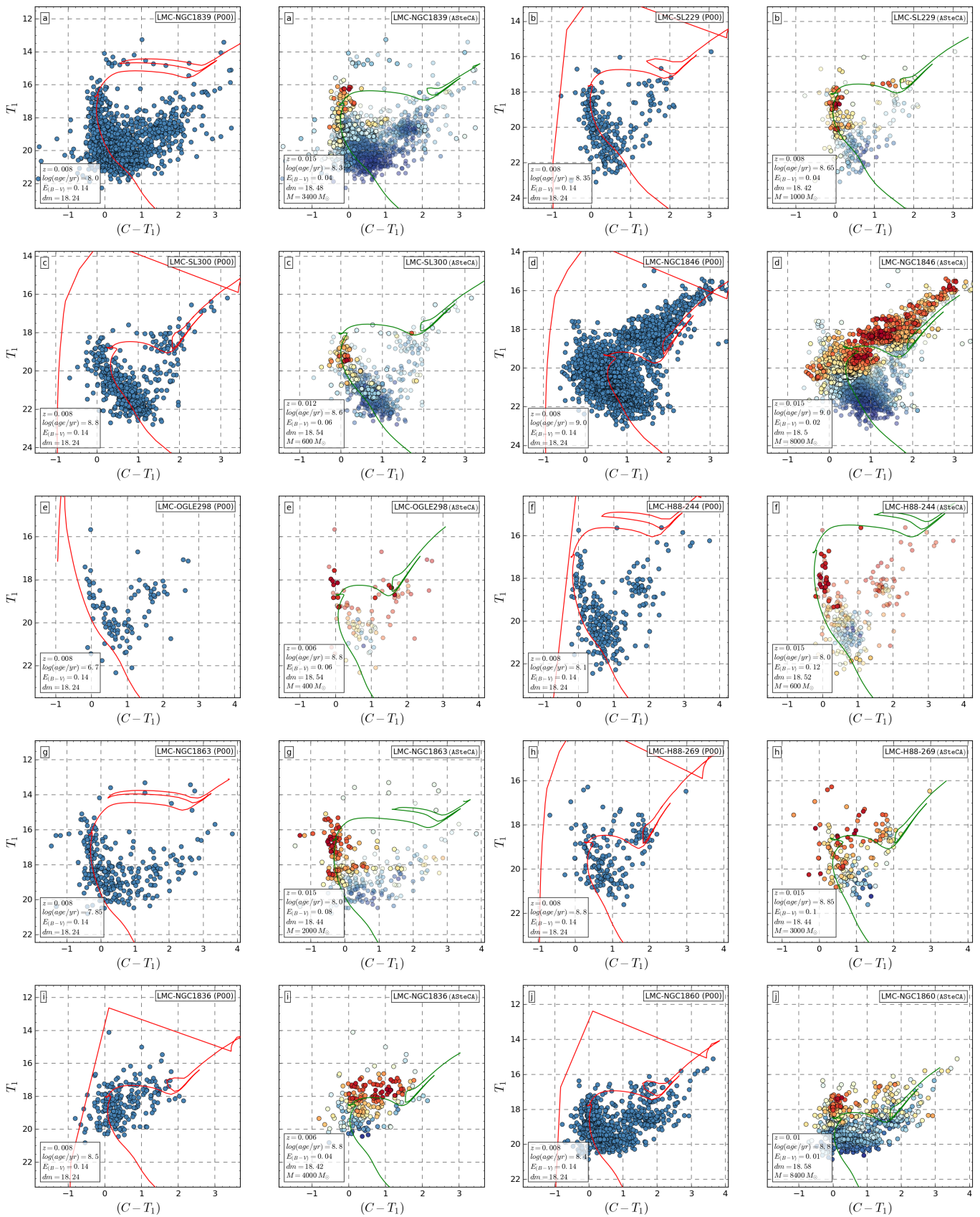
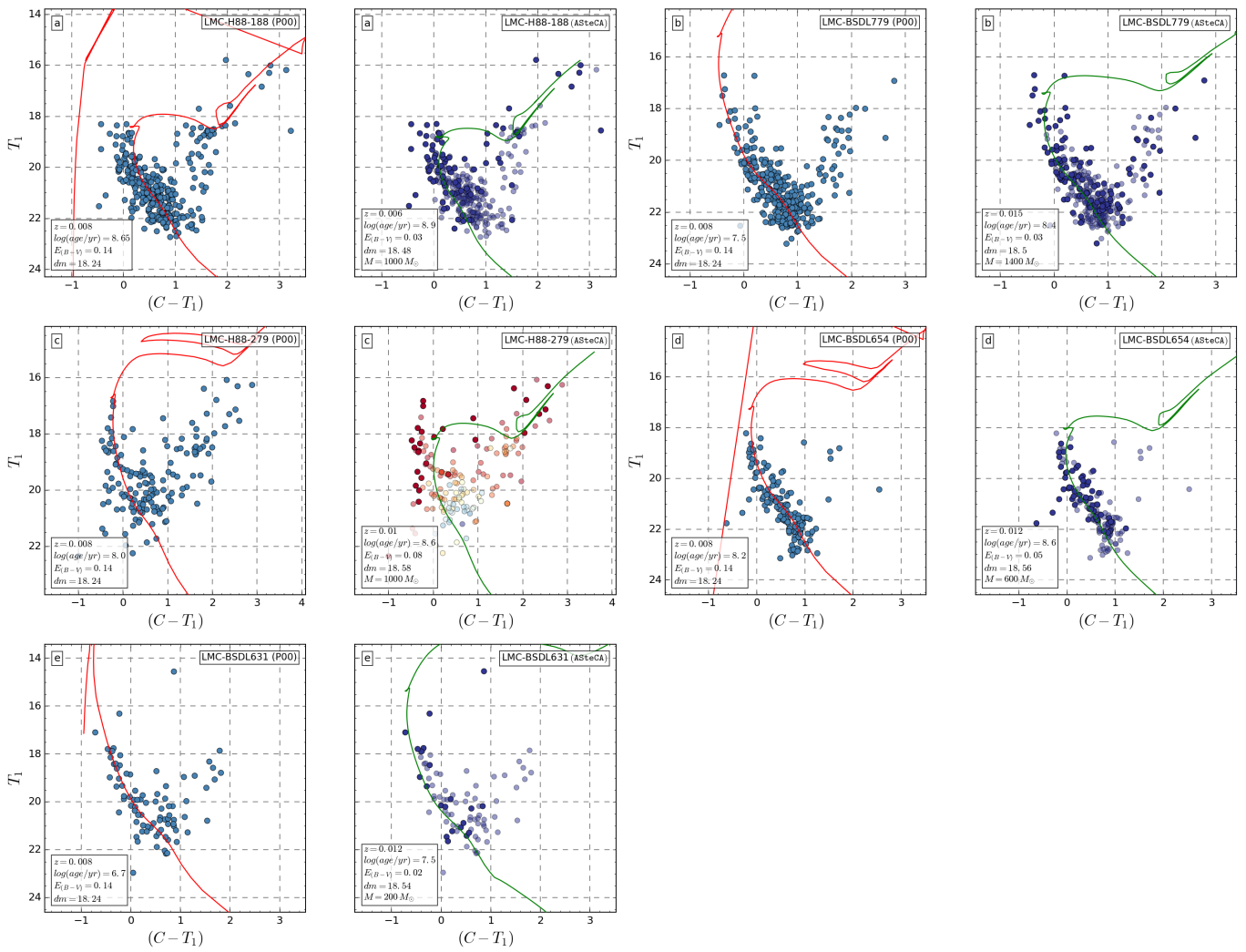
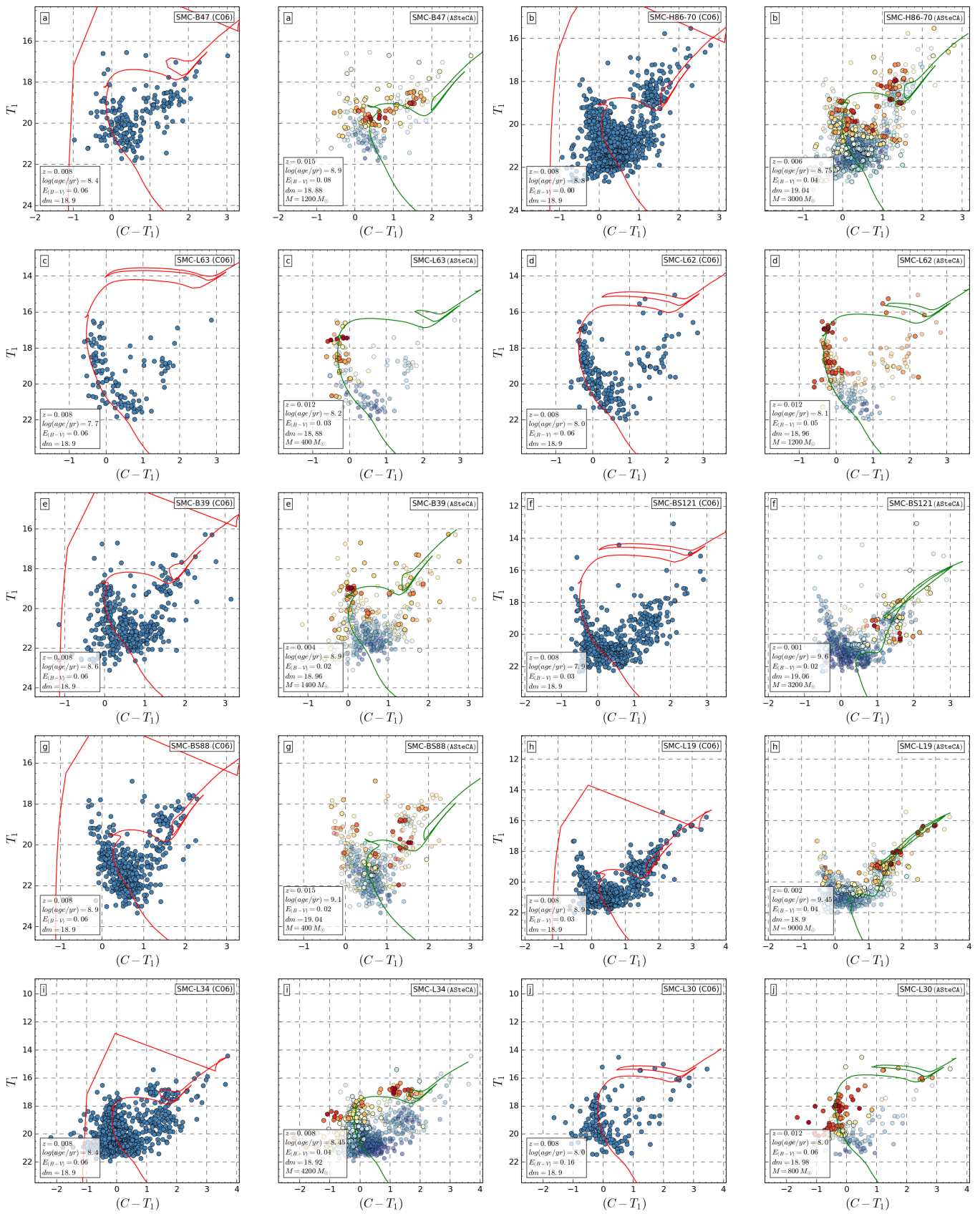


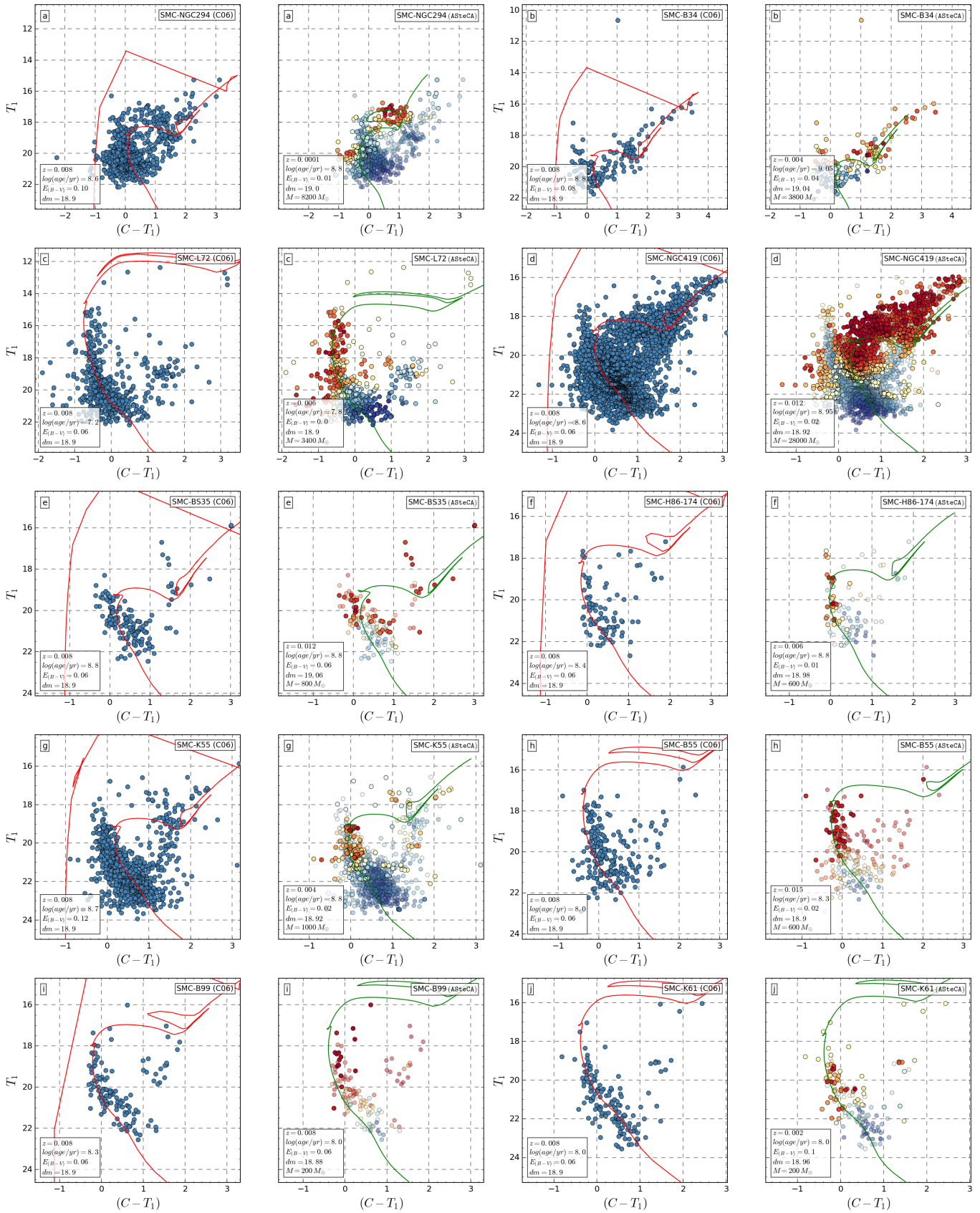
Fig. B.2. CMDs for the P99 database.

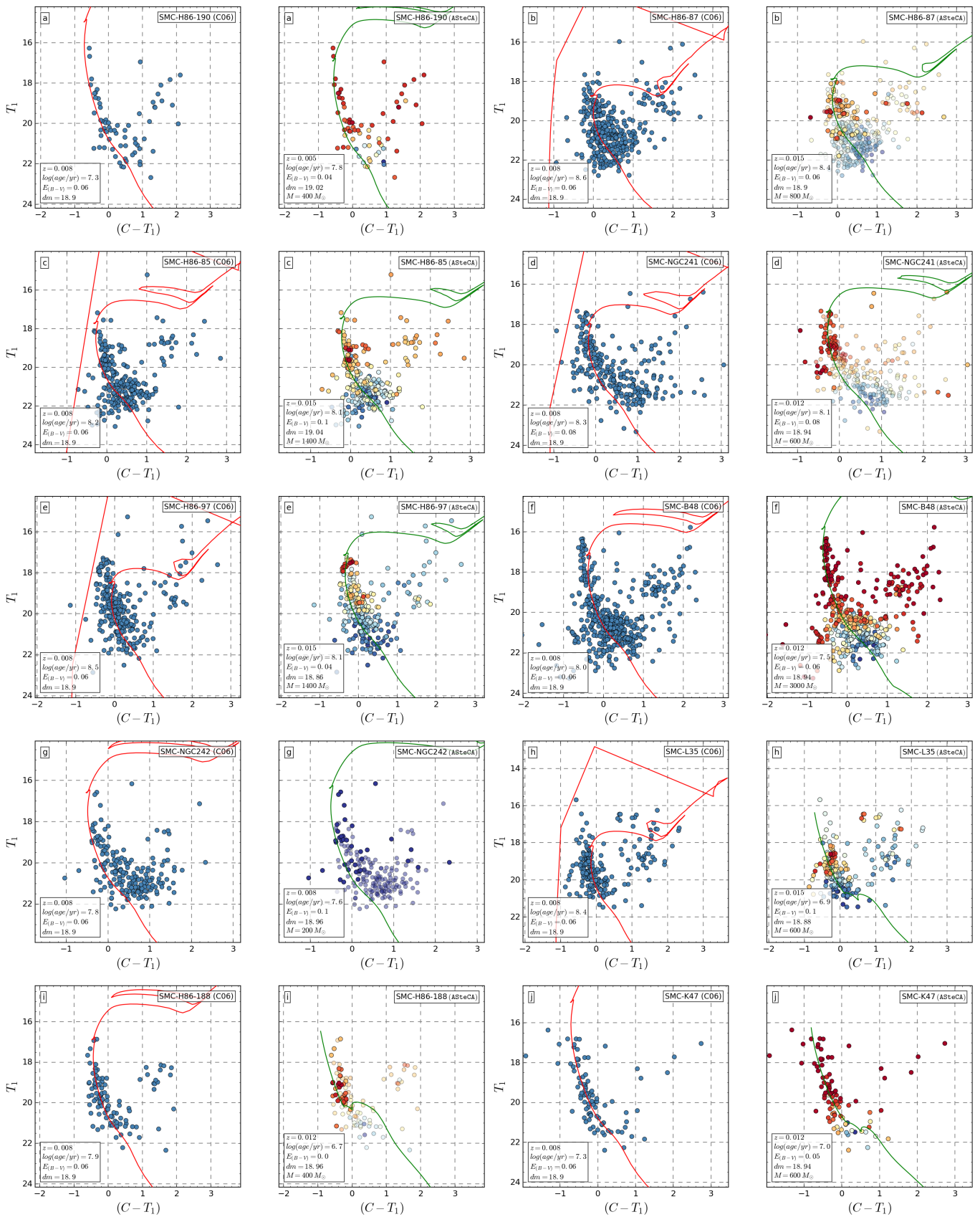
**Fig. B.3.** CMDs for the P00 database.

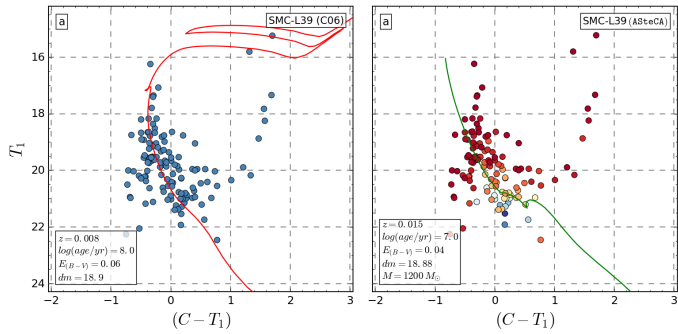
**Fig. B.4.** CMDs for the P00 database.

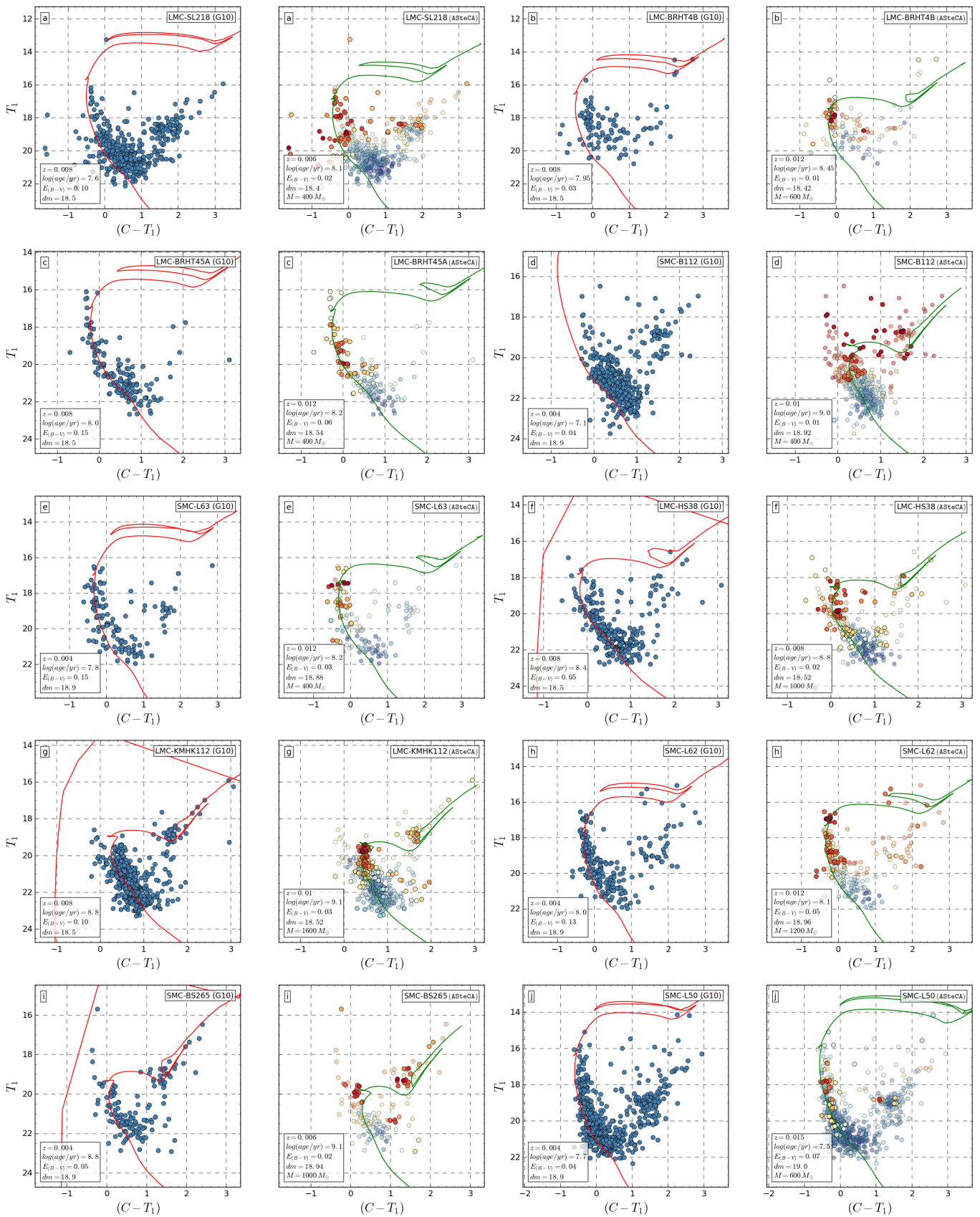
**Fig. B.5.** CMDs for the P00 database.

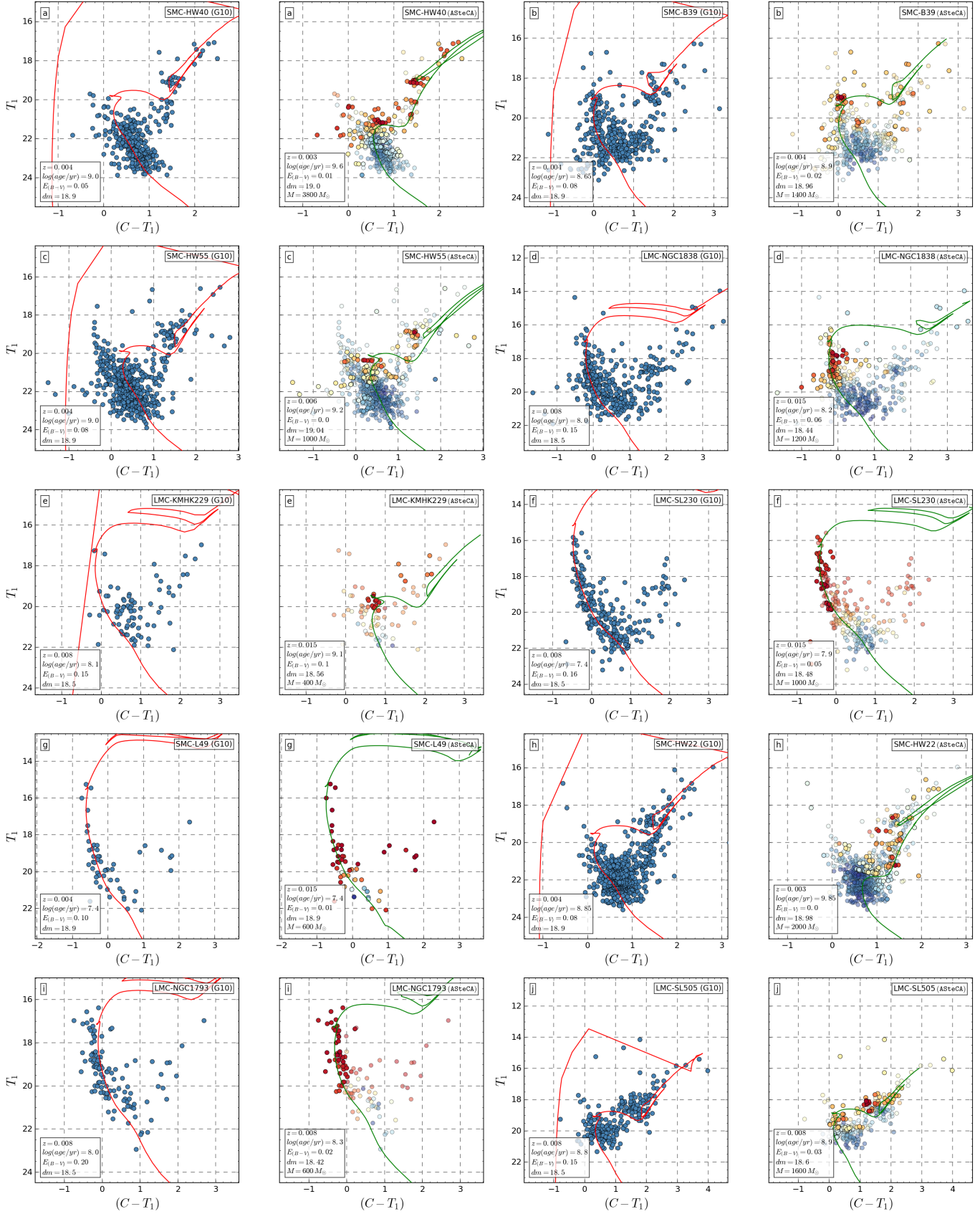
**Fig. B.6.** CMDs for the C06 database.

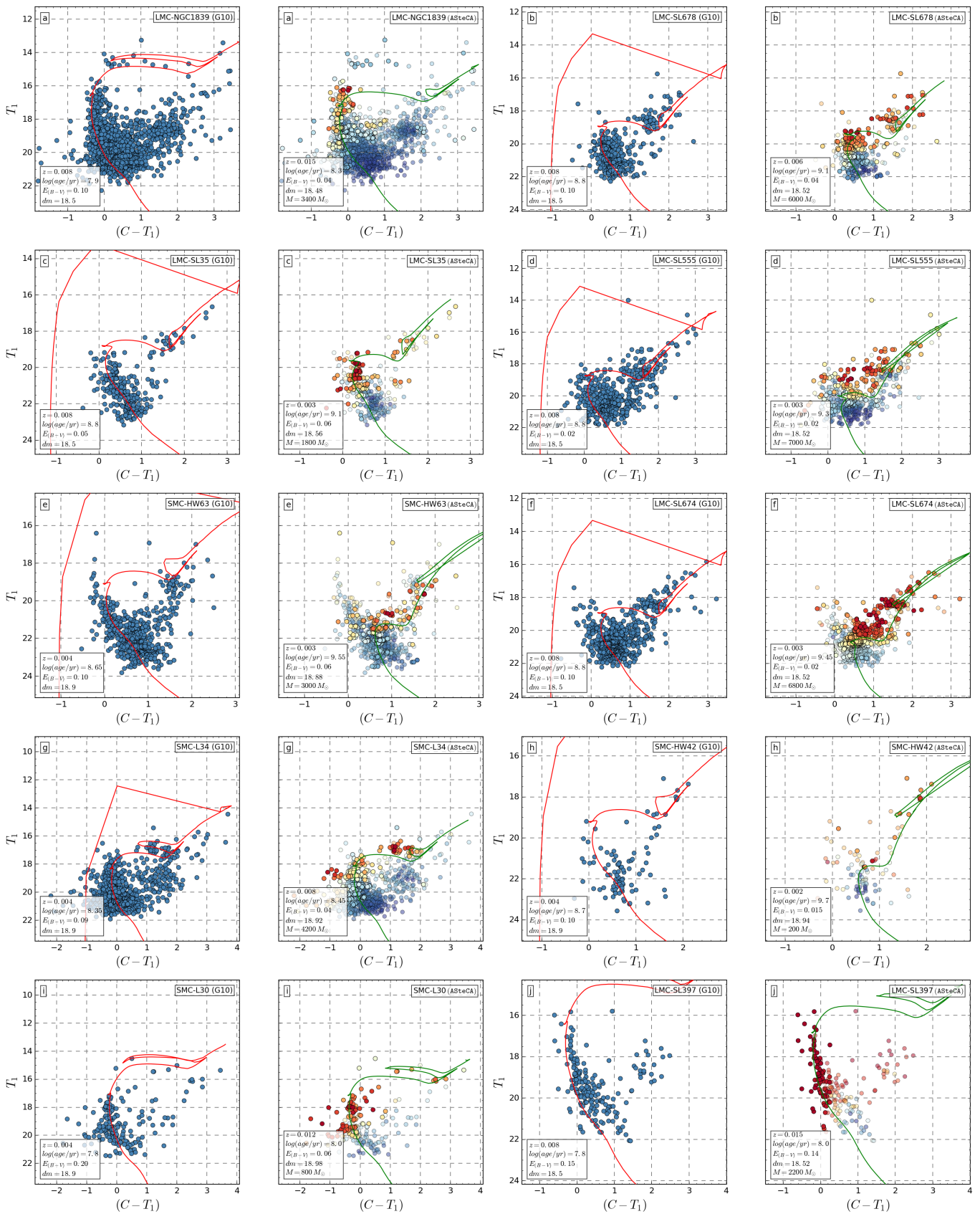
**Fig. B.7.** CMDs for the C06 database.

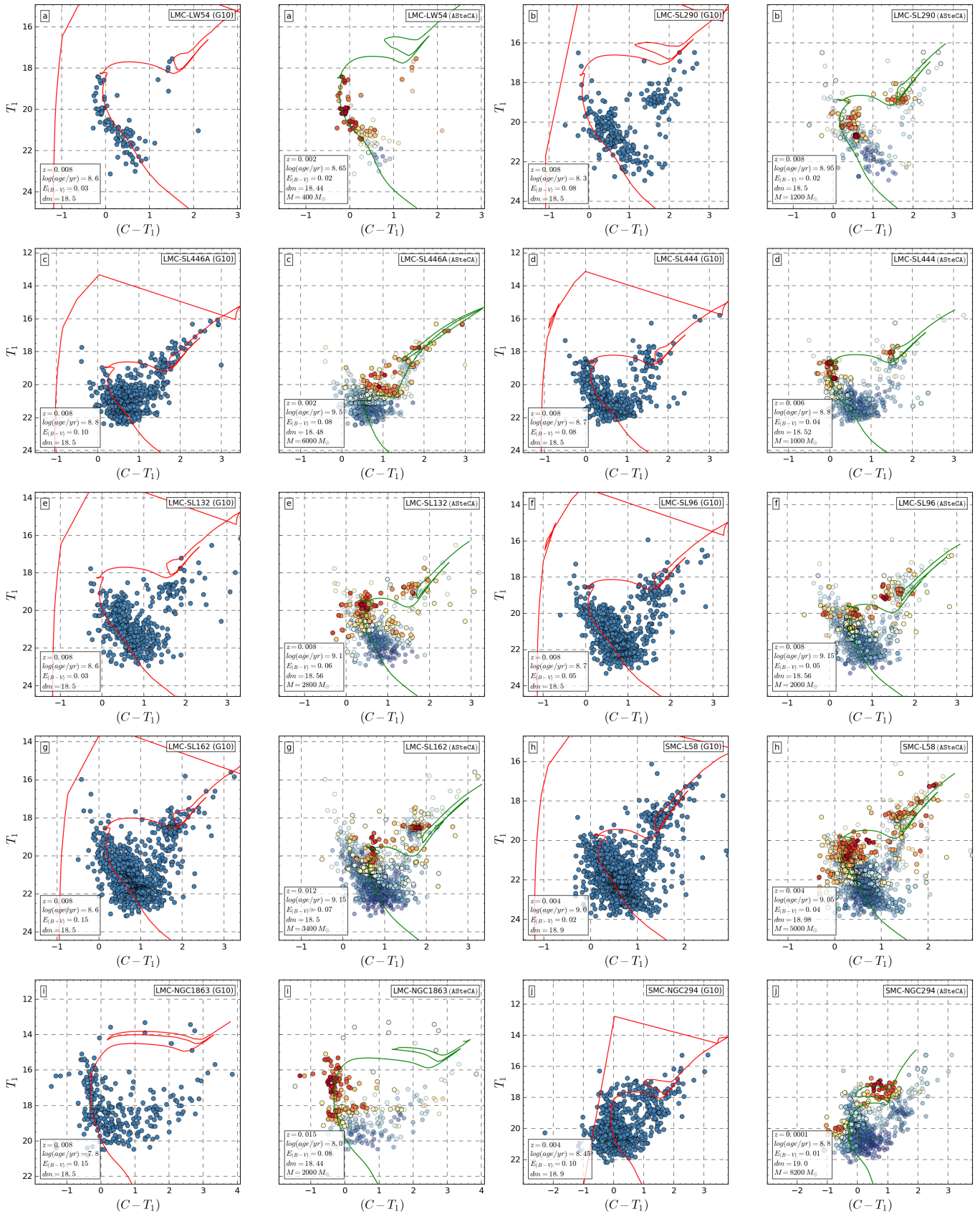
**Fig. B.8.** CMDs for the C06 database.

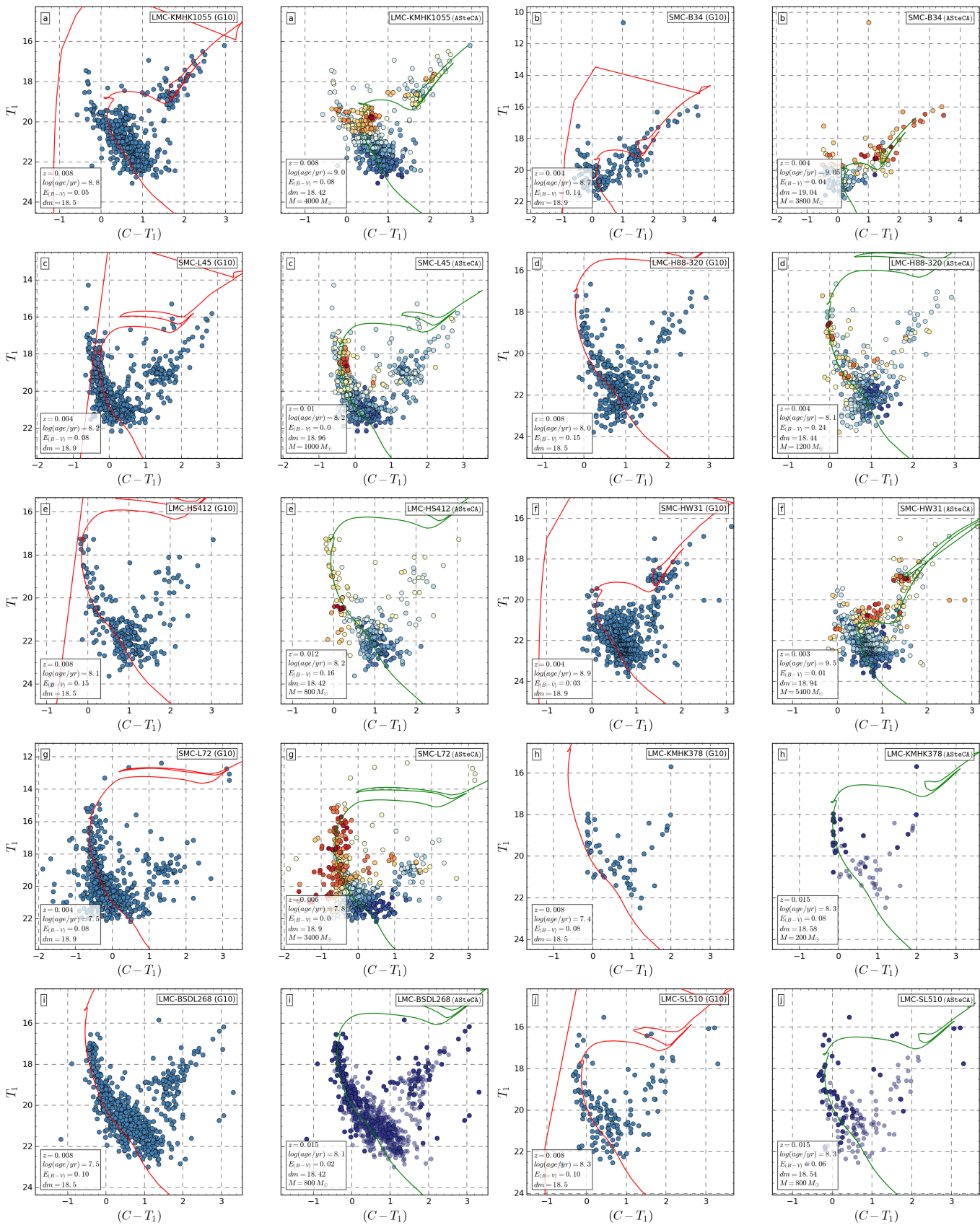
**Fig. B.9.** CMDs for the C06 database.

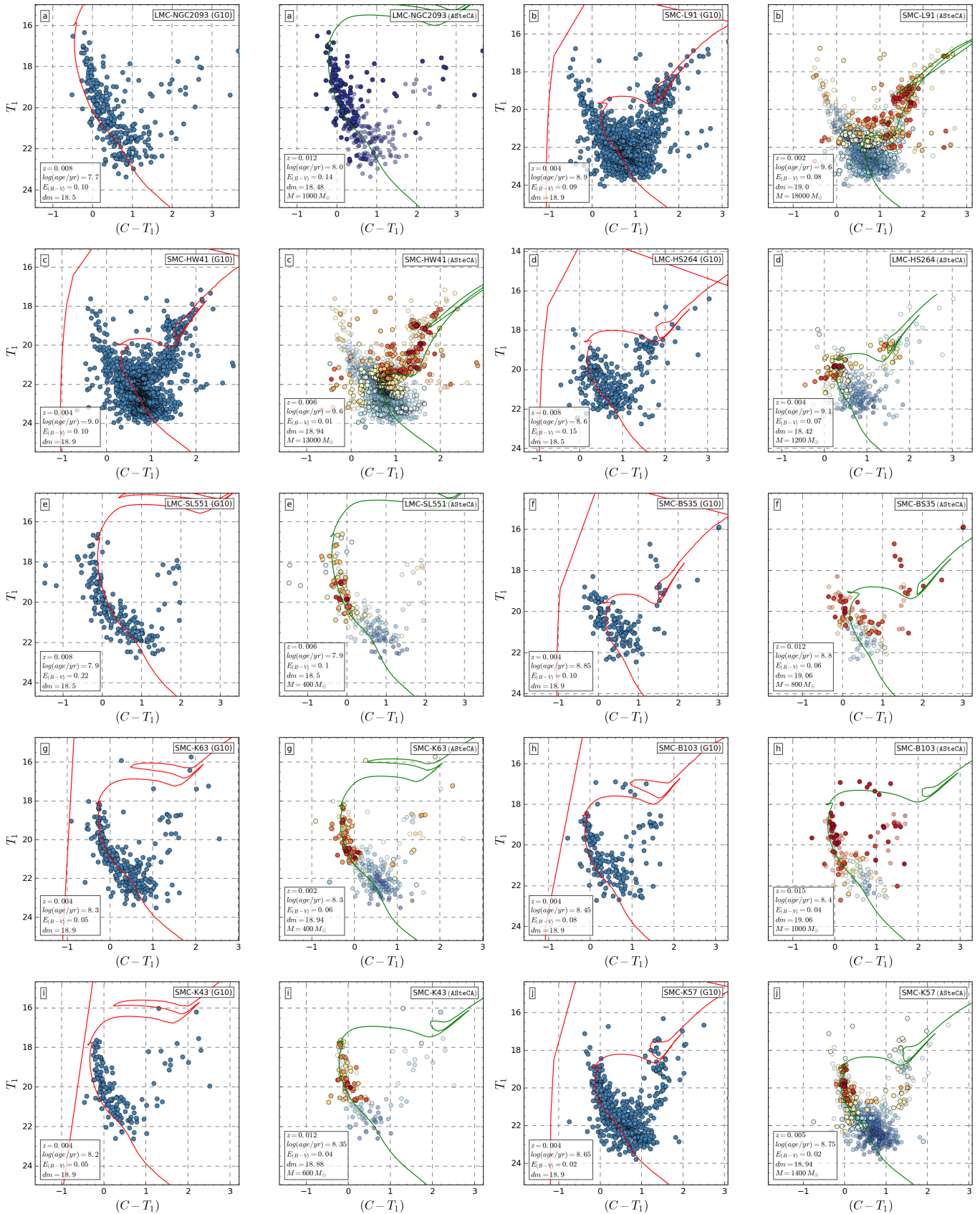
**Fig. B.10.** CMDs for the G10 database.

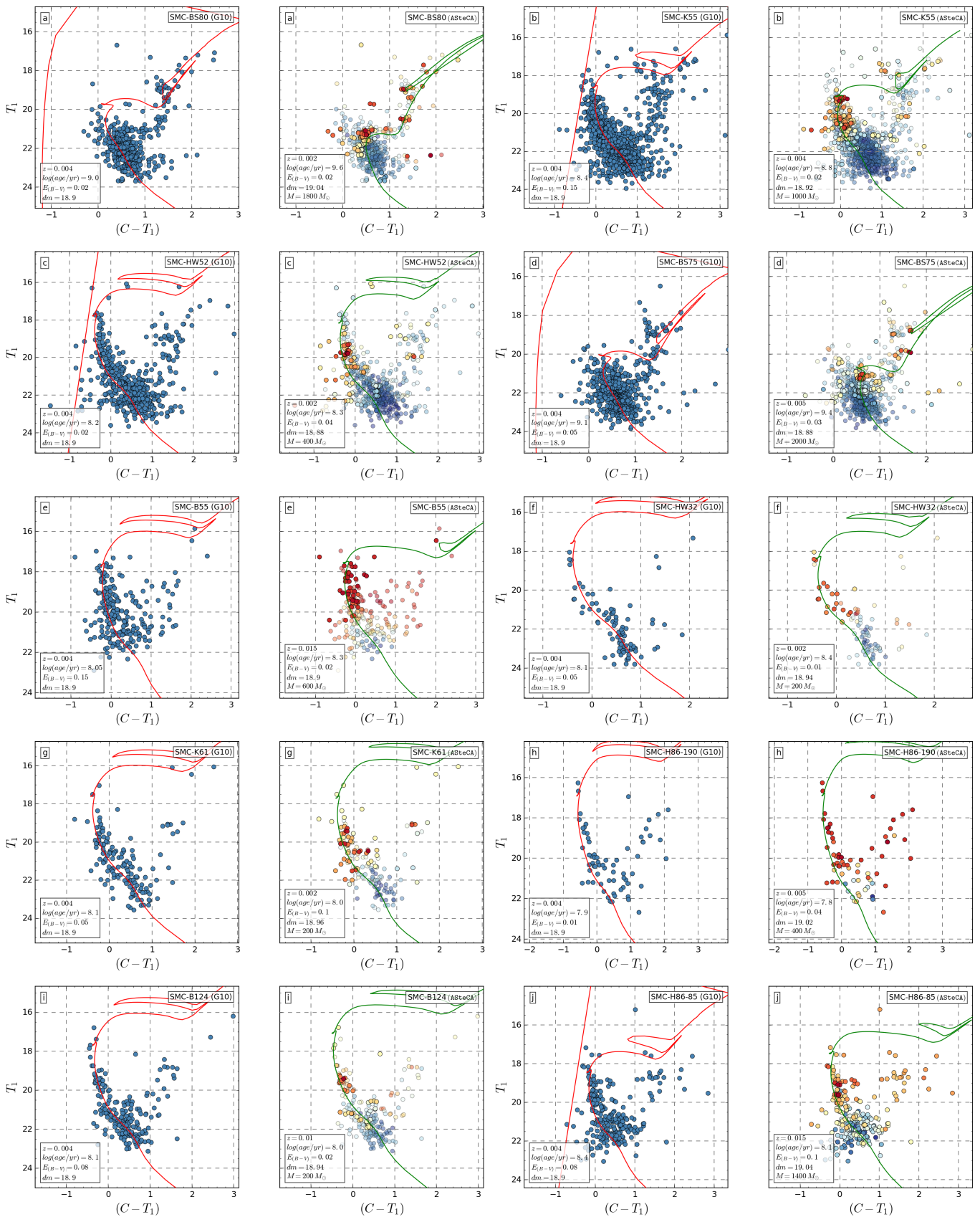
**Fig. B.11.** CMDs for the G10 database.

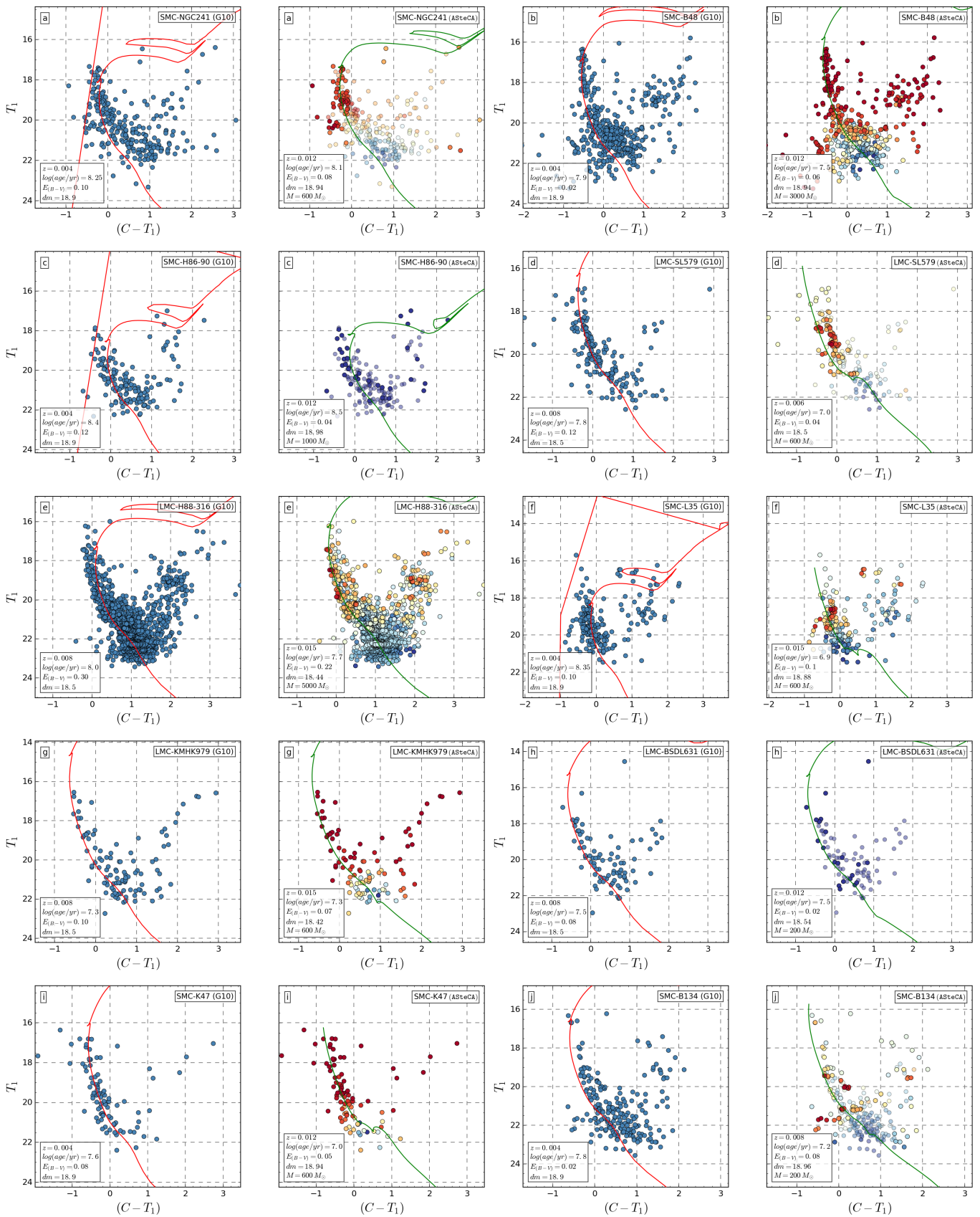
**Fig. B.12.** CMDs for the G10 database.

**Fig. B.13.** CMDs for the G10 database.

**Fig. B.14.** CMDs for the G10 database.

**Fig. B.15.** CMDs for the G10 database.

**Fig. B.16.** CMDs for the G10 database.

**Fig. B.17.** CMDs for the G10 database.

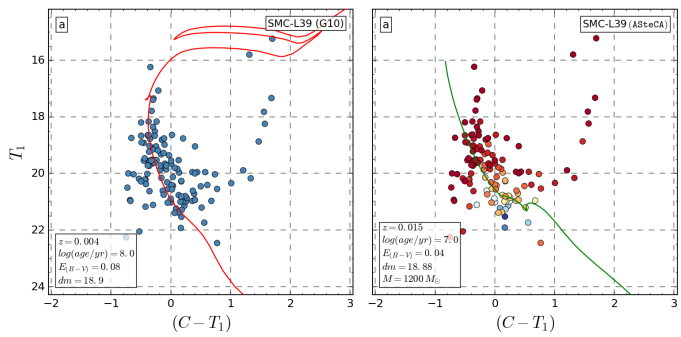


Fig. B.18. CMDs for the G10 database.

1713 Appendix C: Total cluster mass validation

1714 The likelihood used in this work, presented in Eq. 1, allows us
 1715 to set the total cluster mass as a free parameter to be optimized,
 1716 i.e. treat it the same way we treat the metallicity, age, extinction,
 1717 and distance parameters. To validate the masses recovered by
 1718 AStECA we processed 768 synthetic cluster generated with the
 1719 MASSCLEAN tool, 384 for each Magellanic Cloud. These syn-
 1720 synthetic clusters were created to imitate the metallicity, age, and
 1721 mass range that clusters in both Magellanic Clouds have, while
 1722 the distance and extinction parameters were fixed. In Table C.1
 1723 these values are shown for the five fundamental parameters fit-
 1724 ted. The process of generating a synthetic cluster with MASS-
 1725 CLEAN was described in Paper I, Sect. 3. Each MASSCLEAN
 1726 cluster had its V vs ($B-V$) CMD (in the *UBRIJHK* photometric
 1727 system) analyzed by the code.

1728 In Fig C.1 we show the results from the best match process
 1729 applied on the 768 MASSCLEAN synthetic cluster, separated
 1730 into three mass regions. The x axis displays the average mass,
 1731 i.e.: $\bar{M} = 0.5 \times (M_{\text{AStECA}} + M_{\text{MASSCLEAN}})$. The y axis shows the
 1732 relative difference mass defined in Eq.4, in the sense:

$$\overline{\Delta M_r} = (M_{\text{AStECA}} - M_{\text{MASSCLEAN}}) / (M_{\text{AStECA}} + M_{\text{MASSCLEAN}}) \quad (\text{C.1})$$

1733 Colors are associated to the differences in $\log(\text{age}/\text{yr})$ (AStECA
 1734 minus MASSCLEAN values), according to the colorbar shown
 1735 to the bottom right of the rightmost plot. The average
 1736 age difference for each mass region defined is: -0.3 ± 0.6
 1737 dex ($\bar{M} \leq 5000 [M_\odot]$), -0.04 ± 0.2 dex ($5000 < \bar{M} \leq 20000 [M_\odot]$),
 1738 -0.01 ± 0.1 dex ($\bar{M} > 20000 [M_\odot]$). As expected, cluster with
 1739 larger masses are assigned more accurate ages by the code.
 1740 On average, the difference between AStECA (estimated) minus
 1741 MASSCLEAN (true) logarithmic ages in the full mass range an-
 1742 alyzed is of $\sim -0.1 \pm 0.4$ dex. The gray bands represent the mean
 1743 and standard deviation for the average relative differences, $\overline{\Delta M_r}$,
 1744 in the estimated versus true masses. For each mass region defined
 1745 above these values are: -0.15 ± 0.2 , 0.03 ± 0.13 , 0.02 ± 0.09 , for
 1746 the combined set of synthetic clusters belonging to both galax-
 1747 ies. There is no visible trend, other than a larger average relative
 1748 difference and dispersion in the estimated mass values, for clus-
 1749 ters with low masses ($< 1000 M_\odot$). For this set of synthetic clus-
 1750 ters – where the total true mass is either $500 M_\odot$ or $1000 M_\odot$ –
 1751 the code assigns masses in a range between ~ 200 and $3000 M_\odot$.

1752 Appendix C.1: Metallicity estimation for different mass values

1753 The metallicity (z) estimated for the entire set is displayed in
 1754 Fig. C.2, for each mass value used in the generation of the
 1755 synthetic MASSCLEAN clusters. There are two clear tenden-
 1756 cies visible in these plots. First we notice that, as the cluster's
 1757 mass grows, so does the accuracy of the metallicity estimates.
 1758 Although the average difference between true and estimated z
 1759 values remains close to $\overline{\Delta z} \approx 0.001^{41}$ for the entire range, its stan-
 1760 dard deviation drops from ~ 0.01 to 0.004 for the more massive
 1761 clusters. Most of the poor solutions obtained by AStECA – those
 1762 with $|\Delta z| > 0.01$ dex – are associated to low mass scarcely popu-
 1763 lated clusters, with an average of ~ 40 true members present in
 1764 their analyzed CMDs. This poor solutions set is composed of 91
 1765 synthetic clusters (equivalent to $\sim 12\%$ of the entire processed
 1766 sample), 58 of which are of low mass ($\leq 1000 M_\odot$). The major-
 1767 ity of these low mass clusters – 38 out of the 58 – are assigned

1768 younger ages by the code, due to an improper field star decon-
 1769 tamination process (an expected issue when the number of true 1769
 1770 members is very low). If we leave out those clusters with a vis- 1770
 1771 ibly wrong age estimation – i.e., those with $|\Delta \log(\text{age}/\text{yr})| \geq 0.5$ 1771
 1772 dex – the average difference in z for the entire mass range is 1772
 1773 found to be $\sim 0.0008 \pm 0.006$ dex; a rather small difference with 1773
 1774 reasonable dispersion. These subset of clusters with wrong ages 1774
 1775 estimated by AStECA represent approximately $\sim 11\%$ of the com- 1775
 1776 bined S/LMC MASSCLEAN sample (82 synthetic clusters), and 1776
 1777 is almost entirely composed of clusters with $M \leq 1000 M_\odot$ (73 1777
 1778 synthetic clusters).

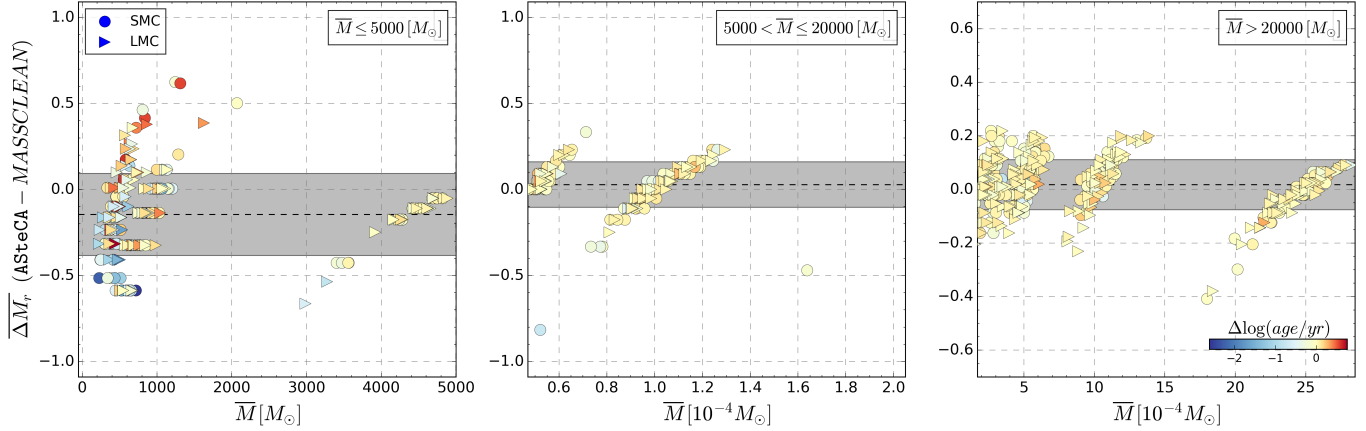
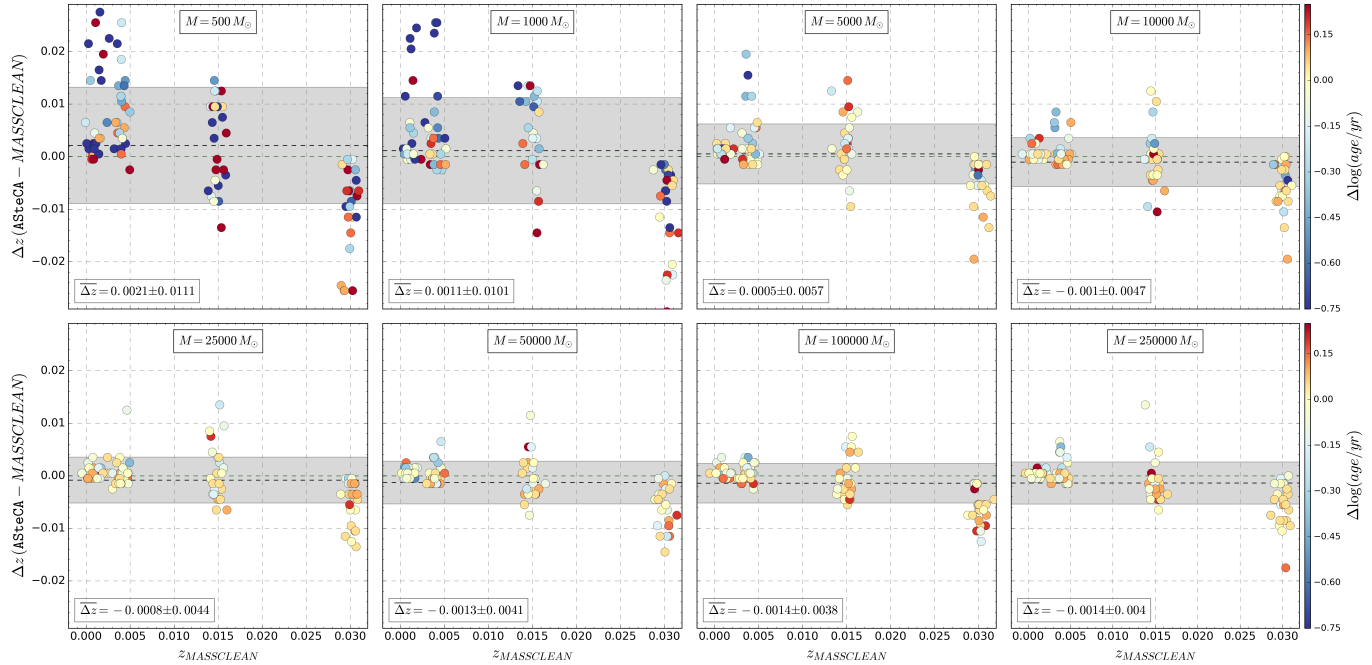
1779 Second, the code seems to overestimate the metal content 1779
 1780 for lower metallicities, and overestimate it for the largest ones. 1780
 1781 A balanced distribution around the $\Delta z=0$ line is only seen for 1781
 1782 the abundances in the middle portion of the analyzed range. 1782
 1783 This trend is much more noticeable for lower masses, but can 1783
 1784 be found for all the mass values shown. This is a statistical 1784
 1785 artifact that arises due to the necessarily limited metallicity 1785
 1786 range analyzed by the code. For the synthetic clusters with 1786
 1787 the lowest metal contents ($z=0.001$), AStECA can only assign 1787
 1788 equal or larger metallicities since negative z values are not 1788
 1789 possible. Equivalently, for the clusters with the largest abun- 1789
 1790 dances ($z=0.03$) the code can only associate equal or lower 1790
 1791 metallicities. This is because of the upper limit used in the z 1791
 1792 range analyzed by AStECA, which is precisely $z=0.03$. This 1792
 1793 “bias” could be avoided for those large metallicity clusters, by 1793
 1794 increasing the upper limit for the z range in the code. It can not 1794
 1795 be avoided for the lowest metal abundances. 1795

1796 An external source of errors also needs to be taken into ac- 1796
 1797 count when comparing AStECA's metallicity (and age) estimates, 1797
 1798 for MASSCLEAN synthetic clusters. This is the intrinsic dif- 1798
 1799 ferences between the Marigo et al. (2008) isochrones – used to 1800
 1800 generate the synthetic MASSCLEAN clusters – and the PAR- 1801
 1801 SEC (Bressan et al. 2012) isochrones – used by the code to 1802
 1802 find the optimal fundamental parameters. These differences are 1803
 1803 a source of error in the matching process that is not straight- 1804
 1804 forward to quantify. The two sets of tracks have non-negligible 1805
 1805 dissimilarities beyond the turn-off points, for most of the age 1806
 1806 range where they can be produced. This can be seen in Fig. C.3, 1807
 1807 where isochrones from both sets are compared for five differ- 1808
 1808 ent $\log(\text{age}/\text{yr})$ ages from 7.5 to 9.5 dex. For ages up to 8 1809
 1809 dex the PARSEC isochrones present a turn-off point located at 1810
 1810 lower $\log(L/L_\odot)$ values, particularly for lower metallicities. This 1811
 1811 causes a shift in the more evolved portions of the isochrone, 1812
 1812 displacing the Marigo isochrones towards larger $\log(L/L_\odot)$ val- 1813
 1813 ues. Beyond that age this effects reverses, and the PARSEC 1814
 1814 isochrones are now lifted above the Marigo tracks. Given the 1815
 1815 many known correlations between fundamental parameters (e.g., 1816
 1816 the age-metallicity, extinction-distance, and distance-metallicity 1817
 1817 relations), it is not easy to predict how the matching algorithm 1818
 1818 will resolve such instances. 1819

⁴¹ This is expected, as $z=0.001$ is the metallicity step used when pro-
 1819 cessing the synthetic clusters with AStECA.

Table C.1. Parameters values used to generate the set of 768 MASSCLEAN synthetic clusters.

Parameter	Values	N
z	0.001, 0.004, 0.015, 0.03	4
log (age/yr)	7, 7.2, 7.5, 7.7, 8, 8.2, 8.5, 8.7, 9, 9.2, 9.5, 9.7	12
μ	18.9 (SMC), 18.5 (LMC)	2
E_{B-V}	0.1	1
Mass (M_\odot)	500, 1000, 5000, 10000, 25000, 50000, 100000, 250000	8

**Fig. C.1.** Recovered masses by ASteCA, for the set of 384 SMC MASSCLEAN synthetic clusters. Relative masses are obtained in the sense ASteCA minus MASSCLEAN (i.e.: estimated minus true values), and shown in the y axis. The average masses in the x axis are perturbed with a small random scatter to improve visibility.**Fig. C.2.** ASteCA metallicity estimates for each mass used to generate the synthetic MASSCLEAN clusters. Colors are associated to the logarithmic age differences, shown in the colorbars to the right. The green dashed horizontal line is the $\Delta[\text{Fe}/\text{H}] = 0$ line, show as reference.

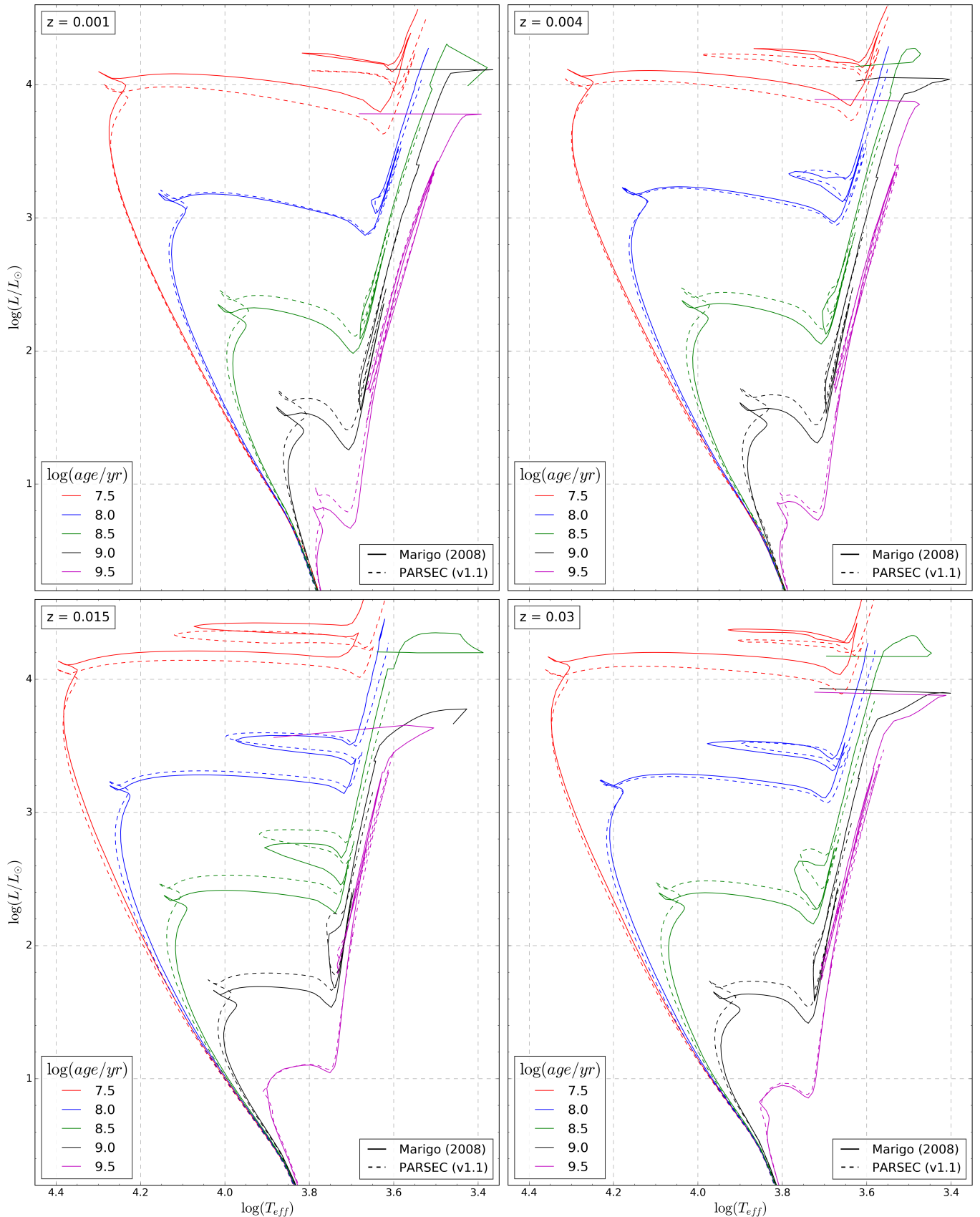


Fig. C.3. Marigo et al. (2008) versus PARSEC (Bressan et al. 2012) isochrones, for different metallicities and ages.

1820 **Appendix D: Color-magnitude diagrams for large
1821 mass OCs**1826 more information about the fundamental parameters assigned to these OCs.
18271822 We present in Fig D.1 CMDs for the five OCs with the largest
1823 mass estimates by either the H03 or the P12 databases. These
1824 are also the OCs with the largest differences in assigned masses
1825 when compared with those derived by AStECA. See Table 5 for

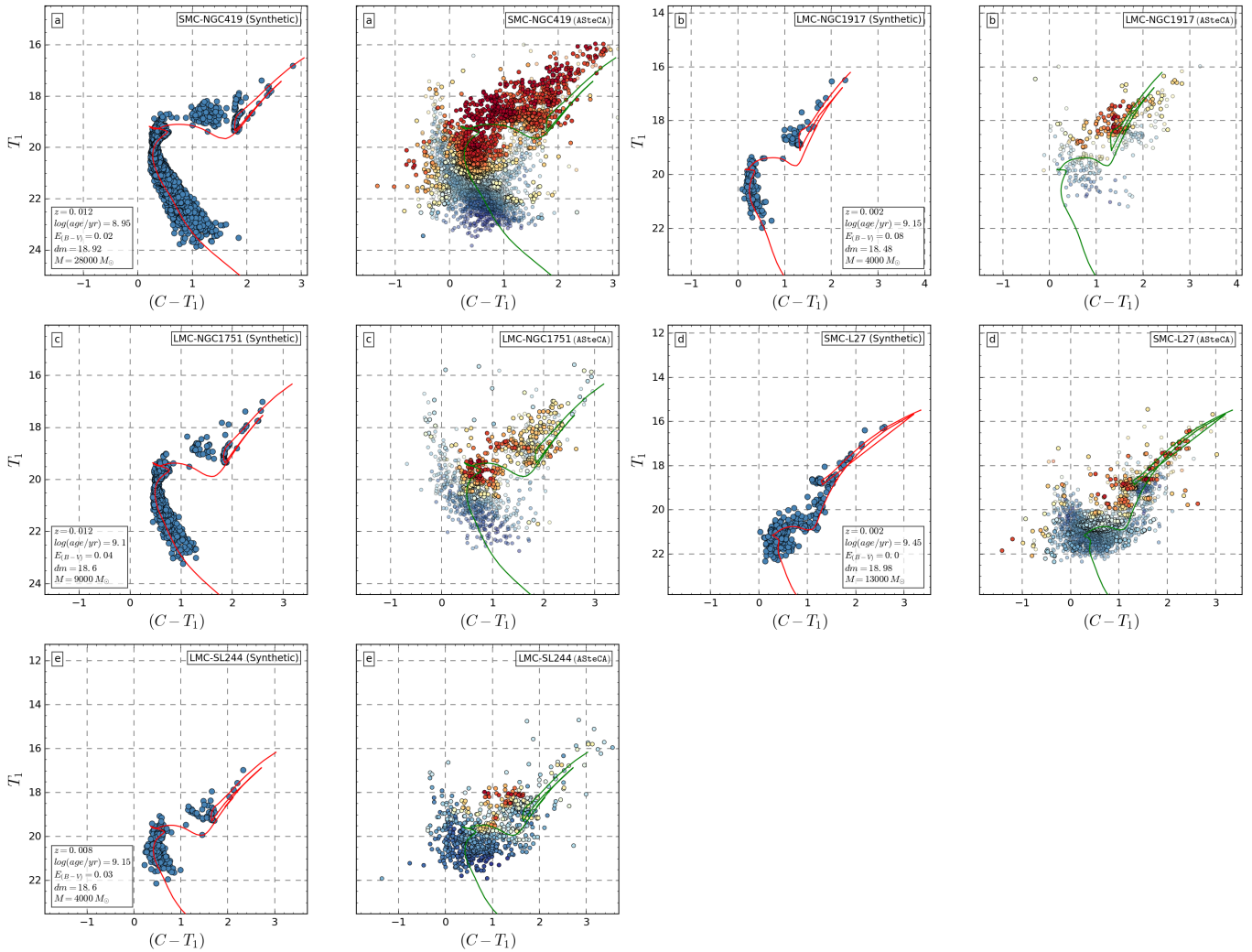


Fig. D.1. CMDs for the OCs with the largest masses assigned by H03 and/or P12. The best match synthetic cluster is plotted to the right, and the observed cluster region CMD to the left, for each OC.

1828 **Appendix E: Age-metallicity relationships for**
 1829 **literature values**

1830 Fig. E.1 shows the AMRs for both Clouds, generated using the
 1831 metallicity and age values taken from those articles presented in
 1832 Table. 1, i.e.: the “literature”.

1833 In Fig. E.2 the CMDs for the four LMC OCs with metallicity
 1834 and ages in the vicinity of ~ 3.3 Gyr and $[Fe/H] \approx -0.25$ dex,
 1835 are shown. These are the OCs responsible for the high metallicity
 1836 found for the AMR of this galaxy, for ages close to 4 Gyr.

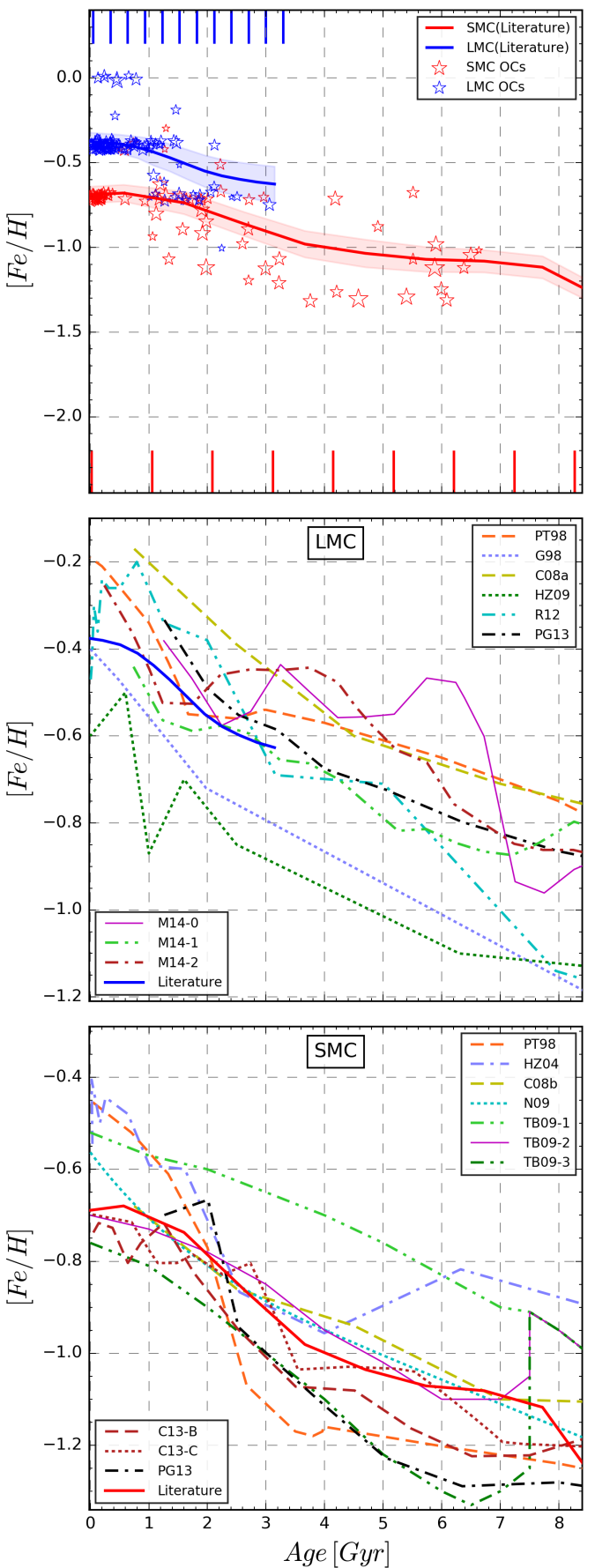


Fig. E.1. Age-metallicity relationships for our set of 239 OCs, using log (age/yr) and $[Fe/H]$ values taken from the literature.

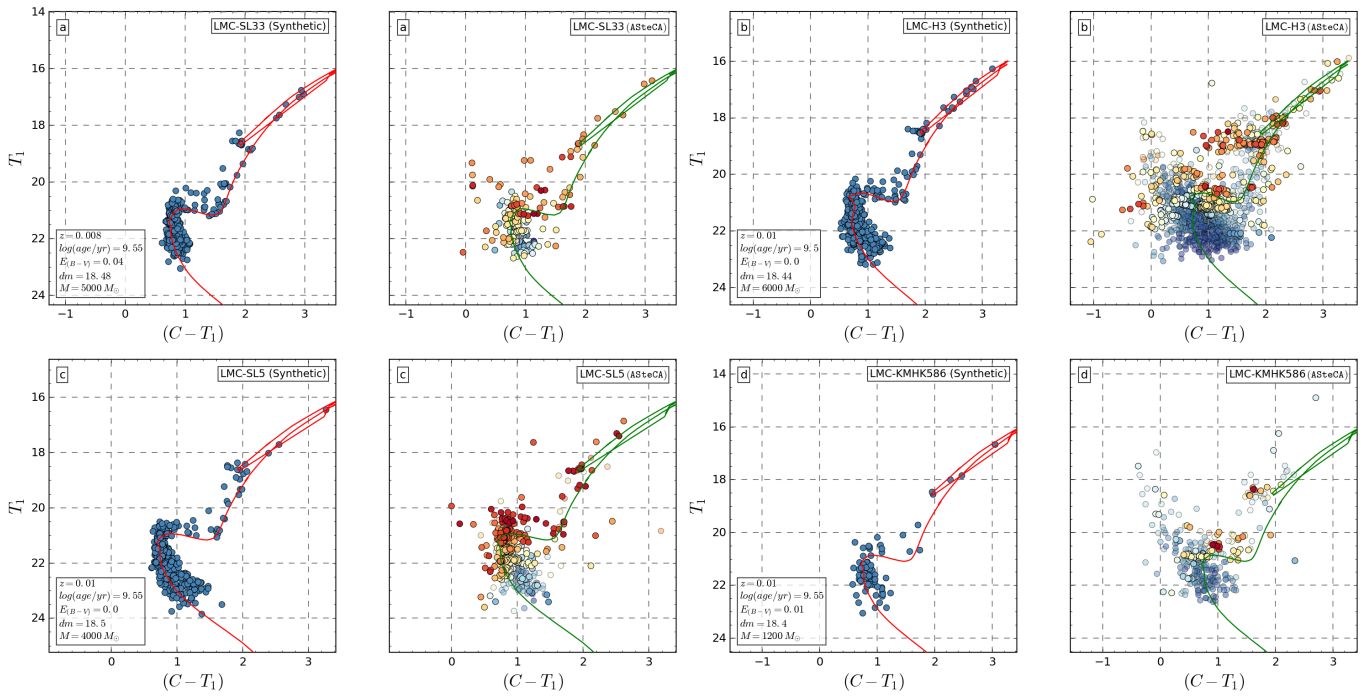


Fig. E.2. CMDs for the OCs that cause a peak in the AMR for the LMC, for ages close to 4 Gyr. The best match synthetic cluster is plotted to the right, and the observed cluster region CMD to the left, for each OC.